Effective Black Holes in Quantum Gravity

Samantha Hergott

A Dissertation submitted to the Faculty of Graduate Studies in Partial Fulfillment of the Requirements for the Degree of Doctor of Philosophy

Graduate Program in Physics

York University
Toronto, Ontario

June, 2025

Abstract

This dissertation explores quantum gravity applications to resolve black hole singularities, investigates the potential transition from black holes to white holes, and characterize the resulting spacetime in each scenario. The following work utilizes various approaches, including canonical loop quantum gravity (LQG) and the generalized uncertainty principle (GUP), while also adopting a more flexible framework that is not tied to any single quantum gravity theory. Instead, this research relies on guiding principles expected to emerge from a complete theory of quantum gravity. Through this exploration, the dissertation aims to contribute to the resolution of key issues in black hole physics within a quantum gravity setting.

The first significant contribution of this thesis involves the application of the Raychaudhuri equation to assess the existence of singularities. In particular, loop quantum gravity corrections to the Raychaudhuri equation are derived for the interior of a Schwarzschild black hole and near the classical singularity. The analysis demonstrates that the resulting effective equation leads to the defocusing of geodesics, caused by the emergence of repulsive terms. This effect prevents the formation of conjugate points, renders the singularity theorems inapplicable, and ultimately facilitates the resolution of the singularity in this spacetime.

Building on this, the next part of the work extends similar ideas within the framework of the generalized uncertainty principle. To address challenges identified in a previous model of the interior of a generalized uncertainty-inspired black hole, an "improved scheme" is introduced, drawing inspiration from loop quantum gravity. In this scheme, quantum parameters become momentum-dependent, allowing the interior to be reworked and extended to the full spacetime. The resulting metric is found to be asymptotically flat, and its associated Kretschmann scalar remains regular throughout. Furthermore, it is shown that both the null expansion and Raychaudhuri equation are regular across the entire spacetime, indicating the resolution of the classical singularity.

The final chapters do not focus on a specific theory of quantum gravity but instead construct a class of time-dependent, asymptotically flat, spherically symmetric metrics to model gravitational collapse in quantum gravity. By imposing a quantum bounce, these metrics prevent singularity formation. They exhibit general properties expected from any quantum gravity theory, without committing to a particular approach. These metrics capture key insights into the dynamics of singularity resolution, as well as horizon formation and evaporation, following either a matter bounce or a black hole to white hole transition.

Acknowledgments

Studying science has always been a passion of mine. Growing up on a farm, I was surrounded by nature, exploration and—of course—the night sky scattered with stars. My parents would make us up a cozy bed in the back of the pick up truck, pack snacks and park on the biggest hill on our property to watch meteor the showers all night long. We would see fire balls, make a thousand wishes on all the shooting stars and eat jellybeans. My parents taught me everything they knew about nature, building things, raising animals, and, most importantly, staying curious. For any phase of science I went through they bought me every book, every toy and took me to any science museum we could find. From aspiring meteorologist and storm chaser, to environmental scientist, to astronomer and finally a theoretical physicist, their endless encouragement has never wavered. A special thanks to my little brother, who patiently played "school" with me so I could teach him everything I was learning. In hindsight, this may have backfired—he's now better at math than me and never lets me forget it. I am so grateful to have such an incredible family who have always embraced my endless stream of hobbies and interests.

An important part of my journey has of course been all of the friends I've made throughout the years. Emilie—you are the glue that holds my sanity together. Thank you for your constant love, endless supply of pep-talks, and understanding that not calling you for a month is nothing to be taken personally. Fred and Jorden—thank you for being my kind of weird. I cherish all our worldly adventures and hope we can continue the traditions for many years to come. To my Perimeter friends, Alice and Brayden — it has been such an honor to go through both our Master's and PhD journeys together. Your consistent willingness to serve as my social decoys in awkward situations has not gone unnoticed — thank you both.

To my supervisors, Matt and Saeed—I cannot begin to express how grateful I am to you both. Matt, thank you for allowing me the freedom to continue working with Saeed. Your support throughout this has meant everything to me. I truly appreciate your honesty and thoughtful advice whenever we discuss my possible future plans. Saeed, I am incredibly grateful for the time you've spent sharing your ideas and knowledge. Whether you know it or not, you helped me rediscover my passion for learning. This journey can often feel long and fruitless, but having a supervisor who is is genuinely curious, passionate, and generous with their time makes all the difference. Thank you for choosing me as your first ever PhD student.

Lastly, thank you to my husband, Jeffrey, for walking every step of this journey with me. Thank you for putting up with my late-night study sessions, making dinner when I'm glued to the computer, forcing me to take breaks when I'm overwhelmed, and always encouraging me to chase my dreams, even if it means living in different countries. You inspire me everyday.

Statement Of Contributions

The material presented in this dissertation was largely written by myself and is based on coauthored publications to which I made significant contributions.

Chapter 2 comes from the published work [36] written in collaboration with Saeed Rastgoo, Saurya Das and Keagan Blanchette. Chapter 3 comes from the published work [89], written in collaboration with Saeed Rastgoo, Federica Fragomeno, Douglas M. Gingrich, and Evan Vienneau. Chapters 4 and 5 are based on the published work [123] and at the time of writing, a not yet published paper, both written in collaboration with Saeed Rastgoo and Viqar Husain. Permission was given to include all the above works.

Contents

List of Figures

1 Introduction

It may seem like almost every introductory paragraph of any quantum gravity text book or research paper begins with some version of the phrase, “General relativity works — until it doesn’t”. This dissertation is no exception. The predictions of black hole and big bang singularities reveal the limits of the classical theory, highlighting the need for a deeper framework that can describe the physics of spacetime beyond these breakdown points. Over the decades, quantum gravity research has made significant strides in proposing mechanisms through which singularities might be avoided, both in cosmological settings and inside black holes [1–4]. This dissertation builds on those efforts, contributing to the growing body of work aimed at constructing a consistent quantum gravity framework and exploring its phenomenological implications, particularly in black hole interiors and singularity resolution.

The projects presented in chapters (2-5) explore the classical limits, phenomenological consequences, and the engineering of effective spacetime metrics. The works are motivated by the loop quantum gravity (LQG) approach to quantum gravity, but chapter 3 borrows techniques from LQG and applies them to another framework, the generalized uncertainty principle (GUP). Chapters 4 and 5 are model-independent, in the sense that they incorporate general features expected in quantum gravity without committing to a specific framework. The central idea is that, regardless of which specific theory of quantum gravity ultimately proves correct, they share a common objective of ensuring that the fabric of spacetime remains coherent, even at its most extreme.

Throughout this dissertation, unless stated otherwise, natural units will be employed, $c, \hbar = 1$. Newton’s constant will be left as G and four spacetime dimensions are considered with a metric signature of mostly plus, $(-+++)$. Except for section 1.3, lowercase Greek letters $\mu, \nu = 0, 1, 2, 3$ denote spacetime indices, while lowercase Latin letters $i, j = 1, 2, 3$ from the middle alphabet denote spatial indices. Section 1.3 adopts popular LQG notation and uses $a, b = 0, 1, 2, 3$ for coordinate spacetime indices as well as coordinate spatial indices, $I, J = 0, 1, 2, 3$ and $i, j = 1, 2, 3$ are internal SU(2) indices for LQG’s tetrad and triad formulation respectively.

1.1 General Relativity- The Bare Minimum

General relativity (GR) describes gravity as the curvature of spacetime governed by Einstein’s field equations,

$$R_{\mu\nu} - \frac{1}{2} R g_{\mu\nu} = 8\pi G T_{\mu\nu}. \tag{1.1.1}$$

The left-hand side is the Einstein tensor, $G_{\mu\nu}$, encoding the curvature of spacetime. The right hand side captures the matter and energy content, given by the stress energy tensor $T_{\mu\nu}$. These equations encode how matter and energy determine the geometry of spacetime, which in turn dictates the motion of particles and fields. The Ricci tensor $R_{\mu\nu}$ and the Ricci scalar $R \equiv g^{\mu\nu}R_{\mu\nu}$ are both contractions of the full Riemann curvature tensor $R^{\rho}{}_{\sigma\mu\nu}$. The metric tensor $g_{\mu\nu}$ defines both the geometric and causal structure of spacetime. Solving Einstein's equations thus amounts to determining the components of the metric consistent with the given matter content.

An equivalent rearrangement of the equations

$$R_{\mu\nu} = 8\pi G(T_{\mu\nu} - \frac{1}{2}Tg_{\mu\nu}), \tag{1.1.2}$$

expresses more directly how the Ricci tensor is sourced by matter, where $T = g^{\mu\nu}T_{\mu\nu}$ is the trace of the stress-energy tensor.

Einstein's equations can be derived from a Lagrangian formulation. The Einstein-Hilbert action is given simply by

$$S_{EH} = \int \sqrt{-g}\ R\ d^4x, \tag{1.1.3}$$

where $g = \det(g_{\mu\nu})$. The dynamical variable is the metric $g_{\mu\nu}$, and varying the action with respect to this will result in the vacuum Einstein's equation

$$\frac{1}{\sqrt{-g}}\frac{\delta S_{EH}}{\delta g^{\mu\nu}} = R_{\mu\nu} - \frac{1}{2}Rg_{\mu\nu} = 0. \tag{1.1.4}$$

To include matter, the action must include also the action for the specific matter under consideration, S_m, so the total action is $S = S_{EH} + S_m$. The stress-energy tensor is then determined by variation of S_m with respect to the metric and is given by the following,

$$T_{\mu\nu} = -\frac{2}{\sqrt{-g}}\frac{\delta S_m}{\delta g^{\mu\nu}}. \tag{1.1.5}$$

This leads to the full Einstein equations (1.1.1), forming the foundation for general relativity. This action-based formulation also serves as the starting point for the canonical formulation used in loop quantum gravity, developed in Section 1.3.

1.2 Black Holes and Spherically Symmetric Spacetimes

Black holes represent fundamental solutions in classical general relativity, offering insights into the nature of gravitational collapse. Despite advances in experimental observations confirming their existence, the nature of singularities predicted by classical GR — where curvature diverges and known physics breaks down — remains an open challenge. This has motivated extensive research in quantum gravity, where black holes are expected to provide crucial insights into the interplay between quantum mechanics and general relativity.

A spacetime is said to be spherically symmetric if there exist coordinates such that the metric can be written in the following form [5]

$$\mathrm{d}s^2 = \gamma(x)_{AB}\mathrm{d}x^A\mathrm{d}x^B + r(x)^2\mathrm{d}\Omega^2. \tag{1.2.1}$$

Where $A, B = 0, 1$ and $d\Omega^2 = d\theta^2 + \sin^2\theta d\phi^2$ is the metric on a unit two-sphere.

Symmetries of a metric are characterized by the existence of Killing vector fields which are infinitesimal generators of isometries [6]. A spacetime is said to be spherically symmetric if it admits three spacelike Killing vectors $\boldsymbol{\xi}_i$ (for $i = 1, 2, 3$) satisfying the relations $[\boldsymbol{\xi}_i, \boldsymbol{\xi}_j] = \boldsymbol{\epsilon}_{ijk}\boldsymbol{\xi}_k$, where ϵ_{ijk} is a $3D$ Levi-Civita symbol and $[\xi_i, \xi_j]^\nu = \xi_i^\mu\partial_\mu\xi_j^\nu - \xi_j^\mu\partial_\mu\xi_i^\nu$ is the Lie bracket, generating the $SO(3)$ symmetry group [5,6]. A spacetime is said to be stationary if it possesses a Killing vector that is timelike near infinity. In a stationary spacetime coordinates can be chosen such that the metric components are completely independent of t. A spacetime is static if it is stationary and invariant under time reversal, implying no cross terms involving dt in the metric [6].

1.2.1 The Schwarzschild Metric

An important example of a spherically symmetric spacetime is the vacuum solution that describes the empty region surrounding a spherically symmetric, non-rotating gravitational source. In vacuum (where the stress-energy tensor vanishes), Einstein equations from Eq. (1.1.2) become

$$R_{\mu\nu} = 0. \tag{1.2.2}$$

The solution is the Schwarzschild metric, written in spherical coordinates it is given by the following

$$\mathrm{d}s^2 = -\Big(1 - \frac{2GM}{r}\Big)\mathrm{d}t^2 + \Big(1 - \frac{2GM}{r}\Big)^{-1}\mathrm{d}r^2 + r^2\mathrm{d}\Omega^2. \tag{1.2.3}$$

The constant M can be interpreted as the mass of the gravitating object [6]. Birkhoff's theorem states that this is the unique spherically symmetric solution to the vacuum Einstein equations [7]. Importantly, no assumptions are made about the dynamics of the matter source—only spherical symmetry. This means the Schwarzschild metric applies to the vacuum outside a collapsing star, a static star, or any spherically symmetric mass distribution. [5,6].

It is obvious from Eq. (1.2.3) that at $r = 0$ and $r = 2GM$, the first two metric components either diverge or vanish. It is essential to determine whether these are genuine physical singularities or merely coordinate artifacts. A more detailed exploration of singularities is still to come but for the moment, some attention can be given to the "Schwarzschild radius" $r_s \equiv 2GM$.

Investigations of geodesic behaviour in Schwarzschild spacetime reveal that $r = 3r_s$ is the smallest possible radius of a stable circular orbit for a massive particle, while unstable circular orbits exist for $\frac{3r_s}{2} < r < 3r_s$ [6,8]. For a massless particle, i.e a photon, an unstable circular orbit exists at $r = \frac{3r_s}{2}$ which means an un-disturbed photon will orbit in a circle forever [6]. This is often referred to as the photon sphere. For most ordinary objects like the Sun or Earth, the Schwarzschild radius lies well within the interior where the vacuum Schwarzschild solution is no longer applicable [8]. However, objects with a radius smaller than its Schwarzschild radius and an exterior spacetime described by the Schwarzschild metric are called spherically symmetric, static black holes [5,6].

1.2.2 Black Holes

The nature of r_s can be further examined by considering a freely falling observer moving radially inward toward a black hole. Such an observer will reach $r = r_s$ in a finite proper time, while for a distant observer, the infalling observer appears to take an infinite amount of coordinate time to cross this boundary (see [9] for details). Furthermore, nothing "odd" happens for the infalling observer, the spacetime geometry is well behaved, and the observer crosses through unscathed. This implies that r_s is likely a coordinate singularity rather than a physical one.

An interesting consequence of these coordinates is that t and r switch their causal nature upon crossing the Schwarzschild radius. A timelike interval is expressed as $ds^2 < 0$ (versus a spacelike interval $ds^2 > 0$ or null $ds^2 = 0$). When $r < 2GM$, notice that $(1 - \frac{2GM}{r}) < 0$ and so

$$-\left(1 - \frac{2GM}{r}\right)dt^2 > 0 \qquad\qquad \left(1 - \frac{2GM}{r}\right)dr^2 < 0.$$

In the region $r > r_s$, t is a timelike coordinate, while r is a spacelike coordinate, but upon crossing the Schwarzschild radius $r < r_s$, t becomes a spatial coordinate while r becomes a temporal coordinate. This means that so long as the observer is outside of r_s, he can change his direction and go from decreasing r to an increasing r. However, if the observer has crossed r_s, there is no way he can reverse the direction of r, just as there is no way he could reverse the direction of time outside r_s. The observer has no choice but to follow the timelike coordinate r to the later value $r = 0$ [9]. This timelike and spacelike role reversal property will be favourable later on.

Recognizing that the Schwarzschild radius corresponds to a coordinate singularity rather than a physical one motivates the introduction of an alternative coordinate system. The Painlevé-Gullstrand (PG) coordinates introduce a transformation of the Schwarzschild time t to a new t_{PG} designed to remain finite at the Schwarzschild radius r_s. This new time coordinate corresponds to the proper time experienced by a freely falling observer who starts at rest at infinity and moves radially inward toward the black hole. Consequently, the coordinate t_{PG} avoids the coordinate singularity that arises in the Schwarzschild coordinate system at r_s. The Schwarzschild metric, expressed in PG coordinates (with t_{PG} relabeled as t for simplicity), is given by [5],

$$\mathrm{d}s^2 = -\Big(1 - \frac{2GM}{r}\Big)\mathrm{d}t^2 + 2\sqrt{\frac{2GM}{r}}\mathrm{d}t\mathrm{d}r + \mathrm{d}r^2 + r^2\mathrm{d}\Omega^2. \tag{1.2.4}$$

This coordinate system proves to be beneficial as it remains regular at $r = r_s$ and allows the metric to describe the motion of infalling observers smoothly as they cross the Schwarzschild radius.

One of the most important features of a black hole is the event horizon which is defined plainly to be a boundary that separates null geodesics that escape to infinity from those that do not [6, 10]. More precisely, an event horizon is a null hypersurface that globally bounds the region of spacetime from which signals cannot reach future null infinity. Determining the position of the event horizon in spherically symmetric spacetimes involves identifying the $r = const$ hypersurface whose normal vector $\partial_\mu r$ is null, satisfying the condition,

$$g^{\mu\nu}\partial_\mu r \partial_\nu r = 0. \tag{1.2.5}$$

In stationary spherically symmetric or axisymmetric spacetimes, such as Schwarzschild or Kerr, this reduces to the condition $g^{rr} = 0$. This quantity is sometimes referred to as the "horizon function" and denoted by Θ. However, in non-stationary spacetimes, the vanishing of $\Theta = g^{rr}$ does not necessarily signal the presence of an event horizon, and instead indicates the presence of an apparent horizon (discussed below).

While the event horizon is a fundamental concept, it is often an impractical tool for studying the geometry and causal structure of spacetime due to its global nature. Determining the event horizon requires knowledge of the entire spacetime evolution; information about the geometry at a specific location alone is insufficient [5,6]. To address this limitation, local notions of horizons such as trapped surfaces and apparent horizons are often employed.

A trapped surface is a two-dimensional, compact, spacelike surface on which both outgoing and ingoing null geodesics are converging rather than diverging. The apparent horizon is defined as a local boundary of a region containing trapped surfaces. It is a marginally trapped surface, where outgoing null geodesics are momentarily stationary, marking the limit beyond which light or any other signals cannot escape. Unlike the event horizon, which depends on the full causal structure of the spacetime, the apparent horizon is determined locally and can evolve dynamically as the spacetime changes [11]. In spherically symmetric spacetimes, the condition $g^{rr} = 0$ typically determines the location of the apparent horizon, without requiring the spacetime to be stationary. In stationary cases such as the Schwarzschild spacetimes, the apparent and event horizons coincide and are both located at $r = r_s$.

1.2.3 Tell-Tale Signs of Singularity Existence

When studying a spacetime it is important to know whether it is regular, that is, if it contains any curvature singularities. A quick check of the curvature invariants such as the Kretschmann scalar, $K = R_{\mu\nu\rho\sigma}R^{\mu\nu\rho\sigma}$, can point out troublesome points. The Kretschmann scalar for the Schwarzschild metric (1.2.3) takes the form

$$K = 12\frac{r_s^2}{r^6}. \tag{1.2.6}$$

Notice that K remains finite when $r = r_s$, reassuring that r_s is just a coordinate singularity, but diverges when $r \to 0$, indicating a potential curvature singularity. While the divergence of curvature invariants signals extreme gravitational effects, it does not, by itself, constitute a rigorous definition of a singularity [7]. A more rigorous method for identifying singularities involves examining geodesic incompleteness, as demonstrated by the Hawking-Penrose singularity theorems. In this approach, a spacetime is said to be singular if there exist geodesics that cannot be extended beyond a finite value of their affine parameter. This formulation avoids the ambiguities of coordinate-dependent descriptions or scalar curvature divergences [7].

To test for geodesic incompleteness, consider a congruence of geodesics — a family of non-intersecting curves — and examine their behavior throughout the spacetime in question. The Raychaudhuri equation provides a crucial tool for this analysis, describing how the expansion of a geodesic congruence evolves along the flow and offering insight into the behavior of geodesics in a given spacetime [6, 10]. The focusing of geodesics to conjugate points signals the breakdown of geodesic continuity, thereby indicating geodesic incompleteness. The

Raychaudhrui equation for timelike geodesics is given by the following[1] [12]

$$\frac{d\theta}{d\tau} = -\frac{1}{3}\theta^2 - \sigma_{\mu\nu}\sigma^{\mu\nu} + \omega_{\mu\nu}\omega^{\mu\nu} - R_{\mu\nu}U^\mu U^\nu. \tag{1.2.7}$$

The terms in this equation have clear physical interpretations tied to the geometry of a cross-sectional area enclosing a fixed number of geodesics. The expansion θ characterizes the rate at which the area of this cross-section changes, with $\theta > 0$ indicating divergence (defocusing) and $\theta < 0$ indicating convergence (focusing) of geodesics. The shear, $\sigma_{\mu\nu}$, describes distortions in the cross-section's shape — for example, how a circular cross-section may become elliptical. The vorticity term, $\omega_{\mu\nu}$ represents the twisting or rotation of the cross-section. Both shear and vorticity are spacelike, ($\sigma_{\mu\nu}\sigma^{\mu\nu} \geq 0$ and $\omega_{\mu\nu}\omega^{\mu\nu} \geq 0$) and as such the shear term will contribute to the focusing of the geodesics while the vorticity contributes to defocusing [10]. The last term involves the Ricci tensor contracted with the normalized velocity vector. It is related to the strong energy condition, $R_{\mu\nu}U^\mu U^\nu \geq 0$, and also reflects tidal gravitational effects and also contributes to focusing. An important observation is that the Raychaudhuri equation governs the behavior of geodesic congruences in spacetime purely geometrically, without reference to any specific gravitational theory (i.e general relativity). This makes it a powerful tool in semiclassical/effective gravity where general relativity becomes inadequate.

The definitions of trapped surfaces and apparent horizons can be refined by incorporating the behaviour of the expansion. A trapped surface is a 2-dimensional, compact, spacelike surface on which both the expansion of outgoing null geodesics θ_+ and ingoing null geodesics θ_- are negative, indicating that light rays in both directions are converging. A marginally trapped surface is the outer most trapped surface for which the expansion of the outgoing null geodesics vanishes, $\theta_+ = 0$, while the expansion of the ingoing null geodesics remains negative, $\theta_- < 0$. An apparent horizon is then defined as the outermost marginally trapped surface, and its position can be determined by solving for the radius r at which $\theta_+ = 0$ for (outgoing) null geodesics.

The Hawking-Penrose singularity theorems show that, under physically reasonable assumptions such as the strong energy condition and appropriate causal structure, the existence of a trapped surface necessarily leads to geodesic incompleteness, interpreted as indicating the presence of a singularity. [5, 12, 13].

1.2.4 Observational Evidence for Black Holes

Theoretical black hole solutions, such as the Scwarzschild (non-rotating) and Kerr (rotating) metrics, have become central to modern astrophysics due to a growing body of observational

[1] In the case of Null geodesics, there is a factor of $\frac{1}{2}$ rather than the $\frac{1}{3}$ in front of θ.

evidence. Although event horizons cannot be directly observed, numerous phenomena are best explained by the presence of compact, massive, and non-luminous objects with strong gravitational fields—consistent with black holes as predicted by general relativity.

The detection of gravitational waves from binary black hole mergers by the LIGO and Virgo collaborations has provided compelling indirect evidence [14, 15]. These signals match the predictions of numerical relativity with remarkable precision, including the ringdown phase consistent with the quasi-normal modes of a perturbed black hole [16]. Additionally, the Event Horizon Telescope (EHT) has produced horizon-scale images of the supermassive black holes in M87* and Sgr A*, showing shadows consistent with general relativistic predictions [17, 18]. X-ray binaries, relativistic jets, and the high-velocity stellar orbits observed near the galactic center further support the existence of astrophysical black holes across a wide mass range [19–21].

While these observations confirm the existence of black hole-like objects, they do not resolve the question of internal structure or the fate of infalling matter. In particular, the existence of classical singularities remains outside the scope of current observations. These limitations motivate ongoing theoretical work—including the models developed in this dissertation—aimed at resolving singularities and understanding the quantum gravitational structure of black holes.

1.3 Loop Quantum Gravity, in Brief

Loop Quantum Gravity is a non-perturbative and background independent approach to the quantization of gravity. It addresses the limitations of conventional quantum field theories, which rely on a fixed spacetime background and thus struggle to describe the dynamical nature of spacetime in general relativity. In GR, as famously summarized, "matter tells spacetime how to curve (and) spacetime tells matter how to move" [22], emphasizing that spacetime itself is a dynamical entity.

The main approaches within LQG are the canonical (Hamiltonian) formulation and the covariant (spin foam) formulations. The canonical formulation, which is the focus of this discussion, is rooted in the Hamiltonian framework and emphasizes the quantization of spacetime geometry by introducing new canonical variables. This discussion is intended only to provide a brief overview and set the stage for later chapters.

1.3.1 ADM Formalism

The starting point is the ADM (Arnowitt–Deser–Misner) formulation of general relativity—a canonical formulation expressed in terms of metric components—which casts GR into a

Hamiltonian framework. The underlying mathematical structure of a Hamiltonian framework is provided by Poisson geometry, which defines the structure of phase space and the rules for computing dynamical evolution via Poisson brackets [23]. Constructing a Hamiltonian directly from the Einstein-Hilbert action requires defining appropriate conjugate variables. Conjugate momenta are defined using time derivatives of the metric, requiring a foliation of spacetime to separate temporal and spatial components. The ADM formalism achieves this by introducing a foliation of the four-dimensional spacetime manifold $\mathcal{M}$ into a family of spatial hypersurfaces Σ labeled by a parameter $t \in \mathbb{R}$ such that $\mathcal{M} \cong \mathbb{R} \times \Sigma$. This assumes spacetime is globally hyperbolic. The evolution from one hypersurface to the next is governed by a vector field t^a, which generates the displacement from one spatial slice to the next. This vector field can be decomposed into its normal and tangential parts as follows:

$$t^a = Nn^a + N^a. \tag{1.3.1}$$

Here, n^a is the (future pointing) unit normal to the hypersurfaces such that $g_{ab}n^a n^b = -1$. The function N is called the lapse while N^a is the shift vector with spatial components $(a = 1, 2, 3)$ [24].

Using this decomposition the spacetime metric takes the form

$$ds^2 = -(N^2 - N^a N_a)dt^2 + 2N_a dt dx^a + q_{ab} dx^a dx^b, \tag{1.3.2}$$

where q_{ab} encodes the spatial components of the metric on the hypersurfaces Σ_t. It is referred to as the induced metric as it is induced from the full spacetime metric g_{ab} by projection

$$q_{ab} = g_{ab} - n_a n_b. \tag{1.3.3}$$

A tensor is called spatial (with respect to a given foliation) if it vanishes when contracted with the normal vector n^a. Spatial tensors can be categorized as intrinsic if they are defined solely in terms of q_{ab}, or extrinsic if they involve n^a as well [23].

The spatial metric itself is an intrinsic tensor on the hypersurface Σ and defines a unique covariant derivative D_a on Σ that is compatible with the spatial geometry, i.e $D_a q_{bc} = 0$. This spatial derivative operator can be related to the spacetime covariant derivative ∇_a as $q_a{}^d q_b{}^e q_c{}^f \nabla_f q_{de} = 0$, which expresses the compatibility of the induced metric q_{ab} with the projection of ∇_a on Σ. The covariant derivative D_a can also define an intrinsic curvature tensor, the 3-dimensional Riemann tensor ${}^{(3)}R_{abc}{}^d v_d = D_a D_b v_c - D_b D_a v_c$ for spatial vector v_c. Although D_a may act on any spacetime tensor, the result will always be a spatial tensor [23]. While the intrinsic geometry applies to a single hypersurface (Σ, q_{ab}), the extrinsic geometry encodes how Σ is embedded in the full spacetime manifold $\mathcal{M}$ and how it bends within it. The extrinsic curvature tensor defined as

$$\begin{aligned} K_{ab} &:= D_a n_b \\ &= q_a^c q_b^d \nabla_c n_d \\ &= \frac{1}{2N}(\dot{q}_{ab} - D_a N_b - D_b N_a). \end{aligned} \tag{1.3.4}$$

Here, $\dot{q}_{ab} = \mathcal{L}_t q_{ab}$ is the Lie derivative of the induced metric along the time vector field t^a.

The Einstein-Hilbert action Eq.(1.1.3), with $\sqrt{-\det g} = N\sqrt{\det q}$, can then be reformulated within the ADM formalism as

$$S_{ADM} = \frac{1}{16\pi G}\int dt \int_\Sigma d^3x \sqrt{\det q}\; N({}^3R + q^{da}q^{bc}K_{db}K_{ac} - K^2), \tag{1.3.5}$$

where ${}^3R$ is the 3-dimensional Ricci scalar. The action depends on the time derivatives of the spatial metric q_{ab} through the extrinsic curvature K_{ab}, while the lapse function N and shift vector N^a appear without any time derivatives. As a result, they serve as Lagrange multipliers, leading to the primary constraints $p_N = \frac{\delta L}{\delta \dot{N}} = 0$ and $p_a = \frac{\delta L}{\delta \dot{N}^a} = 0$. In contrast, the time derivatives $\dot{q}_{ab}$ yield conjugate momenta $p^{ab} = \frac{\delta L}{\delta \dot{q}_{ab}}$, which define an invertible relation, allowing $\dot{q}_{ab}$ to be written in terms of the canonical variables. After performing a Legendre transformation, the consistency of the primary constraints leads to secondary constraints: the (spatial) diffeomorphism constraint $\mathcal{H}_a$ and the Hamiltonian (scalar) constraint $\mathcal{H}$. The total gravitational Hamiltonian then becomes a sum of constraints

$$H_{\text{grav}} = \frac{1}{16\pi G}\int d^3x (N^a \mathcal{H}_a + N\mathcal{H}), \tag{1.3.6}$$

and thus H_{grav} vanishes on the constraint surface. Consequently, physical time evolution is generated by gauge transformations, reflecting the diffeomorphism invariance of GR.

The canonical ADM framework leads naturally to the Wheeler–DeWitt equation as an attempt at quantizing gravity. However, this approach encounters serious obstacles — from ambiguities in defining the quantum Hamiltonian to the lack of a well-defined inner product or operator ordering in the Hilbert space [24]. A more promising path towards a theory of quantum gravity begins with the Palatini formulation, which generalizes the variables used in GR and facilitates the introduction of the the Ashtekar-Barbero Variables. These variables lie at the heart of the canonical approach to LQG and are the topic of the next subsection.

1.3.2 Tetrad Formulation and Ashtekar-Barbero Variables

While the ADM formalism provides a canonical framework for GR, LQG builds on a first-order formalism to simplify quantization, starting from the Palatini action. Both the Einstein-Hilbert action and the ADM formulation are examples of second-order formalisms of GR, in which variation with respect to the metric yields equations involving second derivatives—owing to the metric dependence of the Levi-Civita connection. However, second-order formulations can present challenges in canonical quantization [23, 25]. These difficulties can be alleviated by switching to a first-order formalism, where the connection is treated as an independent field, separate from the metric [25].

The first-order formalism of general relativity requires a reformulation of the Hamiltonian (1.3.6) in terms of orthonormal vector fields (tetrads), providing a natural framework for gauge symmetries and quantization. A tetrad denoted e^a_I, consists of four linearly independent vector fields labeled by internal Lorentz indices $I, J = (0, 1, 2, 3)$ and spacetime indices $a, b = (0, 1, 2, 3)$. These relate the spacetime metric g^{ab} to the internal Minkowski metric η^{IJ} via

$$g^{ab} = e^a_I e^b_J \eta^{IJ}. \tag{1.3.7}$$

This relation shows that the tetrad field fully encodes the information contained in the metric [23]. The corresponding co-tetrad (or dual tetrad), denoted e^I_a, satisfies the orthonormality conditions

$$e^a_I e^J_a = \delta^I_J \qquad\qquad e^a_I e^I_b = \delta^a_b. \tag{1.3.8}$$

One can also raise the internal index with η^{IJ} while lowering the spacetime index with the spacetime metric g_{ab}, $e^I_a = \eta^{IJ} g_{ab} e^b_J$. Under a local Lorentz transformation $e^a_I \to \Lambda_I{}^J e^a_J$, the spacetime metric remains invariant, reflecting the internal gauge freedom [23, 24].

To describe parallel transport in the tetrad formulation, one introduces a Lorentz connection 1−form $\omega_a{}^I{}_J$ which satisfies the compatibility condition $\mathcal{D}_a \eta_{IJ} = 0$ and is antisymmetric in its internal indices [26]. This defines a covariant derivative $\mathcal{D}_a$ acting on tensors with Lorentz indices. Applied to a mixed object like the co-tetrad, it takes the form

$$\begin{aligned} \mathcal{D}_a e^I_b &= \nabla_a e^I_b + \omega_a{}^I{}_J e^J_b \\ &= \partial_a e^I_b + \omega_a{}^I{}_J e^J_b - \Gamma^c_{ab} e^I_c, \end{aligned} \tag{1.3.9}$$

where, Γ^c_{ab} are the usual Christoffel symbols of the Levi-Civita connection.

The associated curvature two-form is:

$$F_{ab}{}^{IJ} = \partial_a \omega_b{}^{IJ} - \partial_b \omega_a{}^{IJ} + \omega_a{}^I{}_K \omega_b{}^{KJ} - \omega_b{}^I{}_K \omega_a{}^{KJ}. \tag{1.3.10}$$

In the Palatini formalism, both e^I_a and $\omega_a{}^{IJ}$, are treated as independent variables. The action of general relativity in these variables is given by,

$$S_{\text{Palatini}} = \frac{1}{16\pi G} \int d^4x \; |e| \; e^a_I e^b_J F_{ab}{}^{IJ}(\omega), \tag{1.3.11}$$

where $|e| = |\text{det}e| = \sqrt{-\text{det}g}$. Varying the action with respect to $\omega_a{}^{IJ}$ yields tetrad compatibility condition $\mathcal{D}_a e^I_b = 0$ which in turn implies that the connection must be the unique torsion-free spin connection compatible with the tetrads [24]. Substituting the resulting equation of the spin connection in terms of tetrads back into the action and varying with respect to the tetrad then yields Einstein's field equations, showing that GR is recovered in this first-order formalism.

To this action, one adds the Holst term, introducing the Immirzi parameter γ . The Holst term, parameterized by the Immirzi parameter, reformulates general relativity in a way that allows it to be cast as an $SU(2)$ gauge theory. In this formulation, the connection becomes the primary dynamical variable, and the Ashtekar-Barbero connection is introduced to facilitate canonical quantization. The key property of the Holst term is that the parameter γ controls the coupling of the Holst term, affecting the quantum theory's spectrum but not the classical dynamics when torsion is zero (as is the case in standard GR) [23,27]. With the additional term the Palatini action (1.3.11) becomes

$$S_{\text{Holst}} = \frac{1}{16\pi G} \int d^4x |e| e^a_I e^b_J (\delta^{[I}_K \delta^{J]}_L - \frac{1}{2\gamma} \epsilon^{IJ}{}_{KL}) F_{ab}{}^{KL}(\omega). \tag{1.3.12}$$

The Holst action serves as the starting point for the canonical formulation of GR in LQG.

To proceed, one performs a $3+1$ decomposition of spacetime, similar to the ADM case, and splits the tetrad into a spatial triad e^i_a ($i = 1, 2, 3$) defined on the spatial hypersurfaces Σ, along with a timelike normal vector. The spin connection $\omega_a{}^{IJ}$ is similarly decomposed into spatial and temporal parts. To reduce the internal Lorentz symmetry $SO(3,1)$ to $SU(2)$ one imposes the time gauge, fixing the boost part of the internal Lorentz symmetry [23,26]. Specifically, the time gauge sets $e^a_0 = n^I e^a_I = n^a$ where n^I is the internal unit vector in the Lorentz group aligned with the "time" direction, and n_a is the unit normal to the spatial hypersurface Σ [23,27]. As a result, the triad e^a_i, which encodes the 3D geometry, is isolated, and the Lorentz connection is reformulated as the Ashtekar-Barbero connection A^i_a,

$$A^i_a = \gamma\omega^{0i}_a + \frac{1}{2}\varepsilon^i_{jk}\omega^{jk}_a, \tag{1.3.13}$$

an SU(2) connection that recasts general relativity as a gauge theory [23, 27]. While this reformulation is equivalent to other canonical formulations of classical general relativity, it is particularly suited for LQG because the compact SU(2) structure enables the use of mathematical tools for a background-independent quantization. The γ appearing in the connection is the Immirzi parameter that was introduced in the Holst action. The different spacetime components of the connection can be interpreted as the spatial spin connection $\Gamma^i_a := \frac{1}{2}\varepsilon^i_{jk}\omega^{jk}_a$ and the extrinsic curvature contracted with the spatial triad $K^i_a := \omega^{0i}_a$ giving,

$$A^i_a = \Gamma^i_a + \gamma K^i_a. \tag{1.3.14}$$

The conjugate momentum variable, known as the densitized triad E^a_i is constructed from the spatial triad e^a_i,

$$E^a_i = |\mathrm{det}e|e^a_i, \tag{1.3.15}$$

where $|\mathrm{det}e|$ is the determinant of the triad. Together, A^i_a and E^a_i form a conjugate pair, and are the canonical variables of GR with Poisson brackets [23, 27]

$$\left\{A^i_a(\mathbf{x}), E^b_j(\mathbf{y})\right\} = 8\pi G\gamma\delta^i_j\delta^b_a\delta^3\left(\mathbf{x}-\mathbf{y}\right). \tag{1.3.16}$$

With these canonical variables, the Holst action admits a Hamiltonian formulation with gravitational Hamiltonian

$$H_{grav} = \int d^3x(-\Lambda^i G_i + N\mathcal{H} + N^a\mathcal{H}_a). \tag{1.3.17}$$

The introduction of triads and the Ashtekar connection introduces a new constraint known as the Gauss constraint, G_i. This constraint generates SU(2) gauge transformations and ensures the densitized triad E^j_b transforms as an $SU(2)$ vector and the Ashtekar connection A^i_a as an $SU(2)$ connection. The remaining constraints are the familiar Hamiltonian $\mathcal{H}$ and Diffeomorphism constraint $\mathcal{H}_a$ which now admit expressions in terms of K^i_a, E^a_i and F^i_{ab}.

1.3.3 Quantization

The Holst term was introduced to facilitate the formulation of GR in terms of the Ashtekar-Barbero connection, reformulating GR as an $SU(2)$ gauge theory. Usually in gauge theory, after imposing the Gauss law constraint, one has a physical Hamiltonian. In contrast, in the Ashtekar-Barbero formulation, even after imposing the Gauss law, the system remains fully constrained due to the diffeomorphism and Hamiltonian constraints, reflecting the background independent nature of GR.

The goal of quantization is to define a Hilbert space and operators that encode the dynamics of gravity non-perturbatively, to capture the background-independent nature of GR.

However, in the Ashtekar-Barbero framework, a significant challenge arises: the connection A_a^i cannot be directly promoted to a well-defined quantum operator. This is due to its local, distributional nature and the choice of a representation that enforces background independence. To overcome the difficulties, LQG employs the holonomy-flux algebra. Holonomies, defined as path-ordered exponentials of the Ashtekar connection along edges, are well-defined SU(2) group elements. They are paired with flux variables, derived from the conjugate densitized triad E_i^a, which are smeared over two-dimensional surfaces [27]. The flux operator encodes geometric information such as area and volume. Although holonomies are not inherently gauge-invariant they transform in a much simpler way than the connection. The trace of a holonomy, known as a Wilson loop, is gauge invariant and played a foundational role in early formulations of LQG. In modern approaches, however, spin networks serve as the primary gauge-invariant quantum states. A spin network is a graph embedded in the spatial manifold, with edges labeled by SU(2) representations (spins) and vertices labeled by intertwiners that ensure gauge invariance by combining the spin labels of the connecting edges in an invariant way. These states generalize Wilson loops as each edge carries a holonomy, and the intertwiners at vertices enforce SU(2) gauge symmetry [27, 28]. These spin network states form an orthonormal basis for the kinematical Hilbert space and are eigenstates of geometric operators such as area and volume. These operators have discrete spectra, indicating that spatial geometry is quantized, with minimal non-zero eigenvalues proportional to powers of Planck length, l_p^2 and l_p^3 for area and volume respectively [23, 24, 27]. While spin networks provide a complete basis for the kinematical Hilbert space, solving the Hamiltonian constraint to obtain the physical Hilbert space remains a major challenge. Evolving spin networks to describe physical processes such as cosmological expansion or black hole dynamics is hindered by the theory's highly non-perturbative structure [27, 29]. To address this, simplified quantization schemes can be used to make contact with physically relevant situations [30]. In many symmetry-reduced settings, one can derive effective models that incorporate key features of the full quantum theory without working with its full complexity. These models approximate the quantum dynamics by modifying the classical equations with quantum corrections inspired by the underlying operator structure. Such effective theories are typically valid in regimes where quantum gravity effects are important but a full quantization is intractable, for instance, in homogeneous cosmologies or black hole interiors. They are trusted when they reproduce the correct semiclassical limit, capture key features like bounded curvature, and reflect the discrete geometry implied by LQG.

One such method is polymer quantization, a framework that reformulates quantum mechanics on a discrete configuration space and is well-suited for symmetry reduced models [31, 32]. In this framework, the classical phase space consists of canonical pairs (q, p), in symmetry-reduced gravity models, these correspond to (A_a^i, E_i^a). Unlike standard Schrödinger quantization, where both q and p are promoted to operators, in polymer quantization the configuration variable (e.g. A_a^i) cannot be promoted to a well-defined operator [31, 33]. Instead, one works with exponentials such as $\exp(i\mu A_a^i)$, which are well defined translation operators on the quantum configuration space. The parameter μ is a regularization scale, often related to the minimal area eigenvalue (area gap) in LQG or LQC. This motivates the use of holonomy-like expressions, which are functions of the connection exponentiated along edges which the objects that remain well-defined in LQG [27]. At the effective level, this restriction manifests in a replacement of the Ashtekar connection with a trigonometric function that encodes the holonomy corrections while avoiding the full path-ordered exponentials:

$$A_a^i \mapsto \frac{\sin(\mu A_a^i)}{\mu}. \tag{1.3.18}$$

Physically, the parameter μ is often tied to the area gap in full LQG, representing the minimal non-zero eigenvalue of the area operator [34]. In effective models like (LQC) or LQG-inspired black hole interiors, this substitution regularizes the classical Hamiltonian and leads to modifications of the equations of motion that are especially significant in high curvature regimes. Notably, the trigonometric form suppresses curvature divergences and is instrumental in the resolution of classical singularities, such as the Big Bang or back hole singularities [1, 35].

2 Black hole singularity resolution via the modified Raychaudhuri equation in loop quantum gravity

This chapter presents the analysis conducted in [36], focusing on loop quantum gravity corrections to the Raychaudhuri equation in the interior of a Schwarzschild black hole and near the classical singularity. The resulting effective equation demonstrates that geodesics undergo defocusing due to the emergence of repulsive terms. This effect prevents the formation of conjugate points, renders the singularity theorems inapplicable, and ultimately leads to the resolution of the singularity in this spacetime.

2.1 Black Hole Singularities and Quantum Gravity

Singularities in general relativity are widely believed to signal the breakdown of the classical theory in regimes where quantum gravitational effects become significant—particularly in regions of extremely high curvature that precede the formation of a singularity. In such regimes, a complete theory of quantum gravity is expected to replace classical descriptions and resolve the singular behavior by incorporating quantum corrections.

Prominent examples of singularities include those predicted at the Big Bang, the Big Crunch, and within black holes. Loop Quantum Cosmology (LQC), the application of LQG techniques to homogeneous and isotropic cosmological models, has led to significant progress in understanding and resolution of such singularities. In particular, for homogeneous and isotropic cosmological models, LQC has shown that the classical big bang and big crunch singularities are replaced by a quantum bounce, arising from the discrete quantum geometry inherent in the theory [1, 37]. In contrast, the Schwarzschild interior is homogeneous but anisotropic near the singularity, which introduces additional complexity in formulating a quantum resolution. As a result, applying LQG techniques to black hole interiors requires different symmetry-reduced models, such as the Kantowski–Sachs spacetime (discussed below), and often requires more subtle treatments to extend singularity resolution in these cases [38]. Much progress has been made in this direction [30,35,39–83], with many proposals suggesting that the classical singularity at the center of the Schwarzschild black hole be replaced by a regular, albeit quantum region, analogous to the resolution of the big bang in LQC.

As discussed in Sec. 1.2.2, it was shown that the roles of the temporal and radial coordinates inside the event horizon switch.This leads to an interior geometry that is locally isometric to Kantowski–Sachs spacetime, a homogeneous but anisotropic cosmological model with all metric components depending only on a single time-like coordinate. This means that the interior can be modeled as a minisuperspace, reducing the number of independent degrees of freedom and enabling loop quantization techniques similar to those used in LQC [30]. This symmetry reduction provides a significant advantage for analyzing the black hole interior in loop quantum gravity, as the loop quantization of the Schwarzschild interior can be formulated in much the same way as in LQC [37, 84]. It is important to note, however, that the classical equivalence between the Schwarzschild interior and Kantowski–Sachs spacetime may not extend to the quantum theory. Assuming this correspondence holds at the quantum level is a working assumption of this approach, and although commonly adopted, it should be kept in mind as a potential limitation.

The loop quantization of the Kantowski-Sachs spacetime introduces key modifications to the classical evolution equations, leading to quantum gravitational corrections in the form of repulsive terms that affect geodesic evolution. These effects can be determined via modified Raychaudhuri equation and it will be shown that the singularity is no longer present at the effective level.

2.2 Interior Schwarzschild Black Hole

Recall from Eq. (1.2.3) that the metric of the exterior Schwarzschild black hole of mass M is given by

$$ds^2 = -\left(1 - \frac{2GM}{r}\right) dt^2 + \left(1 - \frac{2GM}{r}\right)^{-1} dr^2 + r^2 \left(d\theta^2 + \sin^2\theta d\phi^2\right). \tag{2.2.1}$$

With $r \in (0, \infty)$ the radial coordinate distance and the radius of the 2−spheres in Schwarzschild coordinates (t, r, θ, ϕ). The metric of the interior of the Schwarzschild black hole can be obtained by switching t and r since the temporal and spatial radial coordinates exchange their causal nature upon crossing the horizon (as discussed in Section 1.2.2). The resulting metric of the interior is then given by

$$ds^2 = -\left(\frac{2GM}{t} - 1\right)^{-1} dt^2 + \left(\frac{2GM}{t} - 1\right) dr^2 + t^2 \left(d\theta^2 + \sin^2\theta d\phi^2\right), \tag{2.2.2}$$

where t, r, θ, ϕ are the Schwarzschild coordinates but now $t \in (0, 2GM)$ and t^2 plays the role of the infalling 2−sphere. The metric components are now independent of r and the system has a finite degrees of freedom, making it a minisuperspace model. This metric is recognized as a Kantowski-Sachs cosmological spacetime with the general form [85]

$$ds^2_{KS} = -N(T)^2 dT^2 + g_{xx}(T) dx^2 + g_{\theta\theta}(T) \left(d\theta^2 + \sin^2\theta d\phi^2\right). \tag{2.2.3}$$

Here, $N(T)$ is the lapse function corresponding to a generic time T. The coordinate x parameterizes the homogeneous spatial direction and is not related to the areal radius of the 2-spheres, which is determined solely by $g_{\theta\theta}$. In contrast, the Schwarzschild coordinate r is the areal radius in the exterior region, satisfying $A = 4\pi r^2$.

Comparing the metrics (2.2.2) and (2.2.3), it is straightforward to see they are related by a transformation,

$$N(T)^2 dT^2 = \left(\frac{2GM}{t} - 1\right)^{-1} dt^2. \tag{2.2.4}$$

A common approach to quantizing the interior of a Schwarzschild black hole is polymer quantization, which is inspired by techniques from loop quantum cosmology. In LQC, polymer quantization is applied to the homogeneous and isotropic Friedmann-Lemaî̂tre-Robertson-Walker (FLRW) spacetime [1, 86]. LQC has demonstrated success in resolving singularities in FLRW spacetimes, and its methods extend naturally to other homogeneous models, including Kantowski-Sachs [84]. Because of the isometry between (2.2.2) and (2.2.3), it is natural to apply LQC-inspired polymer quantization techniques for studying singularity resolution in Schwarzschild (interior) black hole spacetimes [58].

First, recall the full Hamiltonian can be written in terms of the Ashtekar-Barbero connection A_a^i and the densitized triad E_i^a determined from the canonical Holst action and given by (1.3.17). The procedure here will be to write the symmetry reduced version of (1.3.17) in terms of the Kantowski-Sachs symmetry of the current model. After gauge fixing the Gauss constraint, the Ashtekar-Barbero variables take the form [30, 84]

$$A_a^i \tau_i dx^a = \frac{c}{L_0}\tau_3 dx + b\tau_2 d\theta - b\tau_1 \sin\theta d\phi + \tau_3 \cos\theta d\phi, \tag{2.2.5}$$

$$E_i^a \tau_i \partial_a = p_c \tau_3 \sin\theta \partial_x + \frac{p_b}{L_0}\tau_2 \sin\theta \partial_\theta - \frac{p_b}{L_0}\tau_1 \partial_\phi. \tag{2.2.6}$$

Where b, c, p_b, and p_c are functions that only depend on time and $\tau_i = -i\sigma_i/2$ are a $su(2)$ basis satisfying $[\tau_i, \tau_j] = \epsilon_{ij}{}^k \tau_k$, with σ_i being the Pauli matrices. L_0 is chosen to restrict the range of integration of the symplectic form over $\mathbb{R}$ to the range $\mathcal{I} = [0, L_0]$ so that the integral does not diverge, i.e. to regularize the integral. This can be done thanks to homogeneity and later one can take the limit $L_0 \to \infty$. Using the relation,

$$\det q \; q^{ab} = \delta^{ij} E_i^a E_j^b, \tag{2.2.7}$$

with (2.2.6), and (2.2.3), one obtains

$$g_{xx}\left(T\right)=\frac{p_b\left(T\right)^2}{L_0^2 p_c\left(T\right)}, \tag{2.2.8}$$

$$g_{\theta\theta}\left(T\right)=\frac{g_{\phi\phi}\left(T\right)}{\sin^2\left(\theta\right)}=g_{\Omega\Omega}\left(T\right)=p_c\left(T\right). \tag{2.2.9}$$

The metric written in terms of the new variables becomes

$$ds^2=-N(T)^2dT^2+\frac{p_b(T)^2}{L_0^2\left|p_c(T)\right|}dx^2+|p_c(T)|(d\theta^2+\sin^2\theta d\phi^2), \tag{2.2.10}$$

where the lapse is left undefined. Writing the above metric in Schwarzschild coordinates (t, r) and comparing directly to the interior Schwarzschild metric (2.2.2), one obtains

$$N\left(t\right)=\left(\frac{2GM}{t}-1\right)^{-\frac{1}{2}}, \tag{2.2.11}$$

$$g_{xx}\left(t\right)=\frac{p_b\left(t\right)^2}{L_0^2 p_c\left(t\right)}=\left(\frac{2GM}{t}-1\right), \tag{2.2.12}$$

$$g_{\theta\theta}\left(t\right)=\frac{g_{\phi\phi}\left(t\right)}{\sin^2\left(\theta\right)}=g_{\Omega\Omega}\left(t\right)=p_c\left(t\right)=t^2. \tag{2.2.13}$$

This shows that classically

$$p_b=0, \qquad p_c=4G^2M^2, \qquad \text{on the horizon } t=2GM, \tag{2.2.14}$$

$$p_b\to 0, \qquad p_c\to 0, \qquad \text{at the singularity } t\to 0. \tag{2.2.15}$$

2.3 Classical Dynamics

To obtain the dynamical properties of this model, the symmetry reduced Hamiltonian needs to be determined. Due to the homogeneity of the Kantowski–Sachs spacetime, the diffeomorphism constraint vanishes identically. Moreover, the choice of connection and triad adapted to Kantowski–Sachs symmetry ensures that the Gauss constraint is automatically satisfied [30]. Consequently, the only remaining nontrivial constraint is the Hamiltonian (also known as the scalar) constraint [27],

$$H_{\text{full}}=\frac{1}{8\pi G}\int d^3x\frac{N}{\sqrt{\det|E|}}\left(\epsilon_i^{jk}F_{ab}^iE_j^aE_k^b-2(1+\gamma^2)K_{[a}^iK_{b]}^jE_i^aE_j^b\right). \tag{2.3.1}$$

Recall, F^i_{ab} is the curvature of the Ashtekar-Barbero connection, K^i_a is the extrinsic curvature of foliations, N is the lapse function and γ is the Barbero-Immirzi parameter [87]. Substituting the canonical variables with equations (2.2.5) and (2.2.6), the symmetry reduced classical Hamiltonian in Kantowski-Sachs spacetime is, [30, 35, 41, 58, 81]

$$H = -\frac{N}{2G\gamma^2}\left[2bc\sqrt{p_c} + \left(b^2+\gamma^2\right)\frac{p_b}{\sqrt{p_c}}\right]. \tag{2.3.2}$$

To obtain the equations of motion, the relevant Poisson brackets

$$\left\{A^i_a(\mathbf{x}), E^b_j(\mathbf{y})\right\} = 8\pi G\gamma\delta^i_j\delta^b_a\delta^3\left(\mathbf{x}-\mathbf{y}\right), \tag{2.3.3}$$

reduce to

$$\{c, p_c\} = 2G\gamma, \qquad \{b, p_b\} = G\gamma. \tag{2.3.4}$$

A convenient choice of lapse function will simplify the equations of motion greatly,

$$N\left(T\right) = \frac{\gamma\sqrt{p_c\left(T\right)}}{b\left(T\right)}, \tag{2.3.5}$$

which makes the Hamiltonian

$$H = -\frac{1}{2G\gamma}\left[\left(b^2+\gamma^2\right)\frac{p_b}{b} + 2cp_c\right]. \tag{2.3.6}$$

This governs classical dynamics, setting the stage for quantum corrections. The gauge choice of lapse simplifies the equations of motion by decoupling those of c, p_c from those of b, p_b making it possible to solve them,

$$\frac{db}{dT} = \{b, H\} = -\frac{1}{2}\left(b + \frac{\gamma^2}{b}\right), \tag{2.3.7}$$

$$\frac{dp_b}{dT} = \{p_b, H\} = \frac{p_b}{2}\left(1 - \frac{\gamma^2}{b^2}\right), \tag{2.3.8}$$

$$\frac{dc}{dT} = \{c, H\} = -2c, \tag{2.3.9}$$

$$\frac{dp_c}{dT} = \{p_c, H\} = 2p_c. \tag{2.3.10}$$

In addition to the four equations above, the on-shell condition corresponding to the vanishing of the Hamiltonian constraint (2.3.6) must also be satisfied on the constraint surface,

$$\left(b^2+\gamma^2\right)\frac{p_b}{b} + 2cp_c \approx 0, \tag{2.3.11}$$

where $\approx$ stands for weak equality, i.e., on the constraint surface. The solution to the classical equations of motion (2.3.7)–(2.3.10) are found to be

$$b\left(T\right)=\pm\sqrt{e^{2C_1}e^{-T}-\gamma^2}, \tag{2.3.12}$$
$$p_b\left(T\right)=C_2e^{\frac{T}{2}}\sqrt{e^{2C_1}-\gamma^2e^T}, \tag{2.3.13}$$
$$c\left(T\right)=C_3e^{-2T}, \tag{2.3.14}$$
$$p_c\left(T\right)=C_4e^{2T}. \tag{2.3.15}$$

A change of coordinates from T to Schwarzschild coordinate t can be easily done through comparison of (2.3.15) with (2.2.13). This suggests that $T=\ln\left(t\right)$ and the above solutions become

$$b\left(t\right)=\pm\sqrt{\frac{e^{2C_1}}{t}-\gamma^2}, \tag{2.3.16}$$
$$p_b\left(t\right)=C_2t\sqrt{\frac{e^{2C_1}}{t}-\gamma^2}, \tag{2.3.17}$$
$$c\left(t\right)=\frac{C_3}{t^2}, \tag{2.3.18}$$
$$p_c\left(t\right)=C_4t^2. \tag{2.3.19}$$

Considering again (2.2.13),

$$C_4=1. \tag{2.3.20}$$

From (2.2.14),

$$0=p_b\left(2GM\right)=2GMC_2\sqrt{\frac{e^{2C_1}}{2GM}-\gamma^2}, \tag{2.3.21}$$

which yields

$$C_1=\frac{1}{2}\ln\left(2GM\gamma^2\right). \tag{2.3.22}$$

Next, from (2.2.12),

$$p_b\left(t\right)^2=\left(\frac{2GM}{t}-1\right)L_0^2t^2, \tag{2.3.23}$$

which if compared with (2.3.17) and using (2.3.22) yields

$$C_2=\frac{L_0}{\gamma}. \tag{2.3.24}$$

Finally, using (2.3.11),

$$C_3=\mp\gamma GML_0. \tag{2.3.25}$$

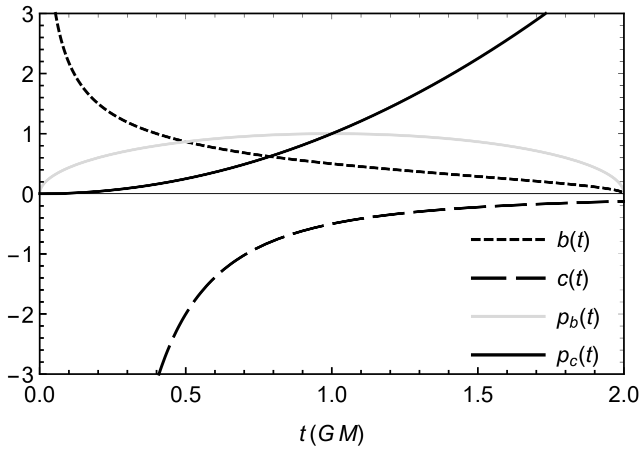

Figure 1: The behavior of canonical variables as a function of Schwarzschild time t. With positive sign for b and negative sign for c. The figure is plotted using $\gamma = 0.5$, $M = 1$, $G = 1$, and $L_0 = 1$.

Hence, the equations of motion in Schwarzschild written in t become

$$b(t) = \pm\,\gamma\sqrt{\frac{2GM}{t} - 1}, \tag{2.3.26}$$

$$p_b(t) = L_0 t\sqrt{\frac{2GM}{t} - 1}, \tag{2.3.27}$$

$$c(t) = \mp\,\frac{\gamma G M L_0}{t^2}, \tag{2.3.28}$$

$$p_c(t) = t^2. \tag{2.3.29}$$

The behavior of these solutions as a function of t is depicted in Fig. (1). From these equations or the plot, one can see that $p_c \to 0$ as $t \to 0$. This means that at the classical singularity, the Riemann invariants such as the Kretschmann scalar

$$K = R_{\mu\nu\rho\sigma}R^{\mu\nu\rho\sigma} \propto \frac{1}{p_c^3}, \tag{2.3.30}$$

all diverge, signaling the presence of a physical singularity there as expected.

The physical significance of the canonical variables can be deduced easily for p_c from (2.2.13) where it is evident that it is the square of the radius of the infalling $2-$spheres. Determining b is less obvious, using the relation

$$d\tau^2 = N(T)^2 dT^2, \tag{2.3.31}$$

along with lapse (2.3.5), (2.3.10) and (2.2.9) one can write

$$b = \frac{\gamma}{2}\frac{1}{\sqrt{p_c}}\frac{dp_c}{d\tau} = \gamma\frac{d}{d\tau}\sqrt{g_{\Omega\Omega}} = \frac{\gamma}{\sqrt{\pi}}\frac{d}{d\tau}\sqrt{A_{\theta,\phi}}, \tag{2.3.32}$$

so that b is proportional to the rate of change of the square root of the physical area of $\mathbb{S}^2$.

Similarly for c, but now using (2.3.8) along with (2.3.11) to replace $\gamma\frac{p_b}{b} = -\frac{bp_b}{\gamma} - \frac{2cp_c}{\gamma}$ in the resultant expression and finally using (2.2.8),

$$c = \gamma\frac{d}{d\tau}\left(\frac{p_b}{\sqrt{p_c}}\right) = \gamma\frac{d}{d\tau}\left(L_0\sqrt{g_{xx}}\right). \tag{2.3.33}$$

And so classically, c is proportional to the rate of change of the physical length of $\mathcal{I}$.

2.4 Classical Raychaudhuri Equation

With the above expressions found for the classical equations of motion, the next step is to determine the behavior of geodesics via the classical Raychaudhuri equation (1.2.7) in terms of the reduced canonical variables $b(t), p_b(t), c(t)$ and $p_c(t)$. Since the model under consideration is in vacuum, in GR, $R_{\mu\nu} = 0$. In the effective regime, however, the equations of motion are not necessarily Einstein's equations, and so $R_{\mu\nu}$ need not vanish. Throughout this project, however, R_{ab} was set to 0 even in the effective regime since this approximation does not qualitatively affect the behavior of the Raychaudhuri equation near the classical singularity. This was shown in later works concretely where the term corresponding to non-zero $R_{\mu\nu}$ was fully considered [88, 89]. Also, in general in Kantowski-Sachs models, the vorticity term is only nonvanishing if one considers metric perturbations [85] hence, $\omega_{\mu\nu}\omega^{\mu\nu} = 0$. This reduces the classical Raychaudhuri equation for timelike geodesics (1.2.7) equation to

$$\frac{d\theta}{d\tau} = -\frac{1}{3}\theta^2 - \sigma_{ab}\sigma^{ab}. \tag{2.4.1}$$

In order to adapt the Raychaudhuri equation to the current LQG formalism, the quantities θ and $\sigma^2 = \sigma_{\mu\nu}\sigma^{\mu\nu}$ appearing on the right-hand side of (2.4.1) must be written in terms of the canonical variables [35, 88]

$$\theta = \frac{\dot{p}_b}{Np_b} + \frac{\dot{p}_c}{2Np_c}, \tag{2.4.2}$$

$$\sigma^2 = \frac{2}{3}\left(-\frac{\dot{p}_b}{Np_b} + \frac{\dot{p}_c}{Np_c}\right)^2. \tag{2.4.3}$$

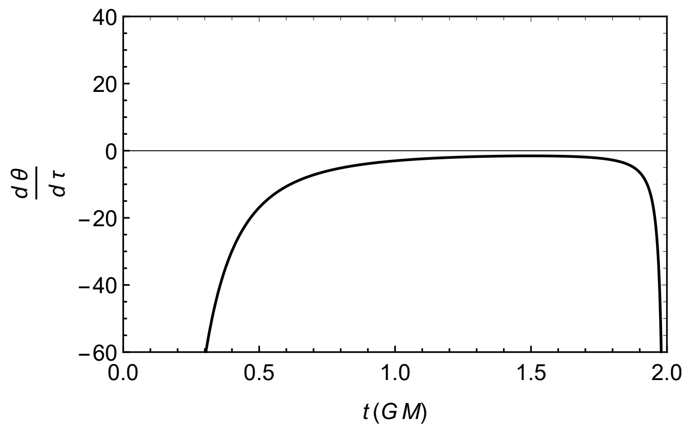

Figure 2: The right-hand side of the Raychaudhuri equation as a function of Schwarzschild time t. At both the classical singularity $t \to 0$ and at the horizon $t = 2GM$, $\frac{d\theta}{d\tau}$ diverges. The former is due to a physical singularity while the latter happens because of the choice of coordinate system with $M = 1, G = 1$.

Replacing these in (2.4.1) and using the equations of motion (2.3.7)–(2.3.10) one obtains for the classical Raychaudhuri equation

$$\frac{d\theta}{d\tau} = -\frac{1}{2p_c}\left(1 + \frac{9b^2}{2\gamma^2} + \frac{\gamma^2}{2b^2}\right). \tag{2.4.4}$$

Since $p_c > 0$ the right hand side is negative as expected and diverges at the singularity given the behavior of canonical variables in Fig. (1). This can also be seen from the expression (2.4.4) written in terms of t, by using the solutions (2.3.26)-(2.3.29) and the lapse (2.2.11) in (2.4.4) to get

$$\frac{d\theta}{d\tau} = \frac{-2t^2 + 8GMt - 9G^2M^2}{t^{\frac{5}{2}}\left(2GM - t\right)^{\frac{3}{2}}}. \tag{2.4.5}$$

The behavior of $\frac{d\theta}{d\tau}$ from (2.4.5) is presented in Fig. (2). This figure confirms that $\frac{d\theta}{d\tau}$ diverges at the classical singularity, pointing to an infinite focusing of geodesics at that region. These features reflect the well-known singularity behavior of the classical theory. In the following section, it becomes clear that the quantum effects can modify this behavior particularly close to the classical singularity.

2.5 Effective dynamics and Raychaudhuri equation

The effective dynamical behavior of the Schwarzschild black hole interior can be derived from its effective Hamiltonian constraint. The effective Hamiltonian can be derived from the classical Hamiltonian through various methods, typically by first constructing the quantum Hamiltonian constraint. In LQG, the Ashtekar–Barbero connection is not a well-defined operator on the Hilbert space. Consequently, the canonical variables b and c, which encode its components in the Kantowski–Sachs symmetry-reduced model, are not fundamental operators in the quantum theory. Instead, these variables are represented by holonomies, as described in [30, 84, 90]. The holonomies and fluxes, and thus the Hamiltonian constraint can then be represented as an operator on a suitable Hilbert space [87]. Due to the absence of a well-defined connection operator on the Hilbert space, this representation is unitarily inequivalent to the standard Schrödinger representation [87], leading to distinct physical predictions. This introduces a key feature of LQG: only finite diffeomorphisms are implemented, leading to a fundamentally discrete spatial geometry. For finite dimensional systems, such a representation is isomorphic to the polymer representation, allowing the use of polymer quantization. This quantization introduces parameters, termed polymer scales, which define the minimal length scales of the model. Quantum effects become significant near these scales. For the present model such a polymer quantization leads to polymer scales μ_b, μ_c associated with the radial and angular minimum scale and impose the fundamental discreteness of loop quantum geometry [30, 35, 58, 84, 88].

After applying polymer quantization to obtain the quantum Hamiltonian, the effective Hamiltonian can be derived using either a path integral approach or by applying the quantum Hamiltonian to states peaked around classical solutions [31, 33, 81, 91–94]. These methods yield an effective Hamiltonian which can also be heuristically obtained by replacing

$$b \rightarrow \frac{\sin(\mu_b b)}{\mu_b}, \tag{2.5.1}$$

$$c \rightarrow \frac{\sin(\mu_c c)}{\mu_c} \tag{2.5.2}$$

in the classical Hamiltonian (2.3.6) [84] . In LQG, two general schemes govern the μ parameters. The first, referred to as the μ_0 scheme or, in this work, the $\mathring{\mu}$ scheme, treats the μ parameters as constants [71] While simple, this scheme was shown to yield unphysical results in some cosmological and black hole settings, such as incorrect semiclassical behavior near the Schwarzschild horizon and strong dependence on fiducial cell choices. To improve this, improved dynamics were proposed in [1], leading to the $\bar{\mu}$-scheme, where $\bar{\mu}_b = \sqrt{\frac{\Delta}{p_b}}$ and $\bar{\mu}_c = \sqrt{\frac{\Delta}{p_c}}$, Δ being the LQG area gap. A variant known as the $\bar{\mu}'$-scheme was later introduced in [95], which alters the dependence: $\bar{\mu}_b = \sqrt{\frac{\Delta}{p_c}}$ and $\bar{\mu}_c = \frac{\sqrt{p_c \Delta}}{p_b}$. These schemes differ in their physical implications. The $\bar{\mu}$-scheme generally yields a better classical limit near the Schwarzschild horizon and ensures bounded curvature invariants. However, both schemes are not invariant under rescaling of the fiducial length L_0, which can lead to unphysical dependence on this arbitrary structure. Recent works explore how to overcome this limitation by seeking covariant regularizations or choosing improved variables.

In the Schwarzschild interior model, the absence of matter content makes it unclear which scheme is optimal or whether the $\mathring{\mu}$ scheme exhibits incorrect semiclassical behavior. In order to be thorough, the $\mathring{\mu}$-scheme is checked as well as two of the most common canonical variable dependent schemes, which are denoted by $\bar{\mu}$ and $\bar{\mu}'$ schemes.

Replacing (2.5.1) and (2.5.2) into the classical Hamiltonian (2.3.6), one obtains an effective Hamiltonian constraint

$$H_{\text{eff}} = -\frac{1}{2\gamma G}\left[p_b\left[\frac{\sin(\mu_b b)}{\mu_b} + \gamma^2\frac{\mu_b}{\sin(\mu_b b)}\right] + 2p_c\frac{\sin(\mu_c c)}{\mu_c}\right]. \tag{2.5.3}$$

Note that (2.5.3) reduces to its classical counterpart (2.3.2) in the appropriate limit. The next step is to select a scheme and follow the procedure outlined in Section 2.4 to derive the modified effective Raychaudhuri equation. This allows one to analyze the geodesic behavior and determine whether quantum effects resolve the singularity.

2.5.1 $\mathring{\mu}$ scheme

In this scheme, one assumes that the polymer or minimal scales $\mathring{\mu}_b$, $\mathring{\mu}_c$ are constants. Hence, the equations of motion corresponding to (2.5.3) become

$$\frac{db}{dT} = \{b, H_{\text{eff}}\} = -\frac{1}{2}\left[\frac{\sin(\mathring{\mu}_b b)}{\mathring{\mu}_b} + \gamma^2\frac{\mathring{\mu}_b}{\sin(\mathring{\mu}_b b)}\right], \tag{2.5.4}$$

$$\frac{dp_b}{dT} = \{p_b, H_{\text{eff}}\} = \frac{1}{2}p_b\cos(\mathring{\mu}_b b)\left[1 - \gamma^2\frac{\mathring{\mu}_b^2}{\sin^2(\mathring{\mu}_b b)}\right], \tag{2.5.5}$$

$$\frac{dc}{dT} = \{c, H_{\text{eff}}\} = -2\frac{\sin(\mathring{\mu}_c c)}{\mathring{\mu}_c}, \tag{2.5.6}$$

$$\frac{dp_c}{dT} = \{p_c, H_{\text{eff}}\} = 2p_c\cos(\mathring{\mu}_c c). \tag{2.5.7}$$

Notice that the $\mathring{\mu}_b \to 0$ and $\mathring{\mu}_c \to 0$ limit of these equations corresponds to the classical equations of motion (2.3.7)–(2.3.10). The solutions to these equations in terms of the

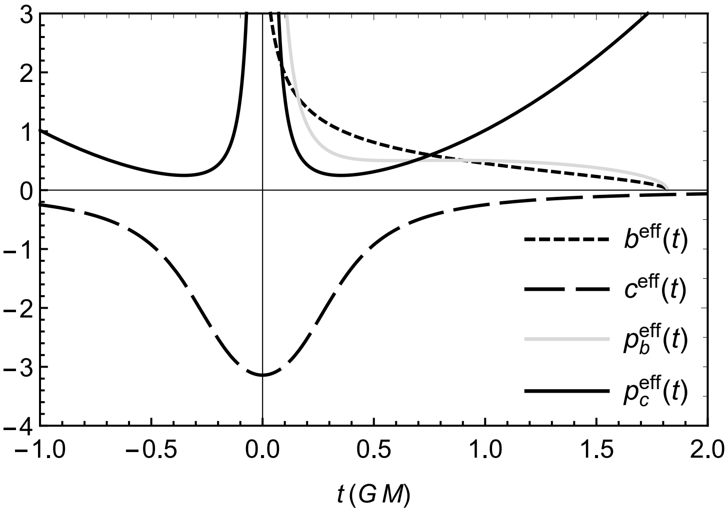

Figure 3: The behavior of canonical variables as a function of Schwarzschild time t, with the positive sign for b and negative sign for c. Plotted with $\gamma = 0.5$, $M = 1$, $G = 1$, $L_0 = 1$, $\mathring{\mu}_b = 0.5$, and $\mathring{\mu}_c = 0.5$. The bounce in p_b, p_c, and c indicates singularity resolution.

Schwarzschild time t with suitable initial conditions, are given by

$$b(t) = \frac{\cos^{-1}\left[\sqrt{1+\gamma^2\mathring{\mu}_b^2}\tanh\left(\sqrt{1+\gamma^2\mathring{\mu}_b^2}\ln\left[\frac{2\sqrt{\frac{t}{2M}}}{\gamma\mathring{\mu}_b}\right]\right)\right]}{\mathring{\mu}_b}, \tag{2.5.8}$$

$$p_b(t) = \frac{\gamma\mathring{\mu}_b L_0 M\left(\frac{\gamma^2\mathring{\mu}_c^2 L_0^2 M^2}{4t^2}+t^2\right)\sqrt{1-(1+\gamma^2\mathring{\mu}_b^2)\tanh^2\left(\sqrt{\gamma^2\mathring{\mu}_b^2+1}\ln\left[\frac{2\sqrt{\frac{t}{2M}}}{\gamma\mathring{\mu}_b}\right]\right)}}{t^2\sqrt{\frac{\gamma^2\mathring{\mu}_c^2 L_0^2 M^2}{4t^4}+1}\left(\gamma^2\mathring{\mu}_b^2-(1+\gamma^2\mathring{\mu}_b^2)\tanh^2\left(\sqrt{1+\gamma^2\mathring{\mu}_b^2}\ln\left[\frac{2\sqrt{\frac{t}{2M}}}{\gamma\mathring{\mu}_b}\right]\right)+1\right)}, \tag{2.5.9}$$

$$c(t) = -\frac{\tan^{-1}\left(\frac{\gamma\mathring{\mu}_c L_0 M}{2t^2}\right)}{\mathring{\mu}_c}, \tag{2.5.10}$$

$$p_c(t) = \frac{\gamma^2\mathring{\mu}_c^2 L_0^2 M^2}{4t^2} + t^2. \tag{2.5.11}$$

The behavior of these solutions is plotted in Fig. (3). It is seen that both p_b and p_c now exhibit a bounce in this effective regime. The bounce implies there is a minimum radius at the bounce due to the existence of a minimum value for p_c. This leads to the resolution of the classical singularity which can also be seen from the fact that the Riemann invariants, which are proportional to $\frac{1}{p_c^n}$ with $n > 0$, do not diverge anywhere inside the black hole.

Replacing the effective solutions (2.5.5) and (2.5.7) into (2.4.2) and (2.4.3) and using

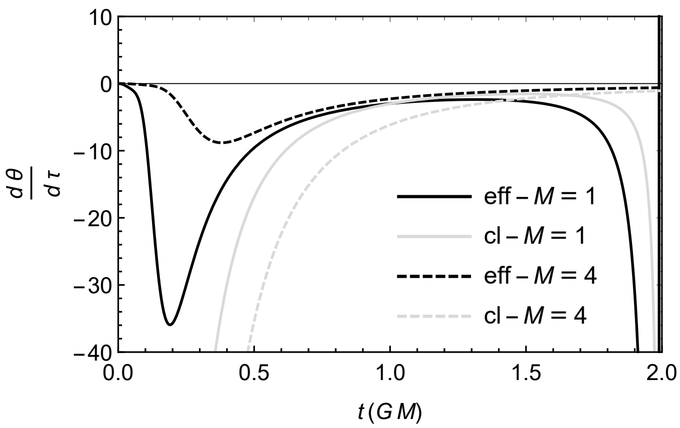

Figure 4: Plot of $\frac{d\theta}{d\tau}$ as a function of the Schwarzschild time t, for two different masses in classical vs effective regimes. The figure is plotted using $\gamma = 0.5$, $G = 1$, $L_0 = 1$, and $\mathring{\mu}_b = 0.08 = \mathring{\mu}_c$.

them in the expression of the Raychaudhuri equation (2.4.1), one obtains

$$\begin{aligned}\frac{d\theta}{d\tau} =& \frac{1}{\gamma^2 p_c}\frac{\sin^2(\mathring{\mu}_b b)}{\mathring{\mu}_b^2}\left[\cos(\mathring{\mu}_b b)\cos(\mathring{\mu}_c c) - \frac{\cos^2(\mathring{\mu}_b b)}{4} - 3\cos^2(\mathring{\mu}_c c)\right] \\ &+ \frac{\cos(\mathring{\mu}_b b)}{p_c}\left[\frac{\cos(\mathring{\mu}_b b)}{2} - \cos(\mathring{\mu}_c c) - \frac{\gamma^2}{4}\cos(\mathring{\mu}_b b)\frac{\mathring{\mu}_b^2}{\sin^2(\mathring{\mu}_b b)}\right]. \end{aligned} \tag{2.5.12}$$

It is instructive to first look at the expansion up to the second order in $\mathring{\mu}_b$ and $\mathring{\mu}_c$,

$$\frac{d\theta}{d\tau} \approx -\frac{1}{2p_c}\left(1 + \frac{9b^2}{2\gamma^2} + \frac{\gamma^2}{2b^2}\right) + \mathring{\mu}_b^2 \frac{1}{2p_c}\left(\frac{b^4}{\gamma^2} + \frac{\gamma^2}{3}\right) + \mathring{\mu}_c^2 \frac{c^2}{2p_c}\left(1 + \frac{5b^2}{\gamma^2}\right). \tag{2.5.13}$$

One can see that the first term on the right-hand side is the classical expression (2.4.4) which is always negative and leads to the divergence of classical expansion rate at the singularity, i.e., infinite focusing. However, Eq. (2.5.13) now involves two additional effective terms proportional to $\mathring{\mu}_b^2$ and $\mathring{\mu}_c^2$, both of which are positive. Hence, the quantum corrections up to the second order in polymer parameters contribute to defocusing, which becomes particularly large close to the singularity. When the full nonperturbative expression is considered (2.5.12), written in terms of the Schwarzschild time t using the solutions (2.5.8)–(2.5.11), this behavior becomes apparent. Figure (4) includes the classical versus the effective behavior of $\frac{d\theta}{d\tau}$ for two different masses. While $\frac{d\theta}{d\tau}$ diverges at the classical singularity, signaling an infinite focusing of geodesics there for both masses, the quantum effects actually reverse this situation for the effective case. Consequently, $\frac{d\theta}{d\tau}$ bounces back from a finite negative value and goes to zero as the classical singularity region is approached. This leads to the resolution of the singularity in the effective theory. It is also worth noting that this happens earlier for a larger black hole.

The nonperturbative effective correction terms resulting from loop quantization appear to contribute to terms with a positive sign and only become significant close to the singularity where quantum gravity effects should be significant. These effective terms then take over and reverse the classical focusing behavior, driving $\frac{d\theta}{d\tau}$ to zero.

2.5.2 $\bar{\mu}$ scheme

Where previously the μ's were constant, in the $\bar{\mu}$-scheme, they now depend on the canonical variables in the following way

$$\bar{\mu}_b = \sqrt{\frac{\Delta}{p_b}}, \tag{2.5.14}$$

$$\bar{\mu}_c = \sqrt{\frac{\Delta}{p_c}}. \tag{2.5.15}$$

Here Δ is the area gap in the full theory of LQG, a fundamental physical parameter. Following the same procedure as before, the resulting equations of motion are:

$$\frac{db}{dT} = \frac{1}{4}\left(b\cos\left(\bar{\mu}_b b\right) - 3\frac{\sin\left(\bar{\mu}_b b\right)}{\bar{\mu}_b} - \gamma^2 \frac{\bar{\mu}_b}{\sin\left(\bar{\mu}_b b\right)}\left[1 + b\cos\left(\bar{\mu}_b b\right)\frac{\bar{\mu}_b}{\sin\left(\bar{\mu}_b b\right)}\right]\right), \tag{2.5.16}$$

$$\frac{dp_b}{dT} = \frac{1}{2}p_b\cos\left(\bar{\mu}_b b\right)\left[1 - \gamma^2\frac{\bar{\mu}_b^2}{\sin^2\left(\bar{\mu}_b b\right)}\right], \tag{2.5.17}$$

$$\frac{dc}{dT} = c\cos\left(\bar{\mu}_c c\right) - 3\frac{\sin\left(\bar{\mu}_c c\right)}{\bar{\mu}_c}, \tag{2.5.18}$$

$$\frac{dp_c}{dT} = 2p_c\cos\left(\bar{\mu}_c c\right). \tag{2.5.19}$$

The solutions to these equations in terms of Schwarzschild time t are obtained numerically using the same initial conditions close to the horizon as have been used in the classical case. They are plotted in Fig. (5). From Fig. (5) one can see that p_c still retains a certain minimum value and bounces after reaching this value. Hence, none of the Riemann invariants will diverge.

The full Raychaudhuri equation now becomes

$$\begin{aligned}\frac{d\theta}{d\tau} =& \frac{1}{\gamma^2 p_c}\frac{\sin^2\left(\bar{\mu}_b b\right)}{\bar{\mu}_b^2}\left[\cos\left(\bar{\mu}_b b\right)\cos\left(\bar{\mu}_c c\right) - \frac{\cos^2\left(\bar{\mu}_b b\right)}{4} - 3\cos^2\left(\bar{\mu}_c c\right)\right] \\ &+ \frac{\cos\left(\bar{\mu}_b b\right)}{p_c}\left[\frac{\cos\left(\bar{\mu}_b b\right)}{2} - \cos\left(\bar{\mu}_c c\right) - \frac{\gamma^2}{4}\cos\left(\bar{\mu}_b b\right)\frac{\bar{\mu}_b^2}{\sin^2\left(\bar{\mu}_b b\right)}\right].\end{aligned} \tag{2.5.20}$$

Looking again at just the expansion of this expression before considering the full nonper-

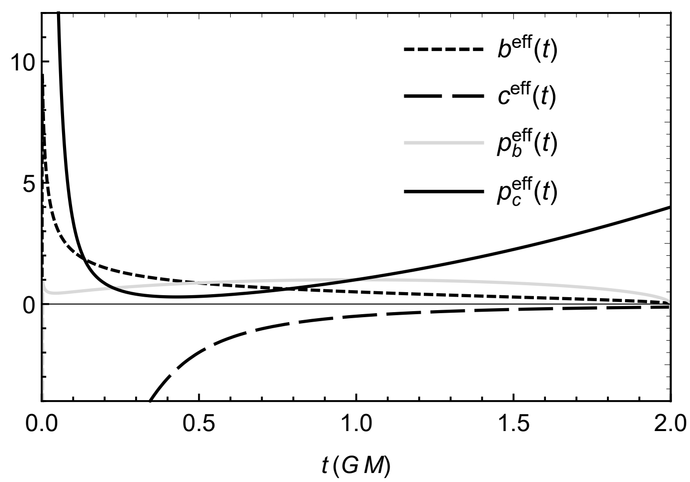

Figure 5: The behavior of canonical variables as a function of Schwarzschild time t in the $\bar{\mu}$ scheme with positive sign for b and negative sign for c . The figure is plotted using $\gamma = 0.5$, $M = 1$, $G = 1$, $L_0 = 1$, and $\Delta = 0.1$.

turbative version up to first order in Δ (which can be considered as the second order in $\bar{\mu}$ scales)

$$\frac{d\theta}{d\tau} \approx -\frac{1}{2p_c}\left(1+\frac{9b^2}{2\gamma^2}+\frac{\gamma^2}{2b^2}\right)+\frac{\Delta}{p_c}\left[\frac{1}{6p_b}\left(\frac{3b^4}{\gamma^2}+\gamma^2\right)+\frac{c^2}{2p_c}\left(1+\frac{5b^2}{\gamma^2}\right)\right]. \tag{2.5.21}$$

Once again, the first term on the right-hand side is the classical expression of the Raychaudhuri equation (2.4.4), contributing to infinite focusing at the singularity. However, all the correction terms are positive becoming significant close to the singularity contributing to defocusing. The full nonperturbative form the modified Raychaudhuri equation in terms of t is plotted in Fig. (6). As the region of the classical singularity is approached, an initial bump or bounce in encountered, followed by a more pronounced bounce closer to where the singularity used to be. As one may begin to expect, the quantum corrections become dominant close to the singularity and turn back the $\frac{d\theta}{d\tau}$ such that at $t \to 0$ no focusing happens at all.

2.5.3 $\bar{\mu}'$ scheme

Here $\bar{\mu}'_b$, $\bar{\mu}'_c$ have the following dependence on the triad variables p_b and p_c as follows:

$$\bar{\mu}'_b = \sqrt{\frac{\Delta}{p_c}}, \tag{2.5.22}$$

$$\bar{\mu}'_c = \frac{\sqrt{p_c \Delta}}{p_b}. \tag{2.5.23}$$

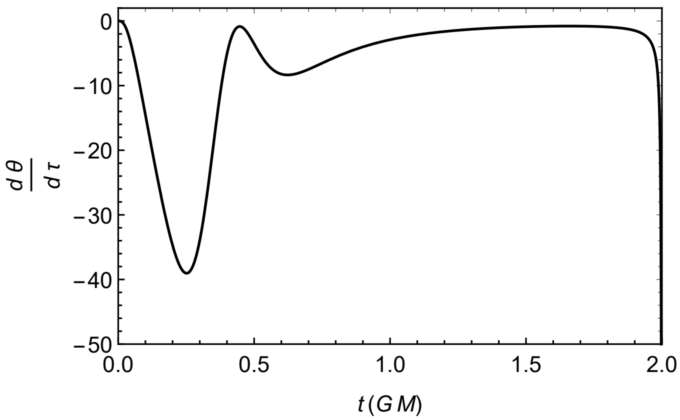

Figure 6: Plot of $\frac{d\theta}{d\tau}$ as a function of the Schwarzschild time t in the $\bar{\mu}$ scheme. The figure is plotted using $\gamma = 0.5$, $G = 1$, $L_0 = 1$

The equations of motion in this case are

$$\frac{db}{dT} = -\frac{1}{2}\gamma^2 \frac{\bar{\mu}_b'}{\sin(\bar{\mu}_b' b)} - \frac{1}{2}\frac{\sin(\bar{\mu}_b' b)}{\bar{\mu}_b'} - \frac{p_c}{p_b}\left[\frac{\sin(\bar{\mu}_c' c)}{\bar{\mu}_c'} + c\cos(\bar{\mu}_c' c)\right], \tag{2.5.24}$$

$$\frac{dp_b}{dT} = \frac{1}{2} p_b \cos(\bar{\mu}_b' b)\left[1 - \gamma^2 \frac{\bar{\mu}_b'^2}{\sin^2(\bar{\mu}_b' b)}\right], \tag{2.5.25}$$

$$\begin{aligned}\frac{dc}{dT} =& \frac{p_b}{2p_c}\left[\gamma^2 \frac{\bar{\mu}_b'}{\sin(\bar{\mu}_b' b)}\left[1 - \frac{\bar{\mu}_b'}{\sin(\bar{\mu}_b' b)} b\cos(\bar{\mu}_b' b)\right] - \frac{\sin(\bar{\mu}_b' b)}{\bar{\mu}_b'}\right] \\ &+ \frac{b p_b \cos(\bar{\mu}_b' b)}{2p_c} - \frac{\sin(\bar{\mu}_c' c)}{\bar{\mu}_c'} - c\cos(\bar{\mu}_c' c),\end{aligned} \tag{2.5.26}$$

$$\frac{dp_c}{dT} = 2p_c \cos(\bar{\mu}_c' c). \tag{2.5.27}$$

Under this dependence, the behavior is quite different than the previous two schemes, but nonetheless the singularity is still avoided. It's interesting to note that the solutions of both b and p_c exhibit a sort of damped oscillatory behavior close to the classical singularity which will contribute to a more volatile behavior of the Raychaudhuri equation. The full Raychaudhuri equation in this case takes the following form

$$\begin{aligned}\frac{d\theta}{d\tau} =& \frac{1}{\gamma^2 p_c}\frac{\sin^2(b\bar{\mu}_b')}{\bar{\mu}_b'^2}\left[\cos(\bar{\mu}_b' b)\cos(\bar{\mu}_c' c) - \frac{\cos^2(\bar{\mu}_b' b)}{4} - 3\cos^2(\bar{\mu}_c' c)\right] \\ &+ \frac{\cos(\bar{\mu}_b' b)}{p_c}\left[\frac{\cos(\bar{\mu}_b' b)}{2} - \cos(\bar{\mu}_c' c) - \frac{\gamma^2}{4}\cos(\bar{\mu}_b' b)\frac{\bar{\mu}_b'^2}{\sin^2(\bar{\mu}_b' b)}\right].\end{aligned} \tag{2.5.28}$$

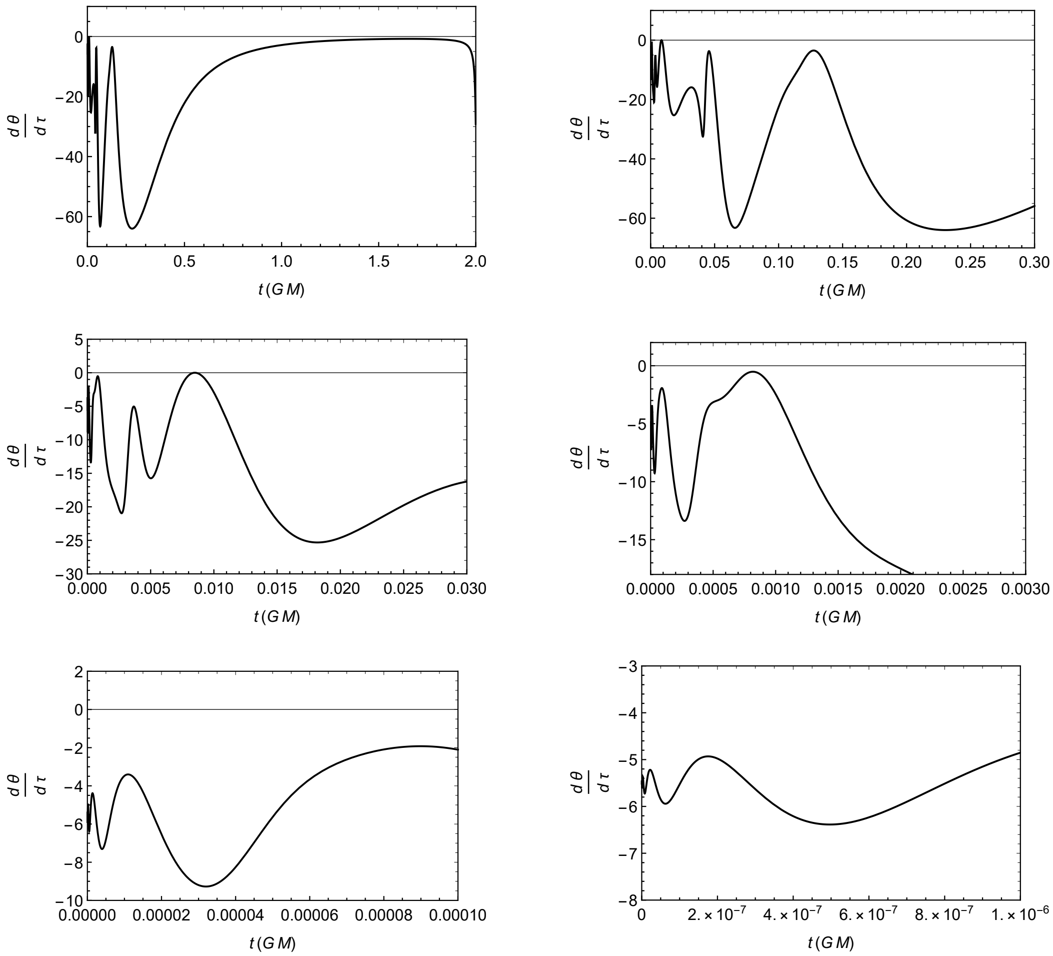

Figure 7: Raychaudhuri equation in the $\bar{\mu}'$ scheme. The top left figure shows the behavior over the whole $0 \leq t \leq 2GM$ range. Other plots show various close-ups of that plot over smaller ranges of t. The figure is plotted using $\gamma = 0.5$, $M = 1$, $G = 1$, $L_0 = 1$, and $\Delta = 0.1$.

This again looks identical to (2.5.12) and (2.5.20), except for the different forms of $\bar{\mu}'$. The expansion of the above equation to firs order in Δ is given by

$$\frac{d\theta}{d\tau} \approx -\frac{1}{2p_c}\left(1 + \frac{9b^2}{2\gamma^2} + \frac{\gamma^2}{2b^2}\right) + \frac{\Delta}{6\gamma^2}\left[\frac{1}{p_c^2}\left(3b^4 + \gamma^4\right) + \frac{3c^2}{p_b^2}\left(5b^2 + \gamma^2\right)\right]. \tag{2.5.29}$$

The form is different from the previous two results but nevertheless it still exhibits the property that the quantum corrections are all positive and hence once again contribute to defocusing of the geodesics. The full nonperturbative Raychaudhuri equation and its close-ups in this case are plotted in Fig. (7). It is seen that in this scheme, the Raychaudhuri equation exhibits a more volatile behavior and has various bumps particularly when approaching where the singularity used to be. Very close to the classical singularity, its form resembles those of b and p_c, behaving like a damped oscillation. Unlike the previous schemes, this scheme yields a nonvanishing value for $\frac{d\theta}{d\tau}$ at or very close to the singularity. In Fig. (7) with the particular choice of numerical values of γ, M, G, L_0 and Δ, the value of $\frac{d\theta}{d\tau}$ for $t \to 0$ is approximately -5.5. Hence, although a nonvanishing focusing is not achieved where the singularity used to be it is still only a relatively small focusing.

2.6 Concluding remarks on black hole singularity resolution via the modified Raychaudhuri equation in LQG

This work investigates LQG corrections arising from applying LQC-inspired polymer quantization techniques to the interior of the Schwarzschild black hole.By exploiting the Kantowski-Sachs symmetry of the Schwarzschild interior, the metric is expressed using Ashtekar-Barbero variables adapted to this symmetry. The dynamics are derived from the classical and effective Hamiltonian constraints, yielding expressions for the Raychaudhuri equation in both classical and quantum regimes. Following standard practice in LQC for Kantowski-Sachs models, various schemes are explored to determine the appropriate choice of the polymer scales, denoted μ_b and μ_c. In all schemes investigated, loop quantum corrections introduce additional terms in the Raychaudhuri equation. Importantly, These terms are positive (repulsive) near the classical singularity, in contrast to the negative (attractive) terms in the classical Raychaudhuri equation. While the classical terms promote geodesic convergence, the quantum terms derived in this work are sufficient to prevent it. This violates the geodesic focusing condition of the Hawking-Penrose singularity theorems, rendering them inapplicable and resolving the classical singularity by ensuring geodesic completeness. It should be emphasized that this result is true only for the spherically symmetric Schwarzschild black hole, more work is necessary to apply these methods to realistic astrophysical black holes as well, with little or no symmetries.

3 Generalized Uncertainty-Inspired Black Hole

Various quantum gravity approaches predict a minimum measurable length scale, with some also suggesting a maximum measurable angular momentum. One such approach is the Generalized Uncertainty Principle (GUP), sometimes referred to as the minimal uncertainty approach [96, 97]. In contrast to LQG, which quantizes spacetime geometry using holonomies and fluxes, GUP modifies the Heisenberg uncertainty principle. It is based on the idea that the fundamental commutation relations between position and momentum operators may be deformed at small scales, leading to a modification of the standard uncertainty relations. By introducing a nonzero minimal uncertainty in position or momentum, GUP alters the underlying algebra, leading to corrections in the standard Heisenberg commutation relations. These modifications yield corrections to the Hamiltonian dynamics, introducing quantum gravity effects at small scales. While this work employs the Ashtekar–Barbero variables to explore GUP effects in a gravitational context, it is worth noting that GUP-inspired modifications have also been applied in simpler settings using other canonical variables, such as ADM metric variables or standard phase space pairs (q, p) in quantum mechanics and minisuperspace cosmology [98, 99]. Given that the GUP modifies the fundamental Poisson brackets, the standard notion of canonical conjugacy breaks down: the position and momentum variables no longer satisfy $\{q, p\} = 1$, but rather a deformation such as $\{q, p\} = 1 + \beta p^2$. In this setting, one can sometimes define effective conjugate variables that restore canonical structure, though these are typically nonlinear functions of the original variables [96, 100]. A general theory of canonical transformations adapted to GUP-deformed algebras remains under development, though attempts have been made to formulate a consistent Hamiltonian framework within which such transformations can be understood [97, 101]. These structural questions underscore the importance of choosing a variable set that remains mathematically manageable and physically interpretable in the presence of GUP corrections.

GUP has been applied to the Schwarzschild black hole interior using Ashtekar-Barbero variables in both the effective regime [101, 102], with comparisons to LQG [103], and the quantum regime [90]. However, directly applying it to the full spacetime of a black hole is still not well understood. To the author's knowledge, no systematic derivation of a full GUP-corrected metric exists in the literature—namely, one that is not limited to perturbative expansions in GUP parameters or based solely on heuristic arguments. The present work aims to fill this gap. The work presented here employs techniques from LQG to find the full spacetime metric of a GUP-modified Schwarzschild black hole. This approach begins by analyzing the Schwarzschild interior metric in Ashtekar-Barbero (AB) variables, as discussed in the previous chapter, but with a GUP-modified algebra. The resulting interior metric is then extended to the full spacetime. This is similar to the approach used in some of the proposed models in LQG [50, 71, 104]. However, the resulting metric exhibits asymptotic deviations, similar to those encountered in [104]. This work remedies these issues by borrowing from LQG the ideas introduced in Chapter 2, in which the quantum parameters of the model that are originally constant become momentum-dependent in different "schemes". Remarkably, this prescription not only resolves the asymptotic issues but renders the black hole regular.

3.1 Non-improved effective interior metric

The Schwarzschild black hole interior, expressed in Ashtekar-Barbero (AB) variables, was introduced in Section 2.2, Eq. (2.2.10). Next, recall the classical Poisson brackets for the phase space variables, given in Eq. (2.3.4) and repeated here for convenience:

$$\{b, p_b\} = G\gamma \quad \text{and} \quad \{c, p_c\} = 2G\gamma. \tag{3.1.1}$$

As demonstrated in Section 2.4, the classical singularity persists in this framework, as evidenced by the divergence of the Kretschmann scalar in Eq. (2.3.30).

To implement GUP, the Poisson brackets in Eq. (3.1.1) are modified with quadratic terms in the connection variables:

$$\{b, p_b\} = G\gamma \left(1 + \beta_b b^2\right), \tag{3.1.2}$$

$$\{c, p_c\} = 2G\gamma \left(1 + \beta_c c^2\right), \tag{3.1.3}$$

where β_b and β_c are small dimensionless GUP parameters [96, 97]. In general, the uncertainty in a phase space variable q and its conjugate momentum p is governed by the expectation value of their commutator

$$\Delta q \Delta p \geq \frac{1}{2} |\langle [\hat{q}, \hat{p}] \rangle|, \tag{3.1.4}$$

where $\langle \hat{O} \rangle$ denotes the expectation value of the operator $\hat{O}$, and ΔA is the standard deviation (uncertainty) in measurements of the observable A. (Note the Δ here refers to uncertainty, not the area gap of LQG introduced in Chapter 2).

If the commutation relation is modified as

$$[\hat{q}, \hat{p}] = i\hbar \left(1 + \beta \left\langle q^2 \right\rangle + \alpha \left\langle p^2 \right\rangle\right) \tag{3.1.5}$$

then the uncertainty principle becomes [96, 97]

$$\Delta q \Delta p \geq \frac{\hbar}{2} \left[1 + \beta (\Delta q)^2 + \alpha (\Delta p)^2 + \beta \left\langle q \right\rangle^2 + \alpha \left\langle p \right\rangle^2\right]. \tag{3.1.6}$$

This implies the existence of a minimal uncertainty in both q and p, given that $\alpha > 0$ and $\beta > 0$ [96, 97]. Applying the modified Poisson brackets (3.1.2)–(3.1.3) to the gravitational phase space variables b, p_b, c, and p_c yields:

$$\Delta p_b \geq G\gamma(\frac{1}{\Delta b} + \beta_b \Delta b), \tag{3.1.7}$$

and

$$\Delta p_c \geq 2G\gamma(\frac{1}{\Delta c} + \beta_c \Delta c) \tag{3.1.8}$$

These expressions confirm minimal uncertainties in Δp_b and Δp_c, with minimal scales of order $\sqrt{\beta_b}$ and $\sqrt{\beta_c}$, respectively [101]. Since the momenta p_b and p_c correspond to components of the densitized triad (see (2.2.6)), and ultimately the metric (2.2.10), this modification implies a fundamental minimal scale in the geometry itself. However, this approach encounters several issues when restricted to positive deformation parameters β, to be discussed later. If one extends this method, particularly (3.1.5), to negative values of GUP parameters, one will not obtain a minimal uncertainty anymore, but the issues will be resolved. The negativity of deformation parameters hints that the physical spacetime has actually a lattice or granular structure at the Planck scale, essentially a crystal-like universe whose lattice spacing is of the order of Planck length [105].

Although (3.1.2) and (3.1.3) do not modify the Hamiltonian (2.3.6), they lead to effective equations of motion that are different from the classical ones (2.3.7)-(2.3.10) due to the modification of the Poisson algebra. Using the classical Poisson brackets (3.1.1), and the equations of motion

$$\begin{aligned} \dot{b} &= \{b, H\}_{\text{cl}} & \dot{p_b} &= \{p_b, H\}_{\text{cl}} \\ \dot{c} &= \{c, H\}_{\text{cl}} & \dot{p_c} &= \{p_c, H\}_{\text{cl}}, \end{aligned}$$

the modifications of (3.1.2)-(3.1.3) result in the classical equations of motion becoming the effective equations of motion

$$\dot{b} = \{b, H\}_{\text{eff}} = \{b, H\}_{\text{cl}}(1 + \beta_b b^2) \qquad \dot{p_b} = \{p_b, H\}_{\text{eff}} = \{p_b, H\}_{\text{cl}}(1 + \beta_b b^2) \tag{3.1.9}$$

$$\dot{c} = \{c, H\}_{\text{eff}} = \{c, H\}_{\text{cl}}(1 + \beta_c c^2) \qquad \dot{p_c} = \{p_c, H\}_{\text{eff}} = \{p_c, H\}_{\text{cl}}(1 + \beta_c c^2). \tag{3.1.10}$$

Recalling (2.3.10), the effective equations of motion become

$$\dot{b} =-\frac{b^2+\gamma^2}{2b}\left(1+\beta_b b^2\right), \tag{3.1.11}$$

$$\dot{p}_b =\frac{p_b\left(b^2-\gamma^2\right)}{2b^2}\left(1+\beta_b b^2\right), \tag{3.1.12}$$

$$\dot{c} =-2c\left(1+\beta_c c^2\right), \tag{3.1.13}$$

$$\dot{p}_c =2p_c\left(1+\beta_c c^2\right). \tag{3.1.14}$$

With solutions [101–103]

$$b =\frac{\gamma\sqrt{R_s t^{\beta_b\gamma^2}-t\left(\gamma^2 R_s\right)^{\beta_b\gamma^2}}}{\sqrt{t\left(\gamma^2 R_s\right)^{\beta_b\gamma^2}-\beta_b\gamma^2 R_s t^{\beta_b\gamma^2}}}, \tag{3.1.15}$$

$$p_b =\gamma L_0 t^{-\beta_b\gamma^2}\sqrt{R_s t^{\beta_b\gamma^2}-t\left(\gamma^2 R_s\right)^{\beta_b\gamma^2}}\sqrt{t\left(\gamma^2 R_s\right)^{\beta_b\gamma^2}-\beta_b\gamma^2 R_s t^{\beta_b\gamma^2}}, \tag{3.1.16}$$

$$c =-\frac{\gamma L_0 R_s}{2\sqrt{t^4-\frac{1}{4}\beta_c\gamma^2 L_0^2 R_s^2}}, \tag{3.1.17}$$

$$p_c =\sqrt{t^4-\frac{1}{4}\beta_c\gamma^2 L_0^2 R_s^2}. \tag{3.1.18}$$

The constants of integration in these solutions have been fixed by matching the classical limit of these solutions when $\beta_b \to 0$ and $\beta_c \to 0$, with the actual classical solutions (2.3.26)-(2.3.29). Substituting the solutions into the metric (2.2.10) together with (2.3.5) written in t yields the effective interior metric for the modified algebra

$$ds^2=-\frac{1}{t^2}\frac{\gamma^2 p_c(t)}{b^2(t)}dt^2+\frac{p_b^2(t)}{L_0^2 p_c(t)}dr^2+p_c(t)\left(d\theta^2+\sin^2(\theta)\,d\phi^2\right). \tag{3.1.19}$$

3.2 Full spacetime extension of the non-improved metric

As explained in Section 2.2, the extended (interior and exterior) metric of the classical Schwarzschild spacetime can be derived by switching the timelike and spacelike coordinates of the Schwarzschild interior. As a first attempt to obtain the extended metric of the GUP modified metric, the same concept is applied to the interior metric found above. In other words, take $t \to r$ and $r \to t$ in the solutions (3.1.15)-(3.1.18) and in the metric (3.1.19)

$$ds^2=\frac{\check{p}_b^2(r)}{L_0^2\check{p}_c(r)}dt^2-\frac{1}{r^2}\frac{\gamma^2\check{p}_c(r)}{\check{b}^2(r)}dr^2+\check{p}_c(r)\left(d\theta^2+\sin^2(\theta)\,d\phi^2\right), \tag{3.2.1}$$

where the checks denote the extended canonical variables. From here on, both interior and exterior will be described by coordinates (t, r, θ, ϕ), with t and r timelike and spacelike in the exterior, respectively, and spacelike and timelike in the interior, respectively.

The next step is to write the canonical variables (3.1.15)-(3.1.18) in a more concise form to further investigate the metric components in the extended spacetime. It is convenient to introduce the following quantities

$$\check{Q}_b = |\beta_b| \gamma^2, \tag{3.2.2}$$
$$\check{Q}_c = |\beta_c| \gamma^2, \tag{3.2.3}$$

and

$$\begin{aligned}
\check{\lambda}(r) &= r\left(\gamma^2 R_s\right)^{\operatorname{sgn}(\beta_b)\check{Q}_b} - R_s r^{\operatorname{sgn}(\beta_b)\check{Q}_b}, && (3.2.4)\\
\check{\mu}(r) &= r\left(\gamma^2 R_s\right)^{\operatorname{sgn}(\beta_b)\check{Q}_b} - \operatorname{sgn}(\beta_b)\,\check{Q}_b R_s r^{\operatorname{sgn}(\beta_b)\check{Q}_b}, && (3.2.5)\\
\check{\xi}(r) &= 4r^4 - L_0^2 \operatorname{sgn}(\beta_c)\,\check{Q}_c R_s^2. && (3.2.6)
\end{aligned}$$

Then the canonical variables can be expressed as

$$\begin{aligned}
\check{b}(r) &= \gamma\sqrt{-\frac{\check{\lambda}(r)}{\check{\mu}(r)}}, && (3.2.7)\\
\check{p}_b(r) &= \frac{L_0}{r^{\operatorname{sgn}(\beta_b)\check{Q}_b}}\sqrt{-\check{\lambda}(r)\,\check{\mu}(r)}, && (3.2.8)\\
\check{c}(r) &= -\frac{\gamma L_0 R_s}{\sqrt{\check{\xi}(r)}}, && (3.2.9)\\
\check{p}_c(r) &= \frac{1}{2}\sqrt{\check{\xi}(r)}. && (3.2.10)
\end{aligned}$$

Substituting these expressions into the extended metric components (3.2.1) yields the metric components

$$\begin{aligned}
\check{g}_{00} &= \frac{\check{p}_b^2}{L_0^2 \check{p}_c} = -\frac{2}{r^{2\operatorname{sgn}(\beta_b)\check{Q}_b}}\frac{\check{\lambda}(r)\,\check{\mu}(r)}{\sqrt{\check{\xi}(r)}}, && (3.2.11)\\
\check{g}_{11} &= -\frac{\gamma^2 \check{p}_c}{\check{b}^2 r^2} = \frac{1}{2r^2}\sqrt{\check{\xi}(r)}\frac{\check{\mu}(r)}{\check{\lambda}(r)}, && (3.2.12)\\
\check{g}_{22} &= \frac{\check{g}_{33}}{\sin^2(\theta)} = \frac{1}{2}\sqrt{\check{\xi}(r)}. && (3.2.13)
\end{aligned}$$

In order for the metric to have the correct signature $(-+++)$, $\check{\lambda}$ and $\check{\mu}$ must have the same sign. For this to be the case, $\check{b}$ and $\check{p}_b$ must be imaginary in the exterior which is similar to some approaches in LQG [106].

3.3 Issues with the non-improved extended metric

The full spacetime metric, with components given by Equations (3.2.11)–(3.2.13), must recover the classical Schwarzschild solution and exhibit proper asymptotic behavior. Analysis shows that the classical limits correctly recover the Schwarzschild metric:

$$\lim_{\beta_b,\,\beta_c\to 0} \check{g}_{00} = -\left(1-\frac{R_s}{r}\right), \tag{3.3.1}$$

$$\lim_{\beta_b,\,\beta_c\to 0} \check{g}_{11} = \left(1-\frac{R_s}{r}\right)^{-1}, \tag{3.3.2}$$

$$\lim_{\beta_b,\,\beta_c\to 0} \check{g}_{22} = r^2. \tag{3.3.3}$$

However, the asymptotic limits fail to recover a Minkowski spacetime:

$$\lim_{r\to\infty} \check{g}_{00} = \begin{cases} 0, & \operatorname{sgn}(\beta_b) = 1 \\ -\infty, & \operatorname{sgn}(\beta_b) = -1 \end{cases}, \tag{3.3.4}$$

$$\lim_{r\to\infty} \check{g}_{11} = \begin{cases} \check{Q}_b, & \operatorname{sgn}(\beta_b) = 1 \\ 1, & \operatorname{sgn}(\beta_b) = -1 \end{cases}. \tag{3.3.5}$$

Further more, the Kretschmann scalar exhibits an incorrect asymptotic fall-off of $K \propto r^{-4}$, compared to the classical r^{-6} behavior. As discussed in Section 2.5, LQG addresses similar asymptotic issues by using momentum-dependent quantum parameters, such as in the $\bar{\mu}$ and $\bar{\mu}'$ improved schemes. It proves instructive to borrow these ideas from LQG and apply them to the GUP parameters.

3.4 Improved effective metric in the $\bar{\beta}$ scheme

3.4.1 Improved metric and its extension to the full spacetime

Adopting LQG's momentum-dependent parameter approach, one can modify the dimensionless quantum parameters to:

$$\beta_b \to \bar{\beta}_b = \frac{\beta_b L_0^4}{p_b^2}, \tag{3.4.1}$$

$$\beta_c \to \bar{\beta}_c = \frac{\beta_c L_0^4}{p_c^2}, \tag{3.4.2}$$

where the powers of L_0 are included to render the $\bar{\beta}$'s dimensionless. This prescription will be referred to as the $\bar{\beta}$ improved scheme, reminiscent of the $\bar{\mu}$ scheme introduced in 2.5.2. The modified GUP algebra becomes:

$$\{b, p_b\} = G\gamma\left(1+\bar{\beta}_b b^2\right) = G\gamma\left(1+\frac{\beta_b L_0^4}{p_b^2}b^2\right), \tag{3.4.3}$$

$$\{c, p_c\} = 2G\gamma\left(1+\bar{\beta}_c c^2\right) = 2G\gamma\left(1+\frac{\beta_c L_0^4}{p_c^2}c^2\right). \tag{3.4.4}$$

The modified algebra alters the interior equations of motion, requiring their re-derivation, while the Hamiltonian (2.3.6) remains unchanged. The improved equations are:

$$\dot{b} = -\frac{b^2+\gamma^2}{2b}\left(1+\frac{\beta_b L_0^4}{p_b^2}b^2\right), \tag{3.4.5}$$

$$\dot{p}_b = \frac{p_b\left(b^2-\gamma^2\right)}{2b^2}\left(1+\frac{\beta_b L_0^4}{p_b^2}b^2\right), \tag{3.4.6}$$

$$\dot{c} = -2c\left(1+\frac{\beta_c L_0^4}{p_c^2}c^2\right), \tag{3.4.7}$$

$$\dot{p}_c = 2p_c\left(1+\frac{\beta_c L_0^4}{p_c^2}c^2\right). \tag{3.4.8}$$

Matching the classical limits, $\beta_b \to 0$ and $\beta_c \to 0$, of the canonical variables with the actual classical solutions (2.3.26)-(2.3.29) of the interior, results in

$$b = \gamma\sqrt{\frac{-\left(\tilde{t}^2-\operatorname{sgn}\left(\beta_b\right)Q_b\right)+R_s\sqrt{\tilde{t}^2-\operatorname{sgn}\left(\beta_b\right)Q_b}}{\tilde{t}^2-\operatorname{sgn}\left(\beta_b\right)Q_b}}, \tag{3.4.9}$$

$$p_b = L_0\sqrt{\tilde{t}^2-\operatorname{sgn}\left(\beta_b\right)Q_b}\sqrt{\frac{-\left(\tilde{t}^2-\operatorname{sgn}\left(\beta_b\right)Q_b\right)+R_s\sqrt{\tilde{t}^2-\operatorname{sgn}\left(\beta_b\right)Q_b}}{\tilde{t}^2-\operatorname{sgn}\left(\beta_b\right)Q_b}}, \tag{3.4.10}$$

$$c = -\frac{\gamma L_0 R_s}{2\left(\tilde{t}^8-\frac{1}{4}\operatorname{sgn}\left(\beta_c\right)Q_c R_s^2\right)^{\frac{1}{4}}}, \tag{3.4.11}$$

$$p_c = \left(\tilde{t}^8-\frac{1}{4}\operatorname{sgn}\left(\beta_c\right)Q_c R_s^2\right)^{\frac{1}{4}}. \tag{3.4.12}$$

where the tilde notation indicates interior coordinates, and for conciseness

$$Q_b = \left|\beta_b\right|\gamma^2 L_0^2 \quad \text{and} \quad Q_c = \left|\beta_c\right|\gamma^2 L_0^6, \tag{3.4.13}$$

where Q_b has dimensions of $[\mathrm{L}]^2$ and Q_c has dimensions of $[\mathrm{L}]^6$. Once again, it is postulated that, just as in the standard classical Schwarzschild case, the full spacetime metric of this

GUP-inspired black hole is derived by analytical extension of the interior by switching $\tilde{t} \to r$, $\tilde{r} \to t$, $\tilde{\theta} \to \theta$ and $\tilde{\phi} \to \phi$, where t and r are the usual Schwarzschild coordinates. The extended version of the canonical variables (3.4.9)-(3.4.12) are

$$\check{b} = \gamma\sqrt{\frac{R_s}{\sqrt{\nu}} - 1}, \tag{3.4.14}$$

$$\check{p}_b = L_0\sqrt{\nu}\sqrt{\frac{R_s}{\sqrt{\nu}} - 1}, \tag{3.4.15}$$

$$\check{c} = -\frac{\gamma L_0 R_s}{2\rho^{\frac{1}{4}}}, \tag{3.4.16}$$

$$\check{p}_c = \rho^{\frac{1}{4}}. \tag{3.4.17}$$

again, the checks represent the extended canonical variables with

$$\nu = r^2 - \operatorname{sgn}(\beta_b)\, Q_b \quad \text{and} \quad \rho = r^8 - \frac{1}{4}\operatorname{sgn}(\beta_c)\, Q_c R_s^2. \tag{3.4.18}$$

Replacing the solutions (3.4.14)-(3.4.17) into the improved full spacetime metric (3.2.1) gives the full spacetime metric components

$$\check{g}_{00} = \frac{\check{p}_b^2}{L_0^2\check{p}_c} = -\sqrt{\frac{\nu}{\sqrt{\rho}}}\left(\sqrt{\nu} - R_s\right), \tag{3.4.19}$$

$$\check{g}_{11} = -\frac{\gamma^2\check{p}_c}{\check{b}^2 r^2} = \frac{\sqrt{\nu\sqrt{\rho}}}{r^2\left(\sqrt{\nu} - R_s\right)}, \tag{3.4.20}$$

$$\check{g}_{22} = \frac{\check{g}_{33}}{\sin^2(\theta)} = \rho^{\frac{1}{4}}. \tag{3.4.21}$$

At this point it is a good idea to examine the signature and the conditions on reality of the above metric. To have a metric which remains real for all values of coordinates, particularly for all values of $r \in (0, \infty)$ both ν and ρ must always remain non-negative. As a result, from (3.4.18) and (3.4.13),

$$\nu > 0 \Rightarrow \operatorname{sgn}(\beta_b) = -1, \tag{3.4.22}$$

$$\rho > 0 \Rightarrow \operatorname{sgn}(\beta_c) = -1. \tag{3.4.23}$$

This is the same result that had been obtained in previous works regarding the interior of this black hole [90, 101–103]. With this requirement of signs, (3.4.13) becomes

$$Q_b = \beta_b \gamma^2 L_0^2 \,, \tag{3.4.24}$$
$$Q_c = \beta_c \gamma^2 L_0^6 \,, \tag{3.4.25}$$

and (3.4.18) becomes

$$\nu = r^2 + Q_b, \tag{3.4.26}$$
$$\rho = r^8 + \frac{1}{4} Q_c R_s^2. \tag{3.4.27}$$

This assures the metric remains real for all $r \in (0, \infty)$ and the signature is as expected for both the interior and the exterior. The final expression for the improved full spacetime metric components (3.4.19)-(3.4.21) together with (3.4.26)-(3.4.27), and (3.4.24)-(3.4.25), can be explicitly written as

$$\begin{aligned} \breve{g}_{00} &= -\sqrt{\frac{\nu}{\sqrt{\rho}}}\left(\sqrt{\nu} - R_s\right) \\ &= -\left(1 + \frac{Q_b}{r^2}\right)\left(1 + \frac{Q_c R_s^2}{4r^8}\right)^{-1/4}\left(1 - \frac{R_s}{\sqrt{r^2 + Q_b}}\right), \end{aligned} \tag{3.4.28}$$

$$\breve{g}_{11} = \frac{\sqrt{\nu\sqrt{\rho}}}{r^2\left(\sqrt{\nu} - R_s\right)} = \left(1 + \frac{Q_c R_s^2}{4r^8}\right)^{1/4}\left(1 - \frac{R_s}{\sqrt{r^2 + Q_b}}\right)^{-1}, \tag{3.4.29}$$

$$\breve{g}_{22} = \frac{\breve{g}_{33}}{\sin^2(\theta)} = \rho^{\frac{1}{4}} = r^2\left(1 + \frac{Q_c R_s^2}{4r^8}\right)^{1/4}. \tag{3.4.30}$$

The coordinates have the natural domain $r \in [0, +\infty)$, $t \in (-\infty, +\infty)$, $\theta \in [0, \pi]$ and $\phi \in [0, 2\pi]$. A plot of these metric components are presented in Fig. 8. The existence of the minimum radius of 2-spheres ($\sqrt{g_{22}}$) is related to the resolution of the singularity and it is seen that the quantum effects close to the singularity are associated to β_c as expected.

3.4.2 Classical and asymptotic limits

For the classical limit, taking $\beta_b \to 0$ and $\beta_c \to 0$ (or equivalently $Q_b \to 0$ and $Q_c \to 0$ according to (3.4.24)-(3.4.25)) of the improved metric components (3.4.28)-(3.4.30) should match those of the classical Schwarzschild metric; explicitly

$$\lim_{\beta_b, \beta_c \to 0} \breve{g}_{00} = -\left(1 - \frac{R_s}{r}\right), \qquad \lim_{\beta_b, \beta_c \to 0} \breve{g}_{11} = \left(1 - \frac{R_s}{r}\right)^{-1}, \qquad \lim_{\beta_b, \beta_c \to 0} \breve{g}_{22} = r^2. \tag{3.4.31}$$

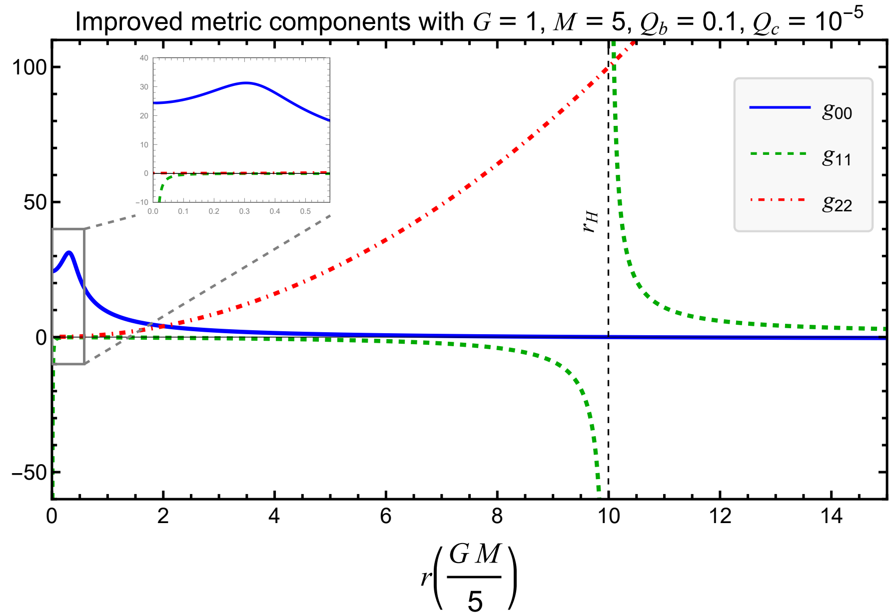

Figure 8: Plot of improved metric components in Schwarzschild coordinates with the given values of parameters on the top of the plot. Note the divergence of g_{11} at $r = 0$.

The asymptotic limits are

$$\lim_{r\to\infty} \check{g}_{00} = -1, \qquad \lim_{r\to\infty} \check{g}_{11} = 1, \qquad \lim_{r\to\infty} \check{g}_{22} = \infty. \tag{3.4.32}$$

Thus this improved prescription fixes the issues with the asymptotic limit and the asymptotic expansion of the metric pointed out above. It is also worth noting that the asymptotic expansions match the Schwarzschild spacetime to leading order:

$$\check{g}_{00}\big|_{r\to\infty} = -\left(1 - \frac{R_s}{r}\right) - \frac{Q_b}{r^2} + \mathcal{O}\left(\frac{1}{r}\right)^3, \tag{3.4.33}$$

$$\check{g}_{11}\big|_{r\to\infty} = \left(1 + \frac{R_s}{r}\right) + \frac{R_s^2}{r^2} + \frac{R_s}{2r^3}\left(2R_s^2 - Q_b\right) + \mathcal{O}\left(\frac{1}{r}\right)^4, \tag{3.4.34}$$

$$\check{g}_{22}\big|_{r\to\infty} = r^2 + \frac{Q_c R_s^2}{16 r^6} + \mathcal{O}\left(\frac{1}{r}\right)^{14}. \tag{3.4.35}$$

These characteristics will be explored further with the horizon and spacetime investigation.

3.4.3 Properties of the improved spacetime, horizon and mass

The model is static and spherically symmetric which implies that the event horizon is a Killing horizon with position given by solving $g^{11}(r_H) = 0$. This yields the horizon radius as

$$r_H = \sqrt{R_s^2 - Q_b} = R_s\sqrt{1 - \frac{Q_b}{R_s^2}}, \tag{3.4.36}$$

which is only slightly smaller than the Schwarzschild radius. This is a pure quantum effect due to the presence of Q_b, which can be seen through the expansion up to first order in Q_b of the horizon radius

$$r_H = R_s - \frac{1}{2}\frac{Q_b}{R_s} + \mathcal{O}\left(\frac{Q_b^2}{R_s^3}\right). \tag{3.4.37}$$

Given the solution for the horizon, three different spacetimes are possible depending on the relative values of M and Q_b.

Case 1:

$$M > \frac{\sqrt{Q_b}}{2G}. \tag{3.4.38}$$

There are two solutions for $g^{11} = 0$, one with a positive r and one with negative r. The positive r is the event horizon and the spacetime is that of a black hole.

Case 2

$$M = \frac{\sqrt{Q_b}}{2G}. \tag{3.4.39}$$

This is the extremal case and sets a natural limit on the minimum black hole mass. A stability analysis is needed to determine if the black hole is remnant, a stable, minimal-mass black hole.

Case 3

$$M < \frac{\sqrt{Q_b}}{2G}. \tag{3.4.40}$$

If realized, it would describe a spacetime with no event horizon and would be a one-way wormhole with an extremal null throat at $r = 0$ [107].

To confirm the physical interpretation of M, several mass definitions are computed. The Komar mass [108] is first computed from the surface integral expression [6].

$$M_{\mathrm{K}}(r) = \frac{1}{4\pi G}\int_{\partial\Sigma} d^2x\sqrt{\gamma^{(2)}}\; n_\mu \sigma_\nu \nabla^\mu K^\nu\,, \tag{3.4.41}$$

where n^μ is a unit normal timelike vector to the spacelike hypersurface Σ with constant t, and σ^μ is a unit spacelike normal vector to the 2-spheres which is the boundary of $\partial\Sigma$ at infinity, $\gamma_{ij}^{(2)}$ is the metric of that 2-sphere, and K^ν is the timelike Killing vector of the static spacetime. A unit normal vector v^μ to a hypersurface described by a function $f(x) = C$ with C a constant can be written as

$$v^\mu = \pm\sqrt{\frac{\pm 1}{g^{\alpha\beta}\partial_\alpha f \partial_\beta f}} g^{\mu\nu}\partial_\nu f \,, \tag{3.4.42}$$

where the positive signs correspond to a spatial unit vector and negative signs correspond to a timelike unit vector. With a diagonal metric, for a spacelike unit vector σ^μ normal to a surface described by $r = C_1$, one obtains

$$\sigma^\mu = \frac{g^{\mu r}}{\sqrt{g^{rr}}} \,, \tag{3.4.43}$$

while the timelike unit vector normal to a hypersurface $t = C_2$, one gets

$$n^\mu = -\frac{g^{\mu t}}{\sqrt{-g^{tt}}} \,. \tag{3.4.44}$$

Substituting these expressions, together with $K^\mu = (1,0,0,0)$ and $\sqrt{\gamma^{(2)}} = g_{\theta\theta}\sin(\theta)$ into the Komar mass M_{K} leads to

$$\begin{aligned} M_{\mathrm{K}} =& \frac{r^2}{2G}\left(\frac{1}{\sqrt{\nu}} - \frac{\omega}{\nu} + 2r^6\frac{\omega}{\rho}\right) \\ =& \frac{r^2}{2G}\left(\frac{1}{\sqrt{r^2+Q_b}} - \frac{R_s - \sqrt{r^2+Q_b}}{r^2+Q_b} + 2r^6\frac{R_s - \sqrt{r^2+Q_b}}{r^8 + \frac{1}{4}Q_c R_s^2}\right) \,, \end{aligned} \tag{3.4.45}$$

where

$$\omega = R_s - \sqrt{\nu} = R_s - \sqrt{r^2 + Q_b} \tag{3.4.46}$$

has been defined. The asymptotic expansion of M_{K} as $r \to \infty$ is

$$M_{\mathrm{K}}(r) = M - \frac{Q_b}{Gr} + \mathcal{O}\left(\frac{1}{r^2}\right) \,, \tag{3.4.47}$$

from which it follows that the asymptotic limit of the Komar mass corresponds to the parameter M appearing in the metric,

$$\lim_{r\to\infty} M_{\mathrm{K}}(r) = M. \tag{3.4.48}$$

The ADM mass [109] is computed using the expression [110]

$$M_{\mathrm{ADM}} = \lim_{r\to\infty} \bar{M}_{\mathrm{ADM}} = \lim_{r\to\infty} \frac{1}{16\pi G} \int_{\partial\Sigma} d^2x \sqrt{\gamma^{(2)}} \sigma^i \left(\bar{\eta}^{jk} \mathcal{D}_k q_{ij} - \mathcal{D}_i \left(\bar{\eta}^{jk} q_{jk} \right) \right) , \tag{3.4.49}$$

where $\mathcal{D}$ is the covariant derivative compatible with the background flat metric $\bar{\eta}^{jk}$ in spherical coordinates. The vector $\sigma^i = \bar{\eta}^{ir}/\sqrt{\bar{\eta}^{rr}} = (1, 0, 0)$ is the outward-pointing unit spacelike normal to the two-sphere $\partial\Sigma$ at infinity, which is the boundary of the spatial hypersurface Σ. The quantity q_{ij} is the induced metric on the three-dimensional spatial hypersurface Σ, while γ_{ij} is the metric of the two-sphere $\partial\Sigma$. Using these definitions, the expression for $\bar{M}_{ADM}$ is found to be

$$\begin{aligned} \bar{M}_{\mathrm{ADM}} &= \frac{\omega\left(\rho - 2r^8\right) - \sqrt{\nu}\rho}{2G\sqrt{\rho}r^3\omega} \\ &= \frac{1}{2Gr^3} \left[\frac{\frac{1}{4}Q_c R_s^2 - r^8}{\sqrt{r^8 + \frac{1}{4}Q_c R_s^2}} - \frac{\sqrt{r^2 + Q_b}\sqrt{r^8 + \frac{1}{4}Q_c R_s^2}}{R_s - \sqrt{r^2 + Q_b}} \right] . \end{aligned} \tag{3.4.50}$$

The asymptotic expansion for $r \to \infty$ takes the form

$$\bar{M}_{\mathrm{ADM}} = M + \frac{2GM^2}{r} + \frac{M\left(8G^2M^2 - Q_b\right)}{2r^2} + \mathcal{O}\left(\frac{1}{r^3}\right), \tag{3.4.51}$$

from which it follows that

$$M_{\mathrm{ADM}} = \lim_{r\to\infty} \bar{M}_{\mathrm{ADM}} = M. \tag{3.4.52}$$

Attention is then turned to the Hawking quasilocal mass, which, in spherical symmetry, reduces to the Misner–Sharp–Hernandez (MSH) mass [111, 112] given by

$$\begin{aligned} M_{\mathrm{MSH}}(r) &= \frac{r}{2G}(1 - \nabla^a r \nabla_a r) = \frac{r}{2G}\left(1 - \frac{1}{g_{11}}\right) \\ &= \frac{r}{2G}\left(1 - \left(1 - \frac{R_s}{\sqrt{r^2 + Q_b}}\right)\left(1 + \frac{Q_c R_s^2}{4r^8}\right)^{-1/4}\right) . \end{aligned} \tag{3.4.53}$$

Then, $M_{\mathrm{MSH}}(r) \to M$ as $r \to \infty$. It is thus found that the parameter M appearing in the GUP-inspired black hole metric coincides with the three mass definitions discussed above, namely

$$\lim_{r\to\infty} \bar{M}_{\mathrm{ADM}}(r) = \lim_{r\to\infty} M_{\mathrm{MSH}}(r) = \lim_{r\to\infty} M_{\mathrm{K}}(r) = M. \tag{3.4.54}$$

3.4.4 Kretschmann Scalar

It is also crucial to check that the asymptotic limit and asymptotic expansion of the Kretschmann scalar K matches those of the classical Schwarzschild spacetime. The expression for K in terms of the canonical variables is found to be

$$
\begin{aligned}
K =& \frac{4}{\sqrt{\rho}} \\
&+ \frac{4r^4}{\nu^5\rho^{\frac{9}{2}}}\Big\{\rho^4\left(\nu^{3/2}-\nu\omega\right)^2+2\nu\rho^4\omega\left(\sqrt{\nu}-\omega\right)r^2+\rho^4\omega^2r^4 \\
&+16\nu^3\rho^3\omega\left(\sqrt{\nu}-\omega\right)r^6+2\nu^2\rho^3\left(3\sqrt{\nu}\omega-2\nu+7\omega^2\right)r^8 \\
&+2\nu\rho^3\omega\left(\omega-2\sqrt{\nu}\right)r^{10}+2\nu^4\rho^2\omega\left(\sqrt{\nu}+96\omega\right)r^{12} \\
&+4\nu^3\rho^2\omega\left(5\omega-17\sqrt{\nu}\right)r^{14}+\nu^2\rho^2\left(-4\sqrt{\nu}\omega+5\nu-18\omega^2\right)r^{16} \\
&-416\nu^4\rho\omega^2r^{20}+2\nu^3\rho\omega\left(29\sqrt{\nu}-3\omega\right)r^{22}+231\nu^4\omega^2r^{28}\Big\}.
\end{aligned}
\tag{3.4.55}
$$

First, checking the asymptotic limit of the Kretschmann scalar

$$\lim_{r\to\infty} K = 0, \tag{3.4.56}$$

it vanishes as expected. Second, the asymptotic expansion is

$$K\Big|_{r\to\infty} = \frac{12R_s^2}{r^6}+\mathcal{O}\left(\frac{1}{r}\right)^7, \tag{3.4.57}$$

in which the leading term is precisely the Schwarzschild Kretschmann scalar. Third, K is always finite over the entire spacetime $r\in[0,\infty)$. It is also determined that (3.4.55) at $r=0$, which previously exhibited a singularity, is now a finite value

$$\lim_{r\to 0^+} K = K\left(r=0\right) = \frac{4}{\sqrt{\rho}}\Big|_{r=0} = \frac{8}{R_s\sqrt{Q_c}}. \tag{3.4.58}$$

This regularity of K is one of the evidences supporting the claim that the singularity of the black hole is resolved in this effective model. Finally, K is regular also at the horizon $r=r_H=\sqrt{R_s^2-Q_b}$, which is another important and desired property. This can be seen explicitly from the values of ν and ρ at the horizon,

$$\nu\left(r=r_H\right) = R_s^2, \tag{3.4.59}$$

$$\rho\nu\left(r=r_H\right) = \left(R_s^2-Q_b\right)^4+\frac{1}{4}Q_cR_s^2. \tag{3.4.60}$$

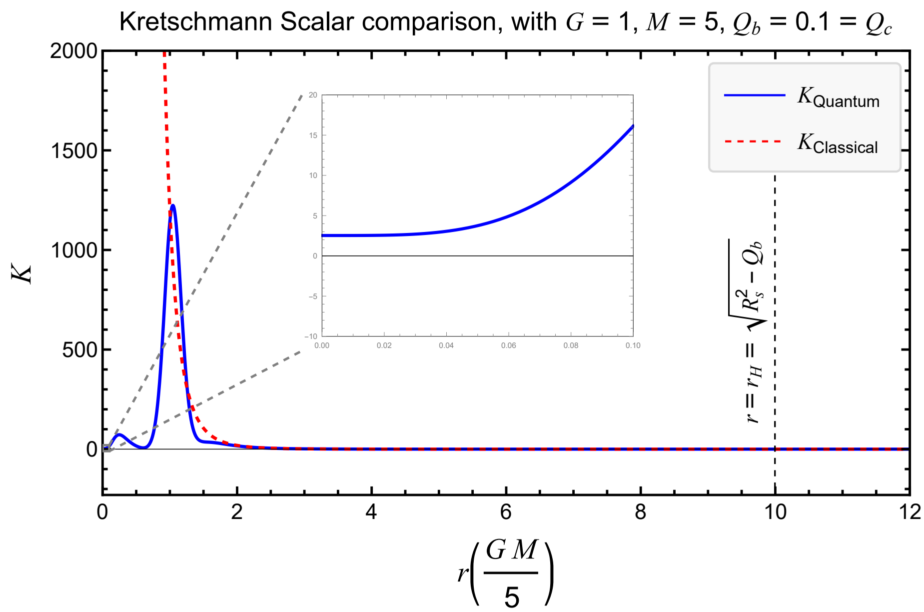

Figure 9: Comparing the classical and effective Kretschmann scalars. It has been zoomed in on the region where the classical and quantum Kretschmann scalars start to deviate. Notice that a different value of Q_c is used from that in previous plots

Some of the above properties can be directly seen from the plot of the Kretschmann scalar in Fig. (9).

It is important to note that these finite and regular values at the horizon and at $r = 0$ and also the correct asymptotic behavior, are a direct consequence of choosing the signs of the β's in (3.4.22)-(3.4.23), which themselves are the result of the reality condition for the metric.

The expansion of two other curvature invariants worth noting are the Ricci scalar and Ricci tensor squared in the asymptotic as well as quantum regimes. The asymptotic expressions at spatial infinity read

$$g^{\mu\nu}R_{\mu\nu} = -\frac{2Q_b}{r^4} + \mathcal{O}\left(\frac{1}{r}\right)^5 \quad \text{and} \quad R_{\mu\nu}R^{\mu\nu} = \frac{12Q_b}{r^8} + \mathcal{O}\left(\frac{1}{r}\right)^9 . \tag{3.4.61}$$

In the quantum regime, as $r \to 0$,

$$g^{\mu\nu}R_{\mu\nu} = \frac{2}{(Q_c R_s^2/4)^{1/4}} \quad \text{and} \quad R_{\mu\nu}R^{\mu\nu} = \frac{2}{(Q_c R_s^2/4)^{1/2}} . \tag{3.4.62}$$

It is seen that the main deviations from general relativity are dominated by the quantum parameter Q_b and the scalars at $r = 0$ are finite, depending on the Q_c quantum parameter.

3.4.5 Effective Stress-Energy Tensor

It is generally expected that the Einstein equations will no longer be the fundamental equations of motion in quantum gravity. While the precise form of the quantum-corrected equations remains unknown, it can still be instructive to study the effective stress-energy tensor derived from the effective metric via the Einstein equations (1.1.1) as well as the effective energy conditions. Assuming an anisotropic perfect fluid the stress-energy tensor takes the form

$$T^{\mu\nu} = (\epsilon + p_\theta)\, U^\mu U^\nu + (p_r - p_\theta)\, W^\mu W^\nu + p_\theta g^{\mu\nu}, \tag{3.4.63}$$

characterized by an effective energy density ϵ, and radial and tangential pressure densities p_r and p_θ $(= p_\phi)$, respectively. Here U^μ is a unit timelike vector field, $U^\mu U_\mu = -1$, which for a comoving fluid becomes

$$U^\mu = \left(\sqrt{-g^{00}}, 0, 0, 0\right), \tag{3.4.64}$$

and W^μ is a unit spacelike vector field, $W^\mu W_\mu = 1$, and satisfying $U^\mu W_\mu = 0$. With these conditions, it becomes

$$W^\mu = \left(0, \sqrt{g^{11}}, 0, 0\right). \tag{3.4.65}$$

Using Einstein's equation $T_{\mu\nu} = \frac{1}{8\pi G} G_{\mu\nu}$ for the exterior,

$$\epsilon = -\frac{1}{8\pi G} g^{00} G_{00}, \tag{3.4.66}$$

$$p_r = \frac{1}{8\pi G} g^{11} G_{11}, \tag{3.4.67}$$

$$p_\theta = \frac{1}{8\pi G} g^{22} G_{22}. \tag{3.4.68}$$

For the interior region, switching $g^{00} \leftrightarrow g^{11}$ and $G_{00} \leftrightarrow G_{11}$ corresponding to $\epsilon \leftrightarrow -p_r$ yields

$$\epsilon = \frac{1}{4\sqrt{2}\pi G} \frac{1}{(Q_c R_s^2)^{1/4}}, \tag{3.4.69}$$

$$p_r = -\frac{1}{4\sqrt{2}\pi G} \frac{1}{(Q_c R_s^2)^{1/4}}, \tag{3.4.70}$$

$$p_\theta = 0, \tag{3.4.71}$$

for the quantum region. Furthermore, the asymptotic behavior of these quantities at $r \to \infty$ is

$$\epsilon = \frac{1}{8\pi G}\frac{R_s Q_b}{r^5} + \mathcal{O}\left(\frac{1}{r}\right)^7 , \tag{3.4.72}$$

$$p_r = -\frac{1}{4\pi G}\frac{Q_b}{r^4} + \mathcal{O}\left(\frac{1}{r}\right)^5 , \tag{3.4.73}$$

$$p_\theta = \frac{1}{4\pi G}\frac{Q_b}{r^4} + \mathcal{O}\left(\frac{1}{r}\right)^5 . \tag{3.4.74}$$

It is clear that the asymptotic behavior is dominated by Q_b and corrections due to Q_c are subdominant.

The energy conditions can now be calculated. The weak energy condition is satisfied if $\epsilon \geq 0$ and $\epsilon + p_i \geq 0$ with $i = r,\, \theta,\, \phi$, noting that $p_\theta = p_\phi$. The strong energy condition is satisfied if $\epsilon + p_i \geq 0$ and $\epsilon + \sum_i p_i \geq 0$. Finally, the dominant energy condition is satisfied if $\epsilon \geq |p_i|$. From (3.4.69)-(3.4.71), notice at the origin, $r = 0$, the weak, strong and dominant energy conditions are satisfied. However, at $r \to \infty$, the leading terms of (3.4.72)-(3.4.74), violate all energy conditions, although they all vanish at infinity and thus are nonviolating.

It is important to emphasize that these are not a (non)violation of an actual matter field energy condition, since this is a vacuum model. One only obtains a stress-energy tensor if one uses the Einstein's equations. However, these are not the equations of motion in this model, since this is a modified theory due to quantum gravity effects. Thus one should not read too much into the above energy conditions.

3.5 Geodesics

The metric's static and spherical symmetry implies three spatial Killing vector fields and one asymptotically timelike Killing vector field, associated with rotational symmetry and geodesic energy, respectively. Hence the direction of the angular momentum can be fixed at $\theta = \pi/2$ and its conserved magnitude is

$$L = g_{22}\frac{d\phi}{d\lambda} = \rho^{\frac{1}{4}}\frac{d\phi}{d\lambda}, \tag{3.5.1}$$

where λ is the affine parameter of the geodesics. The conserved energy of the geodesics is

$$E = -g_{00}\frac{dt}{d\lambda} = \sqrt{\frac{\nu}{\sqrt{\rho}}}\left(\sqrt{\nu} - R_s\right)\frac{dt}{d\lambda}. \tag{3.5.2}$$

Additionally, the constant of motion along the path is given by

$$\varepsilon = -g_{\mu\nu}\frac{dx^{\mu}}{d\lambda}\frac{dx^{\nu}}{d\lambda} = \begin{cases} 0, & \text{null geodesics} \\ 1, & \text{timelike geodesics} \end{cases}. \tag{3.5.3}$$

Using these conserved quantities, the geodesic equation reduces to a single effective potential form

$$-\frac{1}{2}g_{00}g_{11}\left(\frac{dr}{d\lambda}\right)^2 - \frac{1}{2}g_{00}\left[\frac{L^2}{g_{22}} + \varepsilon\right] = \frac{1}{2}E^2, \tag{3.5.4}$$

which for the current model is given by

$$\frac{1}{2}\frac{\nu}{r^2}\left(\frac{dr}{d\lambda}\right)^2 + V_{\text{eff}} = \bar{E}, \tag{3.5.5}$$

with the effective potential V_{eff} and the energy $\bar{E}$ defined as

$$V_{\text{eff}} = -\frac{1}{2}g_{00}\left[\frac{L^2}{g_{22}} + \varepsilon\right] = \frac{1}{2}\sqrt{\frac{\nu}{\sqrt{\rho}}}\left(\sqrt{\nu} - R_s\right)\left[\frac{L^2}{\rho^{\frac{1}{4}}} + \varepsilon\right], \tag{3.5.6}$$

$$\bar{E} = \frac{1}{2}E^2. \tag{3.5.7}$$

Given that ν/r^2 never vanishes in this model, the circular orbits are located at r for which $dV_{\text{eff}}/dr = 0$.

3.5.1 Null Geodesics and photon sphere

For null geodesics ($\varepsilon = 0$), the photon sphere corresponds to a circular orbit where $dV_{\text{eff}}/dr = 0$. The effective potential is:

$$V_{\text{eff}} = \frac{1}{2}\sqrt{\frac{\nu}{\sqrt{\rho}}}\left(\sqrt{\nu} - R_s\right)\left[\frac{L^2}{\rho^{\frac{1}{4}}}\right], \tag{3.5.8}$$

and so $dV_{\text{eff}}/dr = 0$ becomes

$$\frac{1}{2}\left(1 + \sqrt{\rho}\right)\frac{1}{\rho}\frac{d\rho}{dr} = \left(1 + \sqrt{\rho}\frac{\sqrt{\nu}}{\sqrt{\nu} - R_s}\right)\frac{1}{\nu}\frac{d\nu}{dr}. \tag{3.5.9}$$

This equation cannot be solved analytically but important information on how to proceed can be obtained from the plot of the potential and its derivative that is presented in Fig. (10). From this figure it is evident that for the null case there seems to be only one maximum, i.e., an unstable circular orbit, outside of the black hole relatively close to the classical photon

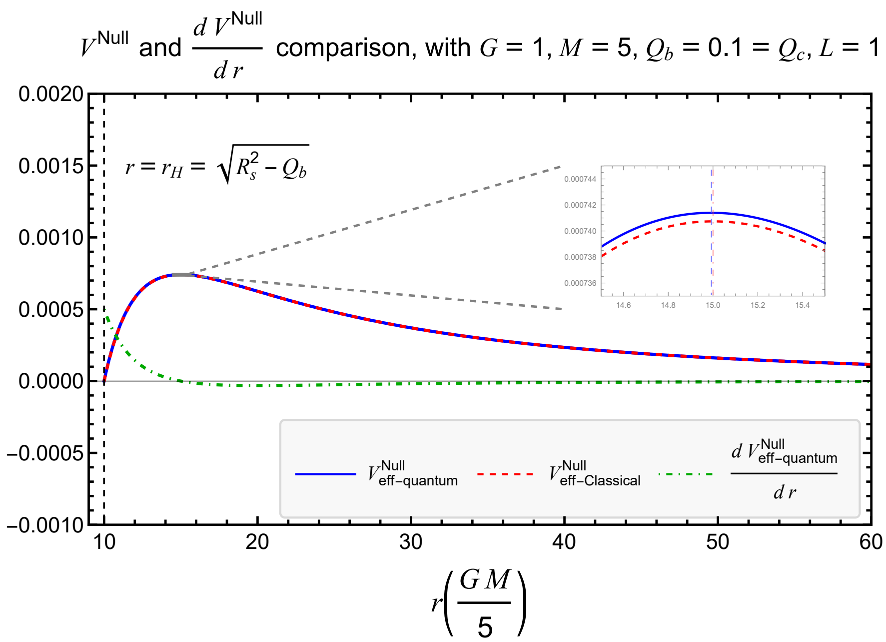

Figure 10: The null effective potential for both the classical and quantum cases, and the derivative of the effective potential in the exterior. It is seen that there seems to be only one extremum in the exterior which is a maximum. This marks the position of the photon sphere. The zoomed-in part shows that the effective photon sphere has a smaller radius (vertical dashed blue line) compared to the classical one (vertical dot dashed red line at $3R_s/2$).

sphere which is at $r_{\text{ph}}^{\text{class}} = 3R_s/2$. To approximate the position of the effective exterior photon sphere from this observation, first expand dV_{eff}/dr up to first order in Q_b and Q_c. Then expand the resulting expression for $r = 3R_s/2 + \delta r$ with $\delta r \to 0$ up to the first order in δr. Next solve this approximate $dV_{\text{eff}}/dr = 0$ for δr and finally expand this δr up to the first order in Q_b and Q_c. The result is the approximate position of the photon sphere given by

$$r_{\text{ph}}^{\text{quat}} = \frac{3R_s}{2} - \frac{7Q_b}{9R_s} + \frac{64Q_c}{6561R_s^5}. \tag{3.5.10}$$

As expected, the leading correction is only in Q_b, since this is the quantum parameter that is important near the horizon.

3.5.2 Timelike geodesics

Setting $\varepsilon = 1$ in $dV_{\text{eff}}/dr = 0$ yields the condition for circular orbits in the timelike case. This equation still cannot be solved analytically and must be approximated through observation of its plot along with V_{eff} now given by

$$V_{\text{eff}} = \frac{1}{2}\sqrt{\frac{\nu}{\sqrt{\rho}}}\left(\sqrt{\nu} - R_s\right)\left[\frac{L^2}{\rho^{\frac{1}{4}}} + 1\right]. \tag{3.5.11}$$

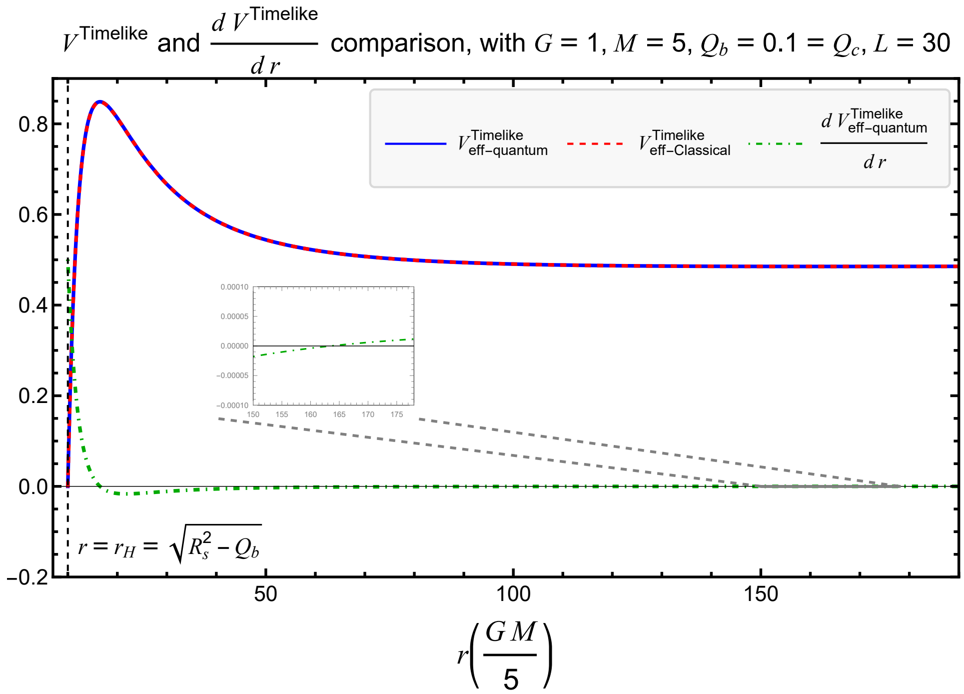

Figure 11: The timelike effective potential for both the classical and quantum cases, and the derivative of the effective potential in the exterior. The quantum curve is qualitatively similar to the classical one where there are two circular orbits in the exterior.

Figure (11) shows the effective potential in the exterior of the black hole, it appears there are only two extrema for V_{eff} corresponding to two circular orbits, just as in the classical case. The location of these in the quantum black hole are different from the classical ones only by a very small amount. This should be expected since the computations until now show that the exterior of this black hole exhibit similar qualitative behaviors as the classical Schwarzschild black hole.

3.6 Painlevé-Gullstrand coordinates and infalling observers

It was introduced in Section 1.2.2 that the Painlevé-Gullstrand coordinates can be used to study the behavior of infalling observers crossing the horizon, avoiding the coordinate singularity there. The PG coordinates are derived from the Schwarzschild coordinates by making a coordinate transformation $t \to t_{\text{PG}}(r,t)$ where t_{PG} is the proper time of the geodesics of an infalling observer with initial zero radial velocity and vanishing angular momentum and

$$dt_{\text{PG}} = dt + \sqrt{-g_{11}\left(1 + \frac{1}{g_{00}}\right)}dr \tag{3.6.1}$$

The PG metric takes the form:

$$ds^2 = g_{00}^{(\mathrm{PG})} dt_{\mathrm{PG}}^2 + 2g_{01}^{(\mathrm{PG})} dt_{\mathrm{PG}} dr + g_{11}^{(\mathrm{PG})} dr^2 + g_{22}^{(\mathrm{PG})} d\Omega^2. \tag{3.6.2}$$

This means the metric for the current model can be written in PG coordinates,

$$g_{00}^{(\mathrm{PG})} = g_{00} = -\frac{\sqrt{r^2 + Q_b}}{\left(r^8 + \frac{1}{4}Q_c R_s^2\right)^{\frac{1}{4}}} \left(\sqrt{r^2 + Q_b} - R_s\right), \tag{3.6.3}$$

$$g_{01}^{(\mathrm{PG})} = -g_{00}\sqrt{-g_{11}\left(1 + \frac{1}{g_{00}}\right)} = \sqrt{1 + \frac{Q_b}{r^2}} \sqrt{1 - \frac{\sqrt{r^2 + Q_b}\left(\sqrt{r^2 + Q_b} - R_s\right)}{\left(r^8 + \frac{1}{4}Q_c R_s^2\right)^{\frac{1}{4}}}}, \tag{3.6.4}$$

$$g_{11}^{(\mathrm{PG})} = -g_{00}g_{11} = 1 + \frac{Q_b}{r^2}, \tag{3.6.5}$$

$$g_{22}^{(\mathrm{PG})} = g_{22} = \left(r^8 + \frac{1}{4}Q_c R_s^2\right)^{\frac{1}{4}}. \tag{3.6.6}$$

This metric can be used to study the behavior of infalling observers crossing the horizon.

3.6.1 Velocity and proper time of the infalling geodesics

In PG coordinates, key properties of an infalling observer with zero initial radial velocity and vanishing angular momentum can be calculated. First, the radial velocity of an infalling observer into the black hole can be computed in its own proper time. For this, replace ds^2 in (3.6.2) with $-d\tau^2$ as well as dt_{PG} with $d\tau$. The result is

$$-1 = g_{00}^{(\mathrm{PG})} + 2g_{01}^{(\mathrm{PG})}\frac{dr}{d\tau} + g_{11}^{(\mathrm{PG})}\left(\frac{dr}{d\tau}\right)^2, \tag{3.6.7}$$

with the solution

$$v_{\mathrm{rain}} = \frac{dr}{d\tau} = \frac{-g_{01}^{(\mathrm{PG})} \pm \sqrt{-g_{00}^{(\mathrm{PG})} g_{11}^{(\mathrm{PG})} + \left(g_{01}^{(\mathrm{PG})}\right)^2 - g_{11}^{(\mathrm{PG})}}}{g_{11}^{(\mathrm{PG})}}. \tag{3.6.8}$$

This results in a velocity of

$$v_{\mathrm{rain}} = \frac{dr}{d\tau} = -\frac{r}{\sqrt{\nu}}\sqrt{1 - \frac{\sqrt{\nu}\left(\sqrt{\nu} - R_s\right)}{\rho^{\frac{1}{4}}}}. \tag{3.6.9}$$

In the classical limit, the velocity will diverge at $r \to 0$ since $\rho_{\mathrm{class}} \propto r^8$. However, quantum corrections stop this expression from diverging, since ρ does not vanish in the quantum

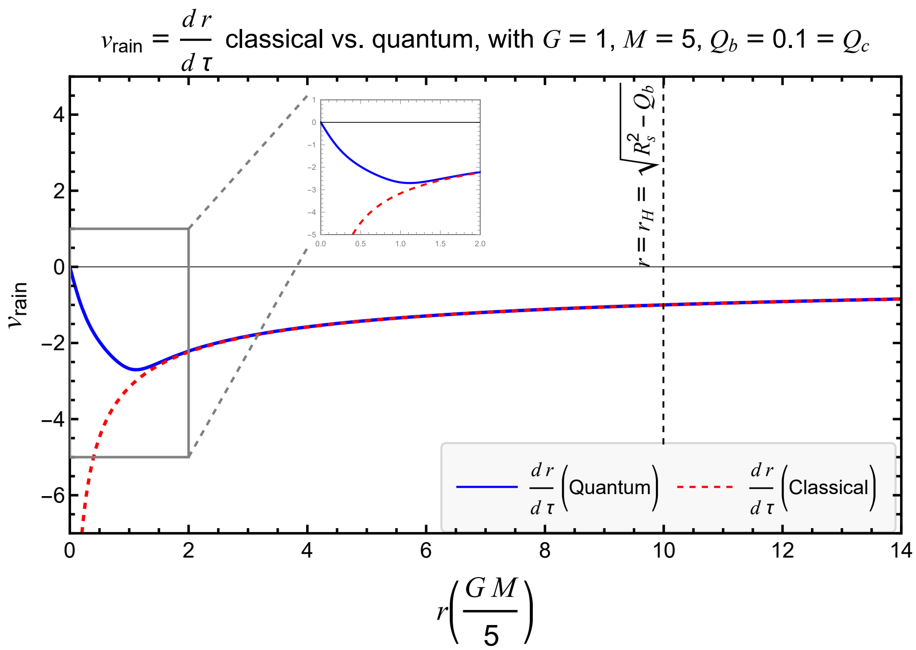

Figure 12: Radial velocity of an infalling observer in Painleve̓-Gullstrand coordinates for the classical and quantum cases.

regime due to the presence of quantum parameter Q_c in (3.4.27). Figure (3.6.1) shows that the classical velocity of a radially infalling observer diverges, versus the quantum corrected velocity which is zero at $r = 0$. From this, it is clear that the deciding factor in non-divergence of the radial infalling velocity is Q_c and that Q_c governs the important quantum effects close to the $r = 0$ region.

3.7 Expansion and Raychaudhuri equation

The next step is to calculate the Raychaudhuri equation to study the behavior of the null geodesics in this improved extended spacetime in PG coordinates. As in standard geodesic analyses [6], the expansion, shear, and vorticity are calculated. Vorticity vanishes for radial null geodesics due to spherical symmetry, and shear is zero in the absence of metric perturbations. The remaining expansion and shear terms are

$$\theta_\pm = \frac{r^8}{\ell^0\sqrt{r^2+Q_b}\left(r^8+\frac{1}{4}Q_cR_s^2\right)}\left(\pm 1 - \sqrt{1+\frac{\sqrt{r^2+Q_b}\left(R_s-\sqrt{r^2+Q_b}\right)}{\left(r^8+\frac{1}{4}Q_cR_s^2\right)^{\frac{1}{4}}}}\right), \quad (3.7.1)$$

$$\sigma_{\mu\nu}\sigma^{\mu\nu} = 0, \quad (3.7.2)$$

where $+$ and $-$ correspond to outgoing and ingoing geodesics, respectively. $\ell_0 > 0$ is an overall constant left over from the auxiliary field conditions. The classical limit, $Q_b \to 0$ and $Q_c \to 0$, of the expansion scalar matches that of the classical Schwarzschild black hole in PG coordinates, particularly for $\ell^0 = 1/2$,

$$\theta_{\pm}^{\text{class.}} = \frac{2}{r}\left(\pm 1 - \sqrt{\frac{R_s}{r}}\right). \tag{3.7.3}$$

Furthermore,

$$\theta_{\pm}\left(r=0\right) = 0. \tag{3.7.4}$$

The finiteness of $\theta_{\pm}$ everywhere, particularly at $r = 0$, provides another strong indication of the resolution of singularity. It is also instructive to look at the expansion at $r = r_H$,

$$\theta_{\pm}(r = r_H) = \frac{4(\pm 1 - 1)\left(Q_b - R_s^2\right)^4}{\ell^0 R_s\left[4\left(Q_b - R_s^2\right)^4 + Q_c R_s^2\right]} \tag{3.7.5}$$

It is particularly important to note that while θ_- is always negative (except at $r = 0$), the outward expansion θ_+ is positive in the exterior, becomes zero at the horizon $r = r_H$, and is negative in the interior. This shows that the black hole region is a trapped region as expected.

The Raychaudhuri equation describes the evolution of the expansion scalar in terms of the affine parameter of the geodesics. Recall that for null geodesics the Raychaudhuri equation is

$$\frac{d\theta}{d\lambda} = -\frac{1}{2}\theta^2 - \sigma_{\mu\nu}\sigma^{\mu\nu} + \omega_{\mu\nu}\omega^{\mu\nu} - R_{\mu\nu}k^{\mu}k^{\nu}. \tag{3.7.6}$$

Once again, only in the classical regime $R_{\mu\nu} = 0$, in the effective regime however, the equations of motion are not Einstein's equations and hence $R_{\mu\nu} \neq 0$. In this regime, the Raychaudhuri equation becomes

$$\begin{aligned}\frac{d\theta_{\pm}}{d\lambda} =& \frac{r^8\left(r^{10} - \frac{7}{4}Q_c R_s^2 r^2 - 2Q_c Q_b R_s^2\right)}{\left(r^2+Q_b\right)^2\left(r^8 + \frac{1}{4}Q_c R_s^2\right)^2\left(\ell^0\right)^2}\times \\ &\left[\pm\sqrt{1 + \frac{\sqrt{r^2+Q_b}\left(R_s - \sqrt{r^2+Q_b}\right)}{\left(r^8+\frac{1}{4}Q_c R_s^2\right)^{1/4}}} - \frac{\sqrt{r^2+Q_b}\left(R_s - \sqrt{r^2+Q_b}\right)}{2\left(r^8+\frac{1}{4}Q_c R_s^2\right)^{1/4}} - 1\right]\end{aligned} \tag{3.7.7}$$

This expression never diverges and in particular becomes zero at $r = 0$. Furthermore, the

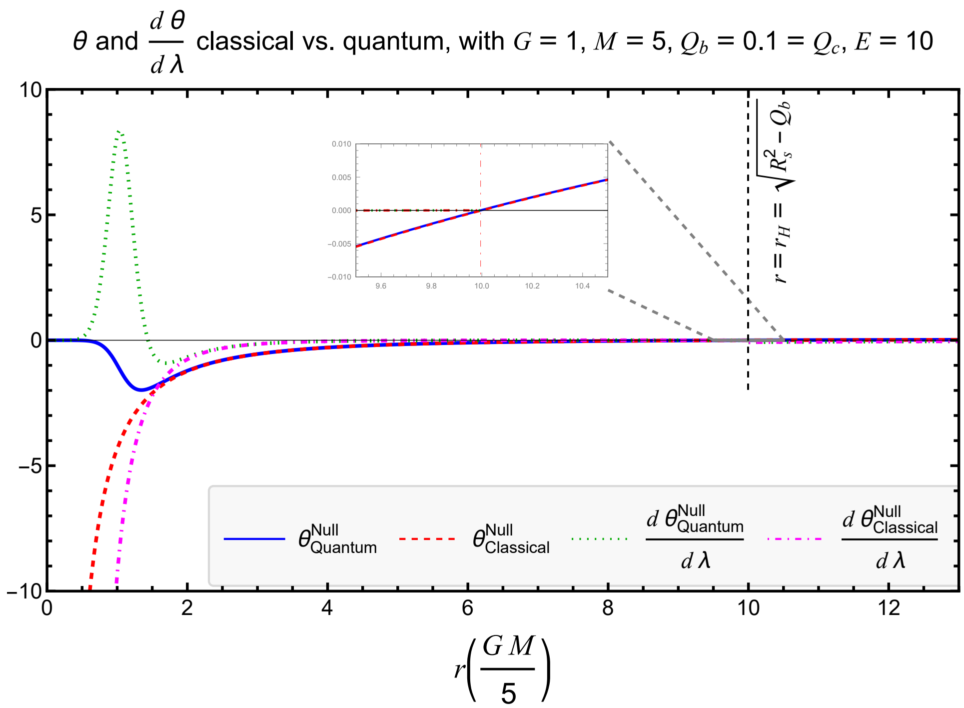

Figure 13: The plot of the outgoing expansion scalar θ_+ and the corresponding Raychaudhuri equation $d\theta_+/d\lambda$ for a congruence of null radial geodesics. It is clear that the quantum versions are finite everywhere particularly at $r = 0$ where they vanish.

classical limit of this expression yields

$$\frac{d\theta_\pm}{d\lambda} = \frac{1}{2r^3\left(\ell^0\right)^2}\left[\pm 2\sqrt{rR_s} - r - R_s\right] \tag{3.7.8}$$

which does diverge at $r \to 0$. A plot of both θ_+ and $d\theta_+/d\lambda$ for outgoing rays is presented in Fig. (13). The finiteness, and in fact vanishing, of both null $\theta_\pm$ and $d\theta_\pm/d\lambda$ over the entire spacetime, along with the regularity of the Kretschmann scalar everywhere in this spacetime indicates that the singularity is resolved in this quantum black hole model.

3.8 Discussion and conclusions

This work investigates the analytical continuation of the GUP-inspired black hole's interior metric, introduced in [101] and detailed in Section 3.4, to the full spacetime by interchanging the radial and temporal coordinates ($t \leftrightarrow r$), analogous to the Schwarzschild case where the interior and exterior metrics are similarly related. It was shown that the resulting extended metric and consequently the Kretschmann scalar exhibit issues in the asymptotic ($r \to \infty$) region in that g_{00} will not be in the desired form and the Kretschmann scalar will fall of as r^{-4} instead of r^{-6}.

To remedy these issues, the idea of introducing an "improved-scheme" was borrowed from the techniques used in loop quantum gravity, as was introduced in 2.5. In this specific model, the minimal uncertainty parameters are β_b and β_c, which were modified to $\bar{\beta}_b = \beta_b L_0^4/p_b^2$ and $\bar{\beta}_c = \beta_c L_0^4/p_c^2$, where p_b and p_c are momenta of the theory which correspond to the components of the densitized triads; essentially the components of the metric. Remarkably, this rather simple prescription, not only results in all the desired asymptotic behaviors, but also renders the black hole regular. Furthermore, the Kretschmann scalar vanishes at $r \to \infty$ as in the classical case, and more importantly, its expansion up to zeroth order in quantum parameters exactly matches that of the Schwarzschild metric. In addition, the classical limits ($\beta_b \to 0$ and $\beta_c \to 0$) match the classical Schwarzschild spacetime. In order for the metric components to always remain real, β_b and β_c should be negative. These requirements then lead directly to the resolution of the singularity by rendering the denominator of the Kretschmann scalar positive and nonzero for any value of the radial coordinate r, including the horizon. The null expansion and the Raychaudhuri equation for a congruence of null geodesics demonstrate their regularity everywhere in this spacetime, which together with regularity of the Kretschmann scalar, indicates that the singularity is resolved in this quantum black hole spacetime.

The construction presented here implements the generalized uncertainty principle (GUP) at the level of particle dynamics, which, while effective for illustrating key features of singularity resolution, inherits the limitations of a minisuperspace approach. A natural question arises: can the GUP be consistently extended to field theory, and if so, would such a formulation provide a more fundamental path toward deriving effective spacetime metrics?

Extensions of GUP to quantum field theory have been explored, for example in the context of modified commutation relations for field modes and deformed canonical structures [96, 113, 114]. These approaches introduce modifications to the field momentum operators or mode expansions, but a consistent and covariant formulation of GUP in curved spacetime field theory remains an open challenge. In particular, incorporating a minimal length while maintaining general covariance and locality leads to ambiguities, especially when defining smeared fields or constructing stress-energy tensors.

As a result, while a GUP-modified field theory might, in principle, provide a more fundamental derivation of effective spacetimes, perhaps even allowing one to identify coordinate systems such as Painlevé–Gullstrand as naturally adapted to the modified dynamics, a systematic procedure to do so is not currently available. The approach adopted in this chapter thus remains at the effective level, capturing key features of GUP phenomenology such as a minimal length and modified Hamiltonian dynamics without relying on a full quantum field-theoretic treatment.

4 Model metrics for quantum black hole evolution

Section 2.1 discussed how LQG and its symmetry-reduced counterpart, LQC, resolve classical singularities predicted by general relativity, such as those appearing in black holes and at the big bang, through quantum geometric effects. Other candidate theories of quantum gravity offer alternative mechanisms for singularity resolution. For instance, string theory addresses black hole singularities via the fuzzball paradigm [115], wherein the classical singularity and event horizon are replaced by a "fuzzy," stringy configuration without a central singularity [116]. In group field theory condensate cosmology, spacetimes emerge as condensates of quantum geometric degrees of freedom, and bounce dynamics can arise naturally within this framework [117]. Similarly, approaches such as spin foam cosmology [118, 119], models based on quantum reduced loop gravity [120], and as previously presented, generalized uncertainty principle [121, 122], also provide mechanisms for avoiding curvature singularities, often featuring a bounce in the effective spacetime description.

Regardless of which theory of quantum gravity ultimately prevails, it is clear that the common goal among all candidates is the resolution of curvature singularities via quantum effects. Motivated by this common feature, the present chapter introduces an effective spacetime construction that encodes features anticipated from quantum gravity—such as dynamical gravitational collapse with resolution of the singularity through a smooth bounce [123]. This construction is not derived from a specific quantum gravity theory but is designed phenomenologically to capture generic features expected of a non-singular quantum-corrected spacetime.

4.1 Metric for Gravitational Collapse

Although it may seem taboo, constructing spacetime metrics based on phenomenological assumptions is well-established, as seen in metric engineering for wormholes [124] and warp drives [125], where metrics are designed to exhibit specific physical properties. This pragmatic approach allows one to explore physically interesting geometries without requiring a full derivation from an underlying fundamental theory. In this spirit, this section constructs a class of spherically symmetric metrics that describe gravitational collapse followed by a nonsingular bounce, with asymptotic flatness and agreement with the Schwarzschild solution outside a compact inner region.

The starting point is the generic spherically symmetric metric of the form

$$ds^2 = -N^2(x,t)dt^2 + f^2(x,t)\left(dx + N^x(x,t)dt\right)^2 + g^2(x,t)d\Omega^2, \tag{4.1.1}$$

where N is the lapse, N^x is the shift, x is a radial coordinate and $f(x,t)$, $g(x,t)$ are arbitrary functions. A particular and useful case of this metric is the Painlevé-Gullstrand (PG) form [126, 127] obtained by setting $g(x,t) = r$, $N(r,t) = 1 = f(r,t)$, and

$$N^x(r,t) = \sqrt{\frac{2Gm(r,t)}{r}}. \tag{4.1.2}$$

This reduces to the the form of Eq. (1.2.4), now with a time and radial dependent mass. The PG coordinates cover the classical spacetime of matter collapse, and are expected to also be sufficient to capture a matter bounce. The shift function (4.1.2) defines the mass $m(r,t)$ to be the mass contained within a radius r at a time t and is related to density via

$$m(r,t) = 4\pi \int_0^r r^2 \rho(r,t) dr. \tag{4.1.3}$$

For asymptotic flatness, the mass function must satisfy:

$$\lim_{r\to\infty} m(r,t) = M, \tag{4.1.4}$$

where M is the Arnowitt-Deser-Misner (ADM) mass, the total energy and momentum contained within the asymptotically flat spacetime. Next, the mass function must initially move toward $r = 0$, reverse direction at some small r, and then move outward. This behaviour is modeled by

$$m(r,t) = M_0 \left[1 + \tanh\left(\frac{r - r_0 - v(r,t)t}{\alpha\, l_0}\right)\right]^a \tanh\left(\frac{r^b}{l_0^b}\right). \tag{4.1.5}$$

Here l_0 is a scale (typically the Planck length); r_0 is associated with the radial position of the bounce; M_0 scales the total ADM mass M; α determines how sharply the mass function rises; a and b are positive integers (or reals) to be chosen such that the density

$$\rho(r,t) = \frac{1}{4\pi r^2}\frac{\partial m}{\partial r} \tag{4.1.6}$$

is bounded as $r \to 0$, a feature necessary for singularity avoidance and $v(r,t)$ is the velocity function of the density profile. While the pressure is assumed to vanish. The hyperbolic tangent function is the simplest choice that captures the desired properties of the mass function but it is important to note that there are many functions that could describe this property, and the one chosen here is far from unique. The velocity function is chosen to model an initially inward-falling mass profile that bounces and expands outward, speeding up during collapse and slowing down during expansion. These features are captured in the function

$$v(r,t) = \frac{A}{(1+r)^n} \tanh\left(\frac{t-t_0}{l_0}\right), \tag{4.1.7}$$

where $A > 0$ is a real constant t_0 is the time when the bounce occurs, and n is a positive constant.

Thus the metric designed to model non-singular gravitational collapse and bounce, as might emerge from a quantum theory of gravity is given by

$$ds^2 = -\Big(1 - \frac{2Gm(r,t)}{r}\Big)dt^2 + 2\sqrt{\frac{2Gm(r,t)}{r}}dtdr + dr^2 + r^2 d\Omega^2. \tag{4.1.8}$$

As mentioned, such metrics are not unique, but the one presented here captures interesting dynamical features such as "horizon bubbles" speculated on in [128].

4.2 Physical properties

It is instructive to study several interesting properties of the phenomenological metric in Section 4.1. These properties include the evolution of mass and density, horizon formation and annihilation, and black hole lifetime. The last feature is a function of the power n in the velocity function (4.1.7) defined above.

4.2.1 Horizons

As discussed in Section 1.2, spherical symmetry simplifies horizon location. They can be determined by,

$$\Theta(r,t) = g^{rr} = 1 - \frac{2Gm(r,t)}{r} = 0. \tag{4.2.1}$$

In stationary spacetimes, this defines the apparent horizon, where the outgoing null geodesic expansion vanishes, with

$$\theta_+(r,t) = \frac{2}{r}\Big(- N^r + 1\Big). \tag{4.2.2}$$

However, in dynamical spacetimes, this condition instead defines a trapping horizon, a hypersurface in spacetime foliated by apparent horizons across different time slices. The trapping horizon captures the dynamic behavior of horizon formation, evolution, and disappearance and generalizes the notion of an apparent horizon to a time-dependent setting. Solving (4.2.1) analytically is challenging, but plotting it provides insight. Figure (14) shows time sequences of the mass function (4.1.5), density (4.1.6), and the horizon function (4.2.1). The first row shows the incoming density and horizons appearing, and the second row shows matter bouncing and horizons disappearing as matter moves outward. Fig. (15) shows the density profile's evolution, illustrating the bounce and outward expansion. The parameters used for

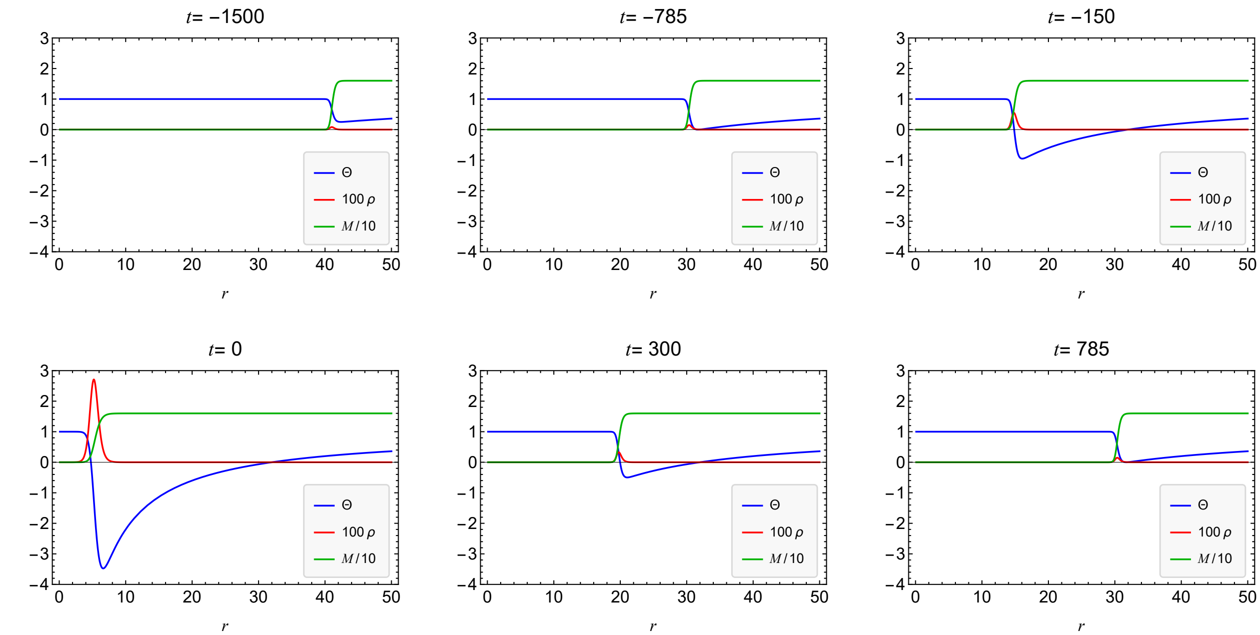

Figure 14: Time sequences of the mass function m (green), density ρ (red), and horizon function Θ (blue): the first row shows in-going matter with horizons (roots of the Θ) appearing, and the second row shows matter bouncing and moving outward. Horizons eventually disappear by the last frame. The outer horizon for most of the evolution remains at a fixed location until it disappears with the root of Θ.

the figures are $a = 2$, $b = 3$, $\alpha = 1$, $M_0 = 4$, and $r_0 = 5$ in the mass function (4.1.5), and $A = n = 1$ in the velocity function (4.1.7). These values are chosen for illustration; qualitatively similar results arise for other choices.

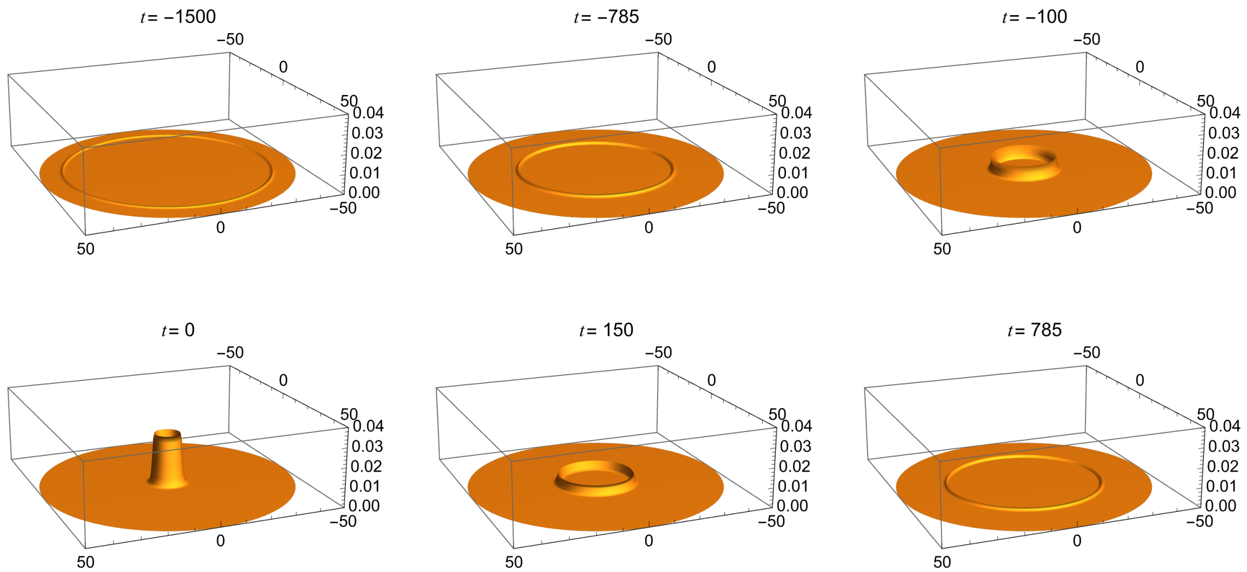

Figure 15: Density function $\rho(r,t)$ at the indicated times. The frames top-left to bottom-right show how the ingoing density profile nears $r = 0$, bounces, and moves outward.

The horizon dynamics are further analyzed in Fig. (16), showing the horizon trajectory in the r, t plane: the red line is the outer horizon, the blue one is the inner horizon, and the green line shows the peak of the density function. In region 1, a pair of horizons form and diverge. The inner horizon and density peak then move inward together, bounce in region 4 after hitting a minimum radius, and then travel outward until the inner and outer horizons merge and annihilate in region 6.

Figure (17) shows a closer look at how the peak of the density behaves as it moves with the inner horizon, and the causal nature of each region is further investigated by determining the behaviour of lightcones within each region. The following features are apparent in Fig. (17):

- Region 1: after formation the outer horizon (red) is spacelike and becomes null, and the inner horizon becomes timelike.
- Region 2: the density peak (green) crosses from outside the inner horizon to the region between the two horizons, the inner horizon is timelike, the density peak is timelike before crossing into the region between the two horizons and becomes spacelike after moving into that region.
- Region 3: the outer horizon is null for nearly all of its finite lifetime.
- Region 4 is the bounce phase: the inner horizon and density peak change from ingoing to outgoing. The inner horizon changes from timelike to spacelike, and the density

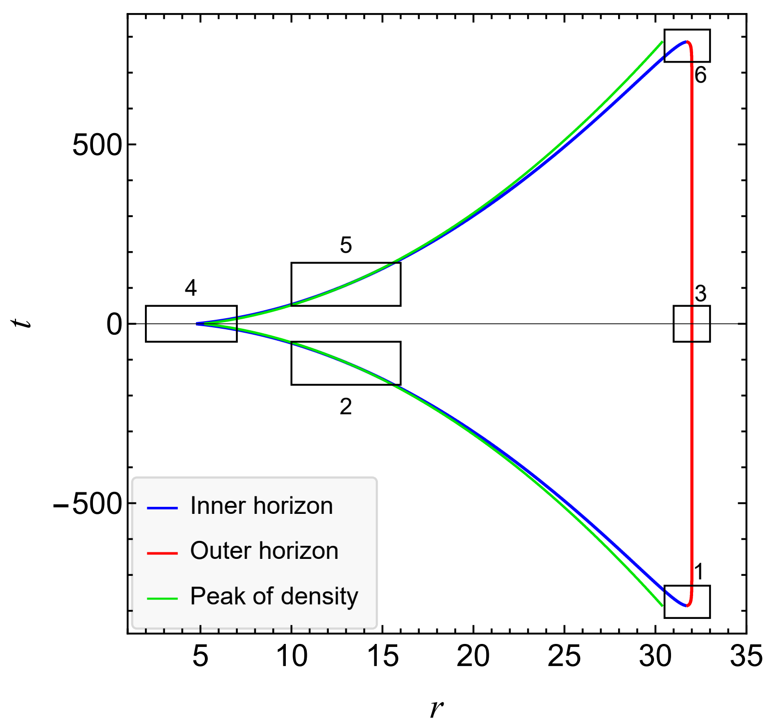

Figure 16: Horizon and density peak trajectories. Horizons form and diverge from point 1, density peak (green) and inner horizon (blue) bounce at point 4, and the inner (blue) and outer (red) horizons merge and annihilate at point 6 (details of each region appear magnified in the next figure).

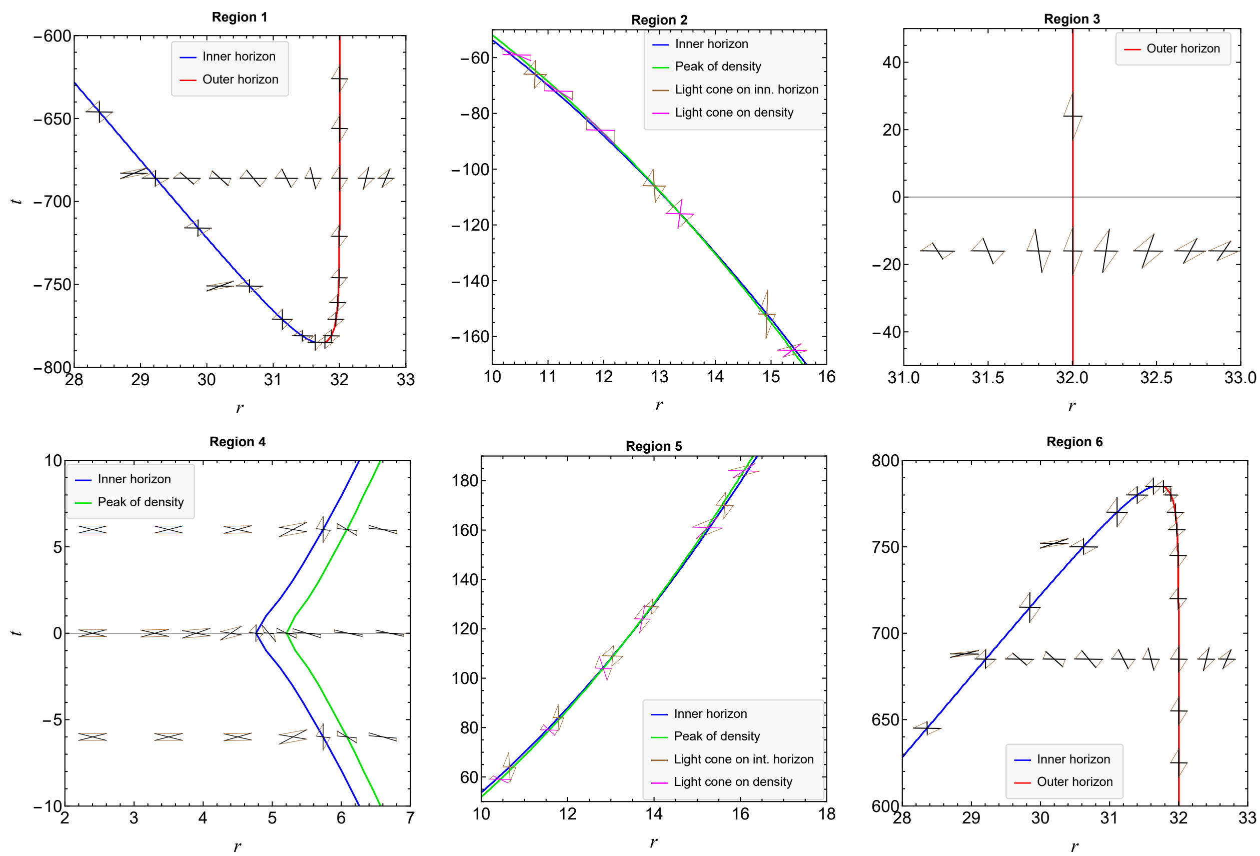

Figure 17: Close up of regions 1-6 of Fig. (16). R1: Horizons form. The outer one becomes null and stays at constant radius, while the inner one is timelike. R2: the peak density crosses from the interior of the inner horizon to the region between the two horizons. R3: the outer horizon becomes null after its formation. R4: the inner horizon and matter density bounce. The inner horizon goes from timelike to spacelike and the peak matter density stays spacelike inside the region between the two horizons. Lightcones near $r = 0$ resemble those of flat spacetime. R5: matter density peak emerges from within the region between the two horizons and becomes timelike. R6: inner and outer horizons merge and annihilate.

peak (green) remains spacelike while inside the regions between the two horizons. The region to the left of the inner horizon is nearly flat.

- Region 5: this is a near reflection of region 2. The density peak emerges from within the inner horizon and becomes timelike, while the inner horizon remains spacelike.
- Region 6: the inner and outer horizons merge and the black hole region disappears. The density peak (not shown) is timelike and propagates outward.

Throughout this process the density peak remains timelike while it is outside the region between the two horizons. The density profile is Gaussian-like, with extended tails straddling the inner horizon, unlike a thin shell. In this way, while its peak enters and exits the region

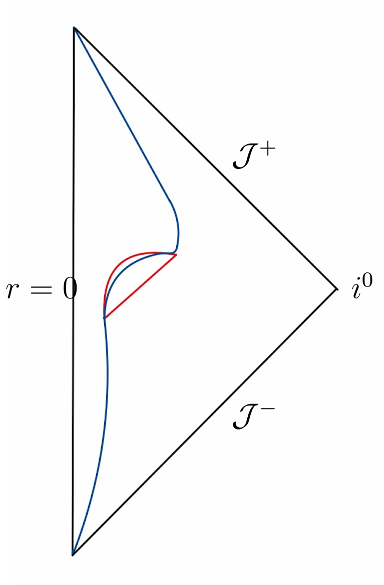

Figure 18: Conformal diagram for the metric with mass function (4.1.5). The red lines show the horizons. The outer horizon segment is null. The inner horizon is timelike before the bounce and becomes spacelike after the bounce. The blue line is the peak of the density profile. It is timelike outside the bubble region (between the horizons) and spacelike inside it.

between the two horizons becoming spacelike, portions of the extended density profile can remain timelike outside the trapped region. It would require a more microscopic view to take into account the thickness of the density profile.

Figure (18) shows the Penrose diagram corresponding to Fig. (16). The red bubble is the region between the two horizons. The outer horizon is a null segment of what classically would be the event horizon. The inner horizon is timelike, then becomes spacelike after the bounce. The blue matter density peak follows the inner horizon, enters the bubble region, and then emerges before the horizons merge and disappear.

4.2.2 Black hole lifetime

Regardless of the process through which a black hole meets its ultimate demise, the time interval for which it exists can be regarded as the black hole lifetime. In this scenario the black hole lifetime T_{BH} is simply the time interval between horizon pair formation t_i (when roots of $\Theta(r,t)$ first appear) and horizon annihilation t_f (when roots of $\Theta(r,t)$ disappear):

$$T_{\rm BH} = t_f - t_i. \tag{4.2.3}$$

For the case shown in Fig. (16), this is approximately the time interval between regions 1 and 6. With a given velocity function of the form (4.1.7), and ADM mass associated with the

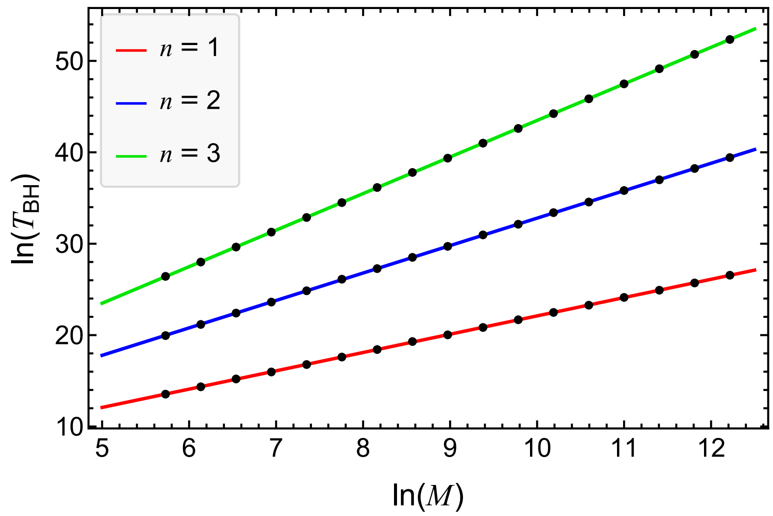

Figure 19: Black hole lifetime $T_{\rm BH}$ as a function of ADM mass M with mass function (4.1.5) and velocity (4.1.7). The lines are fit by the formula $T_{\rm BH} \approx 2^{n+2}M^{n+1}$

mass function (4.1.5), $T_{\rm BH}$ is readily determined by numerically tracking the roots of $\Theta(r,t)$. (This process was also followed in [129], with the same definition of black hole lifetime).

The power n in the velocity function (4.1.7) determines the ingoing and outgoing radially dependent velocity for a fixed parameter A; the larger the value of n, the slower the speed, and hence the longer the lifetime. This is confirmed by Fig. (19), showing log-log graphs of $T_{\rm BH}$ vs. ADM mass M for $n = 1, \ldots, 3$ with $A = 1$ in (4.1.7). The fit to these points is well approximated by the formula

$$T_{\rm BH} \approx 2^{n+2}M^{n+1}. \tag{4.2.4}$$

This expression quantitatively ties the power n in the velocity function to the black hole lifetime as defined above. It contains the M^2 case calculated for dust collapse in [129]. For $n = 2$, this yields a lifetime scaling proportional to M^3 which is of the same order as the lifetime predicted by Hawking evaporation [130]. However, unlike Hawking evaporation, which results in complete evaporation without an outgoing density profile, this model describes a quantum bounce with an outgoing phase. Thus, the model achieves a comparable timescale but through a distinct physical mechanism.

4.3 Concluding remarks on model metrics for quantum black hole evolution

The metric (4.1.8) with mass function (4.1.5) is phenomenologically designed to model gravitational collapse while incorporating features that are expected to arise from a full theory of quantum gravity. The primary feature of the metric is a non-singular bounce, modeled by a smooth time-dependent mass function (4.1.5). While it remains an open question whether such a metric can be derived as an effective description from a candidate theory of quantum gravity, it serves as a valuable toy model for exploring the phenomenology of singularity resolution.

For early times before the bounce (in the PG coordinate time), the metric could be that of classically collapsing matter in GR, i.e., outside the matter region it is Schwarzschild spacetime, and in the matter region it is a metric that satisfies the dominant energy condition. However, during and just after the bounce phase, the metric would correspond to a GR solution with matter that violates the "effective" dominant and "effective" strong energy conditions, but where the energy density ρ in (4.1.6) remains positive and finite everywhere for all t.

It is important to note that horizon formation and evaporation as shown in Figures (16), (17), and (18) follow directly from the metric. There are other conjectured proposals for nonsingular black holes with corresponding conformal diagrams. These include [128, 131] which are similar in spirit to what is presented here, but without an explicit metric. Ref. [132] on the other hand describes a black hole to white hole transition, where the black hole event horizon connects directly to a white hole horizon, but again no explicit non-vacuum metric is presently available. The conformal diagram derived from quantum gravity corrected dust collapse in [129, 133] is similar to Fig. (18), but with a shock wave that arises in that calculation.

In the following chapter, this model is extended to describe a transition into a white hole geometry following the collapse, rather than the symmetric bounce considered here.

5 Black hole to white hole evolution

In the previous chapter, a class of spacetime metrics was engineered to model gravitational collapse, a quantum bounce, and the eventual dynamical disappearance of the black hole—capturing features anticipated in effective models of quantum gravity. The metric contains a transient trapped region without a spacetime singularity, but does not contain anti-trapped regions. As such, it may be viewed as a dynamical analog of proposed static regular black holes.

A particularly compelling scenario in quantum gravity is that of a black hole interior undergoing a quantum bounce re-emerging as a white hole—a time-reversed black hole which expels matter. Unlike the trapped regions characteristic of black holes, white holes possess anti-trapped regions where the expansion of both ingoing and outgoing null geodesics is positive. The boundary of such an anti-trapped region is known as the past apparent horizon. Although unstable in classical GR, white holes can arise naturally in quantum gravity contexts, replacing classical singularities with a quantum bounce [131]. A black-to-white hole transition has been the focus of many studies within quantum gravity as a way to explain the re-emergence after a bounce. Notably, the Planck star scenario proposed by Rovelli and Vidotto suggests a Planck star serves as a quantum bridge between black hole and white hole regions, effectively replacing the classical singularity with a non-singular transition surface [134]. Related studies [135–137] have explored effective spacetimes describing such transitions, often constructing phenomenological metrics by gluing together distinct black hole and white hole regions. However, these approaches often neglect matter dynamics and may involve matching causally disconnected or static regions. In contrast, the model presented here constructs a single, continuous geometry incorporating both matter flow and dynamical horizons, without resorting to gluing procedures. It extends the bouncing scenario from the previous chapter to describe a smooth black-to-white hole transition within a unified dynamical framework. The metric features trapped and anti-trapped regions of finite lifetime and may be interpreted as arising from an inhomogeneous and anisotropic fluid.

5.1 Towards a White Hole Transition

A white hole region is characterized by the presence of an anti-trapped region, where the expansions of both future-directed ingoing and outgoing null congruences are positive. In spherically symmetric spacetimes, the expansion scalars for radial null geodesics provide a diagnostic tool for identifying trapped or anti-trapped regions. Consider again the generic spherically symmetric metric in PG coordinates

$$ds^2 = -(1 - N^r(r,t)^2)dt^2 + N^r(r,t)dtdr + dr^2 + r^2 d\Omega^2, \tag{5.1.1}$$

with arbitrary shift function $N^r(r,t)$. For this metric, the expansions of outgoing and ingoing radial null geodesics are given by

$$\theta_\pm = \frac{2}{r}(-N^r \pm 1), \tag{5.1.2}$$

where the positive (negative) sign corresponds to the outgoing (ingoing) null radial geodesics. The expansion scalars characterize spacetime regions as:

$$\text{Outside a black hole: } \theta_+ > 0 \text{ and } \theta_- < 0 \tag{5.1.3}$$

$$\text{Inside a black hole: } \theta_+ < 0 \text{ and } \theta_- < 0 \tag{5.1.4}$$

$$\text{Inside a white hole: } \theta_+ > 0 \text{ and } \theta_- > 0 \tag{5.1.5}$$

$$\text{Outside a white hole: } \theta_+ > 0 \text{ and } \theta_- < 0. \tag{5.1.6}$$

The behaviour of the expansion scalars imposes a "constraint" on the shift function: if $N^r > 0$ for all r and t, then although the outgoing expansion θ_+ may be positive or negative, the ingoing expansion θ_- will always be negative. As a result, the presence of a white hole region would be hindered. This situation is realized in the previous bounce-based model where the shift was defined by (4.1.2).

To overcome this and to allow the metric to describe regions with $\theta_\pm > 0$ at the same time, the shift is modified to:

$$N^r(r,t) = -\tanh(\lambda(t - t_0))\sqrt{\frac{2Gm(r,t)}{r}}, \tag{5.1.7}$$

where λ is a free parameter controlling the sharpness of the transition, and t_0 marks the bounce time. Using the mass and velocity functions (4.1.5) and (4.1.7), the modified shift introduces a time-dependent sign flip in N^r, allowing θ_- to become positive for $t > t_0$. This facilitates the emergence of an anti-trapped region across $t = t_0$, resulting in a white hole transition.

Altogether, the metric (5.1.1), combined with the new shift function (5.1.7) and previously defined mass and velocity profiles, defines a new class of spacetimes. These preserve the singularity resolution and dynamical horizons of the prior model while admitting white hole interiors, providing smooth black hole to white hole transitions.

It should be noted however, this construction introduces a limitation: because the sign flip in the shift function (5.1.7) occurs simultaneously at all radii, it implies that the outward "repulsive" behavior extends even to regions far from the central core where quantum gravitational effects would normally be expected to be negligible. This lack of localization may reduce the physical plausibility of the model in asymptotic or weak-field regimes. More refined constructions could attempt to localize the transition to the deep interior (e.g., by making the sign flip in N^r both time- and radius-dependent), but such extensions are beyond the scope of the present work.

5.2 Properties of the new model

5.2.1 Expansion scalar, horizons, and black hole to white hole transition

The modified metric (5.1.1) resolves the classical singularity as in the original model (Section 4.1), via the mass function (4.1.5). Its causal structure, however, differs significantly, enabling a black-to-white hole transition. As discussed, the behaviour of the expansion scalars play a crucial role in identifying the black hole and white hole horizons as well as their trapped and anti-trapped regions. The black hole outer apparent horizon occurs where $\theta_+ = 0$, the transition from positive to negative, while $\theta_- < 0$ for both the exterior and interior of the black hole. Solving $\theta_+ = 0$ yields two roots, indicating inner and outer horizons, as shown in the last two time shots in the first row of Fig.(20). Conversely, the white hole region is characterized by anti-trapped surfaces, where both expansions are positive. The outer horizon corresponds to the surface where the ingoing expansion θ_- changes sign from negative to positive, i.e., where $\theta_- = 0$. Once again, there are two roots marking the inner and outer white hole horizons, as can be seen in the middle time shot of the second row in Fig.(20). An important feature in this time sequence is that the transition from a black to a white hole region must have θ_+ become positive for all r, and that θ_- turns from negative to positive to signal a white hole region. This requires a transition region where $\theta_- < 0$ and $\theta_+ > 0$ for a brief time interval, since the black hole and white hole regions cannot overlap. This occurs in the $t = 0$ frame.

The horizon trajectory, along with the matter density peak trajectory in the $r - t$ plane is seen in Fig.(21). Notice the similarities and differences between this and Fig.(16). In the current model, the black hole horizons form and begin diverging. As $t \to t_0$ the outer horizon shrinks while the inner horizon expands and the two annihilate just before the bounce at $t = t_0$, marking the end of the black hole. Shortly after $t = t_0$, white hole horizons form and begin to diverge for a given time before again converging, meeting and annihilating, marking the end of the white hole. Throughout the evolution, the peak of the matter density follows the black hole inner horizon, crosses into trapped region, and exits before annihilation. The

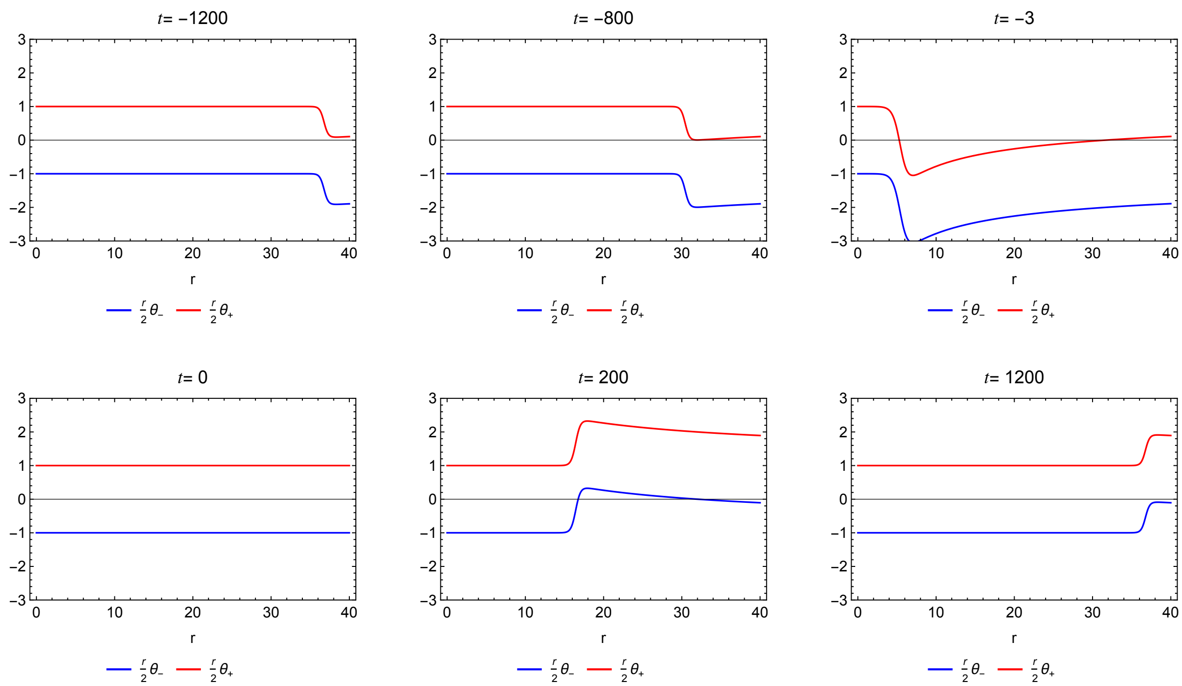

Figure 20: Behaviour of the expansion scalar θ_- for ingoing null radial geodesics and θ_+ for outgoing null radial geodesics for the improved shift function to exhibit a black to white hole transition. Here $M_0 = 4,\ l_0 = 1,\ n = 1,\ r_0 = 5, t_0 = 0,\ b = 3,\ A = 1,\ \lambda = 1,\ G = 1$

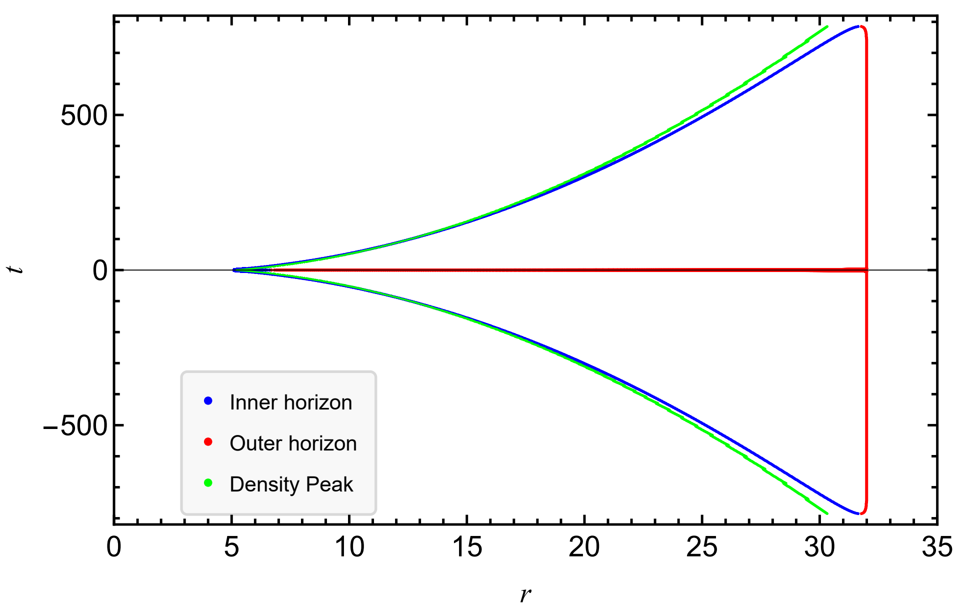

Figure 21: Horizon and density peak trajectories. Black hole horizons form and diverge before converging and annihilating before the bounce at $t = 0$, while white hole horizons form after the bounce and diverge before converging and annihilating. Note that the density is unchanged and as such exhibits the same behaviour as in Sec.4.

density peak hits the minimum radius at $t = t_0$ and expands, entering the white hole's anti-trapped region between its horizons and exiting before the white hole vanishes, as depicted in Fig.(21). The causal structure, illustrated in Fig.(22), reveals distinct dynamics and features

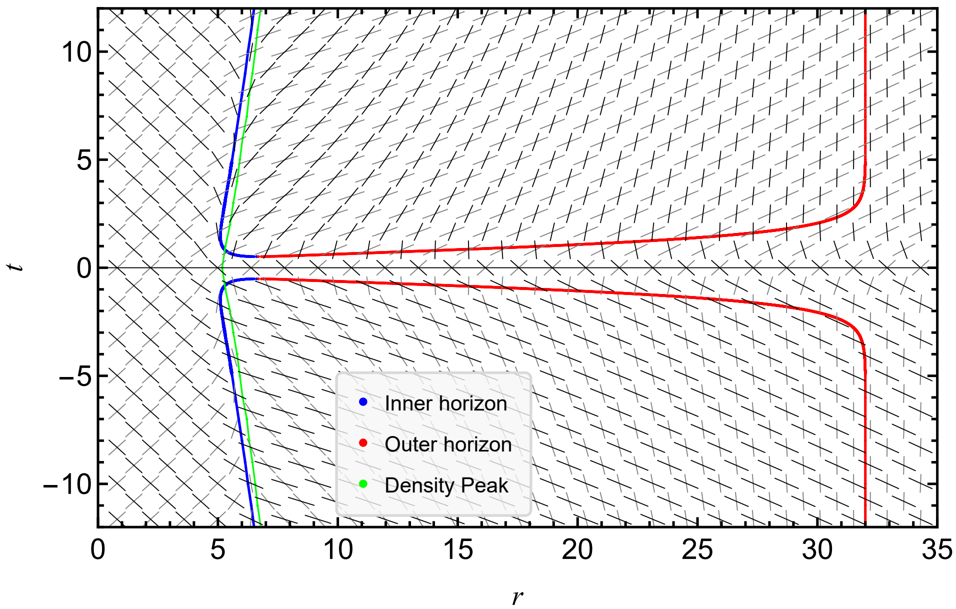

Figure 22: Close up view of the horizon evolution of the black and white hole, as well as the causal structure for the different regions.

of the spacetime. As in the previous model, the black hole's outer horizon starts spacelike, shifts to null for most of its lifetime, then becomes spacelike as it shrinks near $t = t_0$. The inner horizon remains timelike until just before the bounce, when it expands. Between the black hole's annihilation and the white hole's formation, spacetime is briefly flat, as θ_- cannot be simultaneously positive and negative to describe both interiors. The inner horizon of the white hole starts spacelike, briefly contracts, then begins to expand while becoming timelike. Its outer horizon starts spacelike, moves to larger r where it remains and becomes null for the most of the life time of the white hole.

Notably, the black hole and white hole cannot coexist; there appears to be a brief coordinate time interval separating their disappearance and appearance. This coordinate time between the transition will likely be dependent on various parameters of the model, making simultaneous formation likely require extreme fine-tuning of parameters rendering it physically unlikely. The schematic conformal diagram (Fig.(23)) depicts a Minkowski asymptotic structure, with trapped (black hole) and anti-trapped (white hole) regions as distinct bubbles.

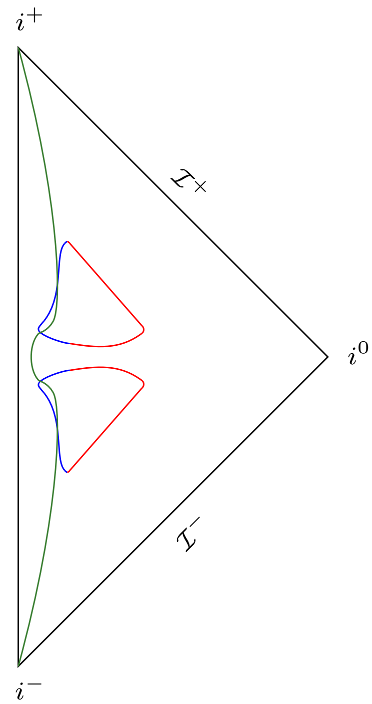

Figure 23: Schematic conformal diagram of the black hole (lower region) to white hole (upper region) transition.

5.2.2 Energy Conditions

As previously noted, but reiterated here for emphasis, it is generally expected that the Einstein's equations will no longer be the fundamental equations in a full theory of quantum gravity or even in effective, or modified gravity theories. As discussed in chapter 3, analyzing the effective stress-energy tensor and assessing the corresponding energy conditions may offer insights into the physical viability of the spacetime. In the present model, the spacetime is not vacuum and possesses its own effective SET, owing to the fact that the metric is non-stationary. However, due to the absence of access to the actual equations of motion, the effective stress-energy tensor is computed by treating the metric as a solution to Einstein's equations. With the spacetime metric (5.1.1) of the current model, the Einstein equations $T_{\mu\nu} = \frac{1}{8\pi G} G_{\mu\nu}$ can be diagonalized and the stress-energy tensor components can be identified as $T^0{}_0 = -\rho$, the energy density, and $T^i{}_i = p_i$ the radial and tangential pressures [8]. These are given by

$$
\begin{aligned}
T^0_0 = -\rho &= -\frac{1}{8\pi G r^2} N^r \left[2r\left(\partial_r N^r\right) + N^r\right], \\
T^1_1 = p_r &= -\frac{1}{8\pi G r^2} \left[2rN^r\partial_r N^r - 2r\partial_t N^r + \left(N^r\right)^2\right], \\
T^2_2 = T^3_3 = p_\theta = p_\phi &= \frac{1}{8\pi G r} \left[-r\left(\partial_r N^r\right)^2 - N^r\left(2\partial_r N^r + r\partial_r^2 N^r\right) + \partial_t N^r + r\partial_t\partial_r N^r\right]
\end{aligned}
\tag{5.2.1}
$$

The dominant energy condition (DEC), $\rho \geq |p_r|$ and $\rho \geq |p_\theta|$, reflects the idea that the energy density measured by any observer should be non-negative and that matter should propagate along timelike or null world lines. Violations of the DEC are anticipated in quantum gravity due to exotic effects, such as negative energy densities, near the bounce region [29]. Figure (24) shows both components of the DEC, $\rho - |p_r|$ and $\rho - |p_\theta|$ as well as the density and radial pressure. For the most part $\rho - |p_r|$ remains near zero across most of the spacetime, except near horizons and the bounce where it becomes significantly negative indicating a strong violation of the DEC as would be expected. An additional violation occurs at $t = t_0$ for large r, possibly due to the outer horizon's inward motion as it annihilates with the inner horizon (and its time-reversed counterpart for the white hole).

Similarly, $\rho - |p_\theta|$ is very close to zero except near horizons and the bounce, where it reaches its most negative value. Inside the black and white holes (to the right of horizons), $\rho - |p_\theta|$ is negative; outside (closer to $r = 0$ than the inner horizons), it is positive. Unlike $\rho - |p_r|$ no significant DEC violation occurs along the $t = 0$ hypersurface for large r. From Fig.(24), similar to the DEC, the effective density is positive everywhere except along the horizons and significantly negative near the bounce, reflecting the quantum effects becoming dominant near the classical singularity.

5.3 Conclusion

This work presents a novel, phenomenological, model-independent, non-stationary, spherically symmetric, singularity-free, and asymptotically flat metric that describes the formation and annihilation of a black hole, followed by a bounce and a subsequent transition to a white hole.

The metric is constructed by "following the matter" using a "designer" mass function in PG coordinates, rather than by gluing together several metrics to achieve the desired outcome. Although the metric captures several desirable features that might emerge from a theory of quantum gravity, it remains to be seen whether it can arise as a solution in an effective theory with quantum gravity corrections. There are a few specific features of the

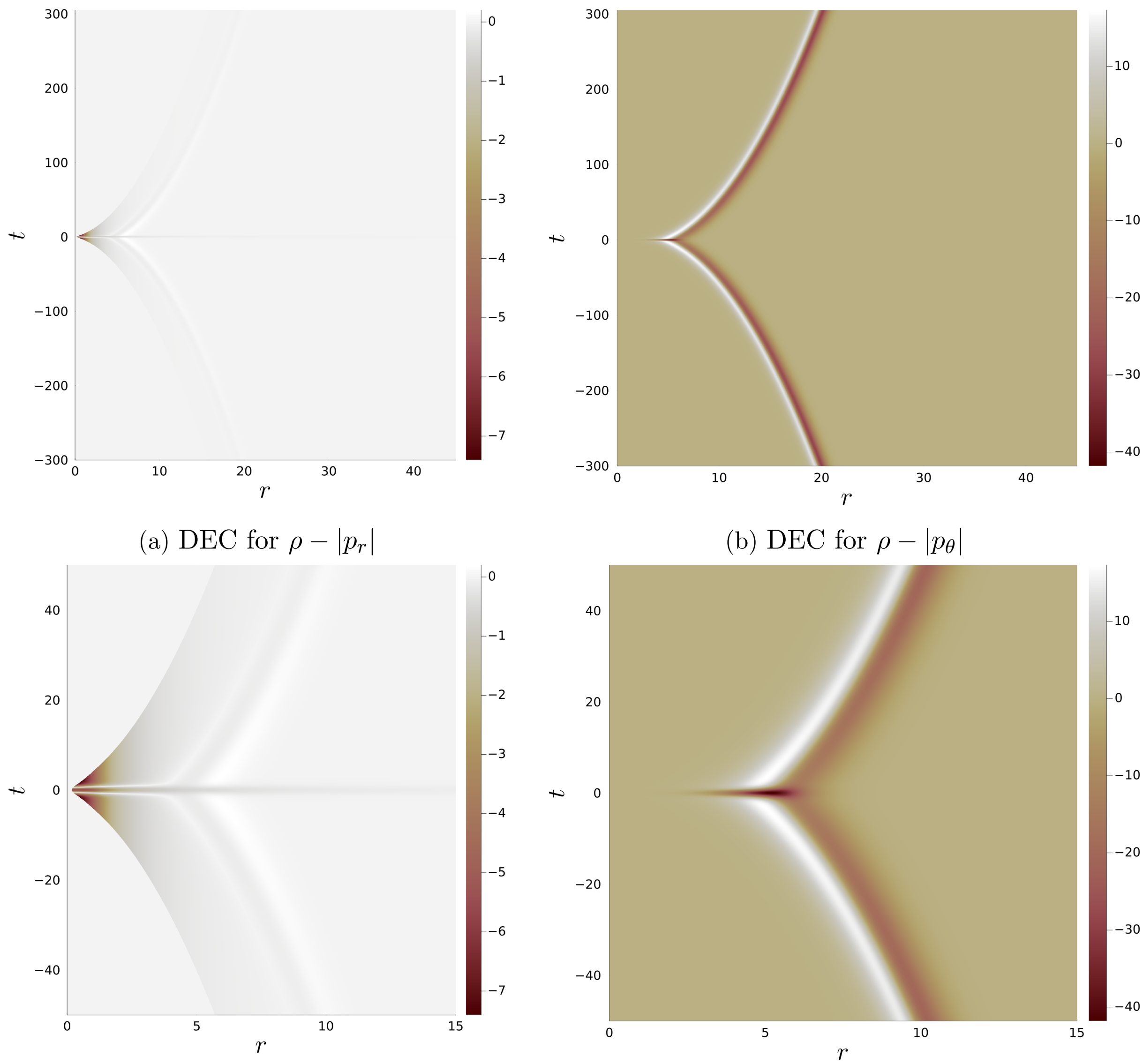

(a) DEC for $\rho - |p_r|$

(b) DEC for $\rho - |p_\theta|$

(c) Zoomed in DEC for $\rho - |p_r|$

(d) Zoomed in DEC for $\rho - |p_\theta|$

Figure 24: Different components of DEC.

geometry that are noteworthy: (i) the BH and WH horizons do not intersect at a point, unlike what is proposed in models that use junctions conditions; (ii) the matter and inner horizons move together and are timelike in some regions and spacelike in others; (iii) matter is superluminal where the BH region ends and the WH region begins (Fig. 22); (iv) the DEC is violated in these regions.

Unlike previous models that glue black and white hole regions across a transition surface [134, 135], this model employs a smooth, time-dependent shift function (5.1.7) to describe the entire evolution within a single metric. Incorporating dynamical matter flow and evolving horizons, this model avoids artificial matching conditions and fine tuning, providing a physically consistent description of quantum black hole evolution. Consistent with LQG's singularity resolution and broader quantum gravity paradigms, the model advances the bounce framework of [123].

6 Conclusion

This dissertation has examined various approaches to resolving black hole singularities within the context of quantum gravity. While each chapter employed different methods ranging from canonical loop quantum gravity and generalized uncertainty principles to phenomenological, model-independent constructions, a common objective underlies all: the construction of regular, geodesically complete black hole spacetimes incorporating key features expected from a quantum theory of gravity.

Chapter 2 presented loop quantum gravity (LQG) corrections to the Raychaudhuri equation in the Schwarzschild interior. Utilizing a Kantowski–Sachs symmetry reduction and effective polymer quantization, the analysis demonstrated that quantum geometric effects introduce repulsive terms into the modified Raychaudhuri equation. These terms defocus geodesics, prevent the formation of conjugate points, and ultimately invalidate the classical singularity theorems, thereby enabling singularity resolution at the effective level.

Chapter 3 applied similar reasoning within the framework of the generalized uncertainty principle (GUP). A momentum-dependent correction scheme, inspired by similar improvements made in LQC, was developed and used to extend an effective interior metric to the full spacetime. The resulting GUP-inspired spacetime was shown to be asymptotically flat and regular throughout. The associated Kretschmann scalar and expansion scalars remained finite everywhere, reinforcing the conclusion that the classical singularity is resolved in this model as well.

Chapters 4 and 5 shifted toward a more flexible and theory-agnostic framework. In Chapter 4, a class of time-dependent, spherically symmetric metrics was constructed to model the collapse and bounce of matter without invoking a specific quantum gravity theory. These metrics were engineered to avoid singularity formation and to dynamically describe horizon formation, evolution, and annihilation. Chapter 5 extended this framework to include a black hole to white hole transition by modifying the shift function in a way that enforces the expansion scalar to flip signs allowing for an anti-trapped region. These models serve as effective spacetime descriptions that mimic expected quantum gravitational behavior without relying on a particular quantization scheme or "cutting and gluing" metrics at a transition surface.

Despite their technical differences, the models offer complementary perspectives on quantum black hole dynamics and share several unifying principles:

1. Geodesic completeness as a diagnostic tool: The behavior of geodesic congruences—analyzed through the Raychaudhuri equation—served as a central criterion for identifying the presence or resolution of singularities in chapters 2 and 3.

2. Regularity and asymptotic flatness: Each model was confirmed or constructed to be free from curvature divergences while recovering standard general relativity in low-curvature regimes far from the classical singularity.

3. Effective, semiclassical treatment: Rather than relying on full quantization, the models adopted an effective approach, incorporating leading-order quantum corrections into classical variables and equations.

4. Progression from theory-specific to theory-independent methods: The dissertation transitioned from models grounded in specific quantum gravity theories (LQG and GUP) to more phenomenological constructions based on general physical expectations of quantum gravity.

The results contribute to the broader research effort aimed at understanding the fate of spacetime singularities in quantum gravity. Specifically, they demonstrate that:

- Singularities can be resolved within a variety of frameworks through effective modifications of classical gravitational dynamics.

- Techniques developed in distinct quantum gravity approaches can inform one another, leading to a convergence of effective features—such as bounded curvature, quantum bounces, and non-singular trapped regions.

- Phenomenological, model-independent metrics offer a practical means of testing quantum gravitational ideas, even in the absence of a complete theory.

These are not free from limitations. All models considered assume spherical symmetry, which simplifies the geometry and reduces the problem to a manageable number of degrees of freedom. However, realistic gravitational collapse scenarios may involve non-symmetric or rotating configurations, and it is unclear whether the methods employed here would extend naturally to those cases. It is also important to note that the spacetimes are effective constructions, not derived from a full quantum theory. While motivated by loop quantum gravity, the generalized uncertainty principle, or general expectations about quantum gravitational behavior, these models remain phenomenological. Their connection to a fundamental quantum theory remains indirect, and their consistency with the full dynamics of such a theory is not guaranteed.

In conclusion, this dissertation advances the understanding of quantum black holes by demonstrating that effective models, whether derived from LQG, GUP, or phenomenological constructions, can resolve singularities and provide insights into horizon dynamics and spacetime evolution. These models highlight the diverse approaches to quantum gravity and lay the groundwork for future investigations into the quantum nature of gravity and its astrophysical manifestations.

References

[1] A. Ashtekar, T. Pawlowski, and P. Singh, "Quantum Nature of the Big Bang: Improved dynamics," Phys. Rev., vol. D74, p. 084003, 2006.

[2] L. Modesto, I. Premont-Schwarz, and A. Randono, "Non-singular black holes in loop quantum gravity," Physical Review D, vol. 82, no. 10, p. 104027, 2010.

[3] R. Brandenberger, "String cosmology: A review," arXiv preprint arXiv:1206.4196, 2012.

[4] S. D. Mathur, "The fuzzball proposal for black holes: An elementary review," Fortschritte der Physik, vol. 57, no. 5-7, pp. 803–831, 2009.

[5] V. P. Frolov and A. Zelnikov, Introduction to black hole physics. Oxford: Oxford Univ. Press, 2011.

[6] S. M. Carroll, Spacetime And Geometry An Introduction To General Relativity. Addison Wesley, 2004.

[7] S. W. Hawking and G. F. R. Ellis, The Large Scale Structure of Space-Time. Cambridge Monographs on Mathematical Physics, Cambridge University Press, 2011.

[8] R. M. Wald, General Relativity. Chicago, USA: Chicago Univ. Pr., 1984.

[9] C. W. Misner, K. S. Thorne, and J. A. Wheeler, Gravitation. San Francisco: W. H. Freeman, 1973.

[10] E. Poisson, A Relativist's Toolkit: The Mathematics of Black-Hole Mechanics. Cambridge University Press, 12 2009.

[11] K. A. Bronnikov and S. G. Rubin, Black Holes, Cosmology and Extra Dimensions. WSP, 2012.

[12] A. Raychaudhuri, "Relativistic cosmology. 1.," Phys. Rev., vol. 98, pp. 1123–1126, 1955.

[13] S. Hawking and R. Penrose, "The Singularities of gravitational collapse and cosmology," Proc. Roy. Soc. Lond. A, vol. 314, pp. 529–548, 1970.

[14] B. e. a. L. S. C. Abbott and V. Collaboration), "Observation of gravitational waves from a binary black hole merger," Phys. Rev. Lett., vol. 116, p. 061102, 2016.

[15] B. e. a. L. S. C. Abbott and V. Collaboration), “Gwtc-1: A gravitational-wave transient catalog of compact binary mergers observed by ligo and virgo during the first and second observing runs,” Phys. Rev. X, vol. 9, no. 3, p. 031040, 2019.

[16] E. Berti, V. Cardoso, and A. O. Starinets, “Quasinormal modes of black holes and black branes,” Class. Quant. Grav., vol. 26, p. 163001, 2009.

[17] E. H. T. Collaboration, “First m87 event horizon telescope results. i. the shadow of the supermassive black hole,” Astrophys. J. Lett., vol. 875, no. 1, p. L1, 2019.

[18] E. H. T. Collaboration, “First sagittarius a* event horizon telescope results. i. the shadow of the supermassive black hole in the center of the milky way,” Astrophys. J. Lett., vol. 930, no. 2, p. L12, 2022.

[19] R. Narayan, “Black holes in astrophysics,” New J. Phys., vol. 7, p. 199, 2005.

[20] C. S. Reynolds, “Measuring black hole spin using x-ray reflection spectroscopy,” Space Sci. Rev., vol. 183, pp. 277–294, 2014.

[21] A. M. e. a. Ghez, “Measuring distance and properties of the milky way’s central supermassive black hole with stellar orbits,” Astrophys. J., vol. 689, pp. 1044–1062, 2008.

[22] J. A. Wheeler and K. Ford, Geons, black holes, and quantum foam: A life in physics. 1998.

[23] M. Bojowald, Canonical Gravity and Applications: Cosmology, Black Holes, and Quantum Gravity. Cambridge University Press, 2010.

[24] P. Dona and S. Speziale, “Introductory lectures to loop quantum gravity,” in Gravitation: Theory and Experiment, 3rd School on Theoretical Physics, pp. 89–140, 7 2010.

[25] A. Ashtekar, Lectures on nonperturbative canonical gravity, vol. 6. 1991.

[26] Y. Tavakoli, “Lecture iii: Ashtekar variables for general relativity.” https://www.cosmo-ufes.org/uploads/1/3/7/0/13701821/lect.notes-3.pdf, 2015. Courses in Canonical Gravity, Universidade Federal do Esp´irito Santo.

[27] T. Thiemann, “Modern canonical quantum general relativity,” 2001.

[28] M. Han, “Introductory lectures on loop quantum gravity.” https://hamsyn.github.io/LQG-group/lecture.html, 2020. Accessed: 2025-04-10.

[29] M. Bojowald, "Loop quantum cosmology," Living Rev. Rel., vol. 8, p. 11, 2005.

[30] A. Ashtekar and M. Bojowald, "Quantum geometry and the Schwarzschild singularity," Class. Quant. Grav., vol. 23, pp. 391–411, 2006.

[31] A. Ashtekar, S. Fairhurst, and J. L. Willis, "Quantum gravity, shadow states, and quantum mechanics," Class. Quant. Grav., vol. 20, pp. 1031–1062, 2003.

[32] A. Ashtekar, M. Bojowald, and J. Lewandowski, "Mathematical structure of loop quantum cosmology," Adv. Theor. Math. Phys., vol. 7, no. 2, pp. 233–268, 2003.

[33] A. Corichi, T. Vukasinac, and J. A. Zapata, "Polymer Quantum Mechanics and its Continuum Limit," Phys. Rev. D, vol. 76, p. 044016, 2007.

[34] A. Ashtekar, T. Pawlowski, and P. Singh, "Quantum nature of the big bang," Phys. Rev. Lett., vol. 96, p. 141301, 2006.

[35] A. Corichi and P. Singh, "Loop quantization of the Schwarzschild interior revisited," Class. Quant. Grav., vol. 33, no. 5, p. 055006, 2016.

[36] K. Blanchette, S. Das, S. Hergott, and S. Rastgoo, "Black hole singularity resolution via the modified Raychaudhuri equation in loop quantum gravity," Phys. Rev. D, vol. 103, no. 8, p. 084038, 2021.

[37] A. Ashtekar, "Loop Quantum Cosmology: An Overview," Gen. Rel. Grav., vol. 41, pp. 707–741, 2009.

[38] A. Ashtekar, J. Olmedo, and P. Singh, "Regular black holes from loop quantum gravity," 2023.

[39] M. Bojowald, "Spherically symmetric quantum geometry: States and basic operators," Class. Quant. Grav., vol. 21, pp. 3733–3753, 2004.

[40] M. Bojowald and R. Swiderski, "Spherically symmetric quantum geometry: Hamiltonian constraint," Class. Quant. Grav., vol. 23, pp. 2129–2154, 2006.

[41] Böhmer, Christian G. and Vandersloot, Kevin, "Loop Quantum Dynamics of the Schwarzschild Interior," Phys. Rev. D, vol. 76, p. 104030, 2007.

[42] Böhmer, Christian G. and Vandersloot, Kevin, "Stability of the Schwarzschild Interior in Loop Quantum Gravity," Phys. Rev. D, vol. 78, p. 067501, 2008.

[43] J. Ben Achour, F. Lamy, H. Liu, and K. Noui, "Non-singular black holes and the Limiting Curvature Mechanism: A Hamiltonian perspective," JCAP, vol. 05, p. 072, 2018.

[44] A. Ashtekar, J. Olmedo, and P. Singh, "Quantum extension of the Kruskal spacetime," Phys. Rev. D, vol. 98, no. 12, p. 126003, 2018.

[45] J. Ben Achour, F. Lamy, H. Liu, and K. Noui, "Polymer Schwarzschild black hole: An effective metric," EPL, vol. 123, no. 2, p. 20006, 2018.

[46] A. Barrau, K. Martineau, and F. Moulin, "A status report on the phenomenology of black holes in loop quantum gravity: Evaporation, tunneling to white holes, dark matter and gravitational waves," Universe, vol. 4, no. 10, p. 102, 2018.

[47] D. Arruga, J. Ben Achour, and K. Noui, "Deformed General Relativity and Quantum Black Holes Interior," Universe, vol. 6, no. 3, p. 39, 2020.

[48] J. Ben Achour, S. Brahma, S. Mukohyama, and J.-P. Uzan, "Towards consistent black-to-white hole bounces from matter collapse," JCAP, vol. 09, p. 020, 2020.

[49] N. Bodendorfer, F. M. Mele, and J. Münch, "Effective Quantum Extended Spacetime of Polymer Schwarzschild Black Hole," Class. Quant. Grav., vol. 36, no. 19, p. 195015, 2019.

[50] N. Bodendorfer, F. M. Mele, and J. Münch, "(b,v)-type variables for black to white hole transitions in effective loop quantum gravity," Physics Letters B, vol. 819, p. 136390, Aug. 2021.

[51] M. Bojowald and J. D. Reyes, "Dilaton Gravity, Poisson Sigma Models and Loop Quantum Gravity," Class. Quant. Grav., vol. 26, p. 035018, 2009.

[52] M. Bojowald, T. Harada, and R. Tibrewala, "Lemaitre-Tolman-Bondi collapse from the perspective of loop quantum gravity," Phys. Rev. D, vol. 78, p. 064057, 2008.

[53] M. Bojowald and S. Brahma, "Signature change in two-dimensional black-hole models of loop quantum gravity," Phys. Rev. D, vol. 98, no. 2, p. 026012, 2018.

[54] M. Bojowald and S. Brahma, "Signature change in loop quantum gravity: Two-dimensional midisuperspace models and dilaton gravity," Phys. Rev. D, vol. 95, no. 12, p. 124014, 2017.

[55] M. Bojowald, S. Brahma, and D.-h. Yeom, "Effective line elements and black-hole models in canonical loop quantum gravity," Phys. Rev. D, vol. 98, no. 4, p. 046015, 2018.

[56] S. Brahma, "Spherically symmetric canonical quantum gravity," Phys. Rev. D, vol. 91, no. 12, p. 124003, 2015.

[57] M. Campiglia, R. Gambini, and J. Pullin, "Loop quantization of spherically symmetric midi-superspaces : The Interior problem," AIP Conf. Proc., vol. 977, no. 1, pp. 52–63, 2008.

[58] D.-W. Chiou, "Phenomenological loop quantum geometry of the Schwarzschild black hole," Phys. Rev. D, vol. 78, p. 064040, 2008.

[59] A. Corichi, A. Karami, S. Rastgoo, and T. Vukavsinac, "Constraint Lie algebra and local physical Hamiltonian for a generic 2D dilatonic model," Class. Quant. Grav., vol. 33, no. 3, p. 035011, 2016.

[60] J. Cortez, W. Cuervo, H. A. Morales-Técotl, and J. C. Ruelas, "Effective loop quantum geometry of Schwarzschild interior," Phys. Rev. D, vol. 95, no. 6, p. 064041, 2017.

[61] R. Gambini and J. Pullin, "Black holes in loop quantum gravity: The Complete space-time," Phys. Rev. Lett., vol. 101, p. 161301, 2008.

[62] R. Gambini, J. Pullin, and S. Rastgoo, "Quantum scalar field in quantum gravity: The vacuum in the spherically symmetric case," Class.Quant.Grav., vol. 26, p. 215011, 2009.

[63] R. Gambini, J. Pullin, and S. Rastgoo, "Quantum scalar field in quantum gravity: the propagator and Lorentz invariance in the spherically symmetric case," Gen. Rel. Grav., vol. 43, pp. 3569–3592, 2011.

[64] R. Gambini and J. Pullin, "Loop quantization of the Schwarzschild black hole," Phys. Rev. Lett., vol. 110, no. 21, p. 211301, 2013.

[65] R. Gambini, J. Olmedo, and J. Pullin, "Spherically symmetric loop quantum gravity: analysis of improved dynamics," Class. Quant. Grav., vol. 37, no. 20, p. 205012, 2020.

[66] V. Husain and O. Winkler, "Quantum resolution of black hole singularities," Class. Quant. Grav., vol. 22, pp. L127–L134, 2005.

[67] V. Husain and O. Winkler, "Quantum Hamiltonian for gravitational collapse," Phys. Rev. D, vol. 73, p. 124007, 2006.

[68] J. G. Kelly, R. Santacruz, and E. Wilson-Ewing, "Black hole collapse and bounce in effective loop quantum gravity," Classical and Quantum Gravity, vol. 38, no. 4, 2020.

[69] J. G. Kelly, R. Santacruz, and E. Wilson-Ewing, "Effective loop quantum gravity framework for vacuum spherically symmetric spacetimes," Physical Review D, vol. 102, Nov. 2020.

[70] A. Kreienbuehl, V. Husain, and S. S. Seahra, "Modified general relativity as a model for quantum gravitational collapse," Class. Quant. Grav., vol. 29, p. 095008, 2012.

[71] L. Modesto, "Loop quantum black hole," Class. Quant. Grav., vol. 23, pp. 5587–5602, 2006.

[72] L. Modesto and I. Premont-Schwarz, "Self-dual Black Holes in LQG: Theory and Phenomenology," Phys. Rev. D, vol. 80, p. 064041, 2009.

[73] J. Olmedo, S. Saini, and P. Singh, "From black holes to white holes: a quantum gravitational, symmetric bounce," Class. Quant. Grav., vol. 34, no. 22, p. 225011, 2017.

[74] T. Thiemann and H. Kastrup, "Canonical quantization of spherically symmetric gravity in Ashtekar's selfdual representation," Nucl. Phys. B, vol. 399, pp. 211–258, 1993.

[75] C. Zhang, Y. Ma, S. Song, and X. Zhang, "Loop quantum Schwarzschild interior and black hole remnant," Phys. Rev. D, vol. 102, no. 4, p. 041502, 2020.

[76] J. Ziprick, J. Gegenberg, and G. Kunstatter, "Polymer Quantization of a Self-Gravitating Thin Shell," Phys. Rev. D, vol. 94, no. 10, p. 104076, 2016.

[77] M. Campiglia, R. Gambini, and J. Pullin, "Loop quantization of spherically symmetric midi-superspaces," Class. Quant. Grav., vol. 24, pp. 3649–3672, 2007.

[78] R. Gambini, J. Pullin, and S. Rastgoo, "New variables for 1+1 dimensional gravity," Class.Quant.Grav., vol. 27, p. 025002, 2010.

[79] S. Rastgoo, "A local true hamiltonian for the cghs model in new variables," 2013.

[80] A. Corichi, J. Olmedo, and S. Rastgoo, "Callan-Giddings-Harvey-Strominger vacuum in loop quantum gravity and singularity resolution," Phys.Rev.D, vol. 94, no. 8, p. 084050, 2016.

[81] H. A. Morales-Técotl, S. Rastgoo, and J. C. Ruelas, "Effective dynamics of the Schwarzschild black hole interior with inverse triad corrections," Annals Phys., vol. 426, p. 168401, 2021.

[82] J. Ben Achour, S. Brahma, and J.-P. Uzan, "Bouncing compact objects. Part I. Quantum extension of the Oppenheimer-Snyder collapse," JCAP, vol. 03, p. 041, 2020.

[83] J. Ben Achour and J.-P. Uzan, "Bouncing compact objects. ii. effective theory of a pulsating planck star," Phys. Rev. D, vol. 102, p. 124041, Dec 2020.

[84] D.-W. Chiou, "Phenomenological dynamics of loop quantum cosmology in Kantowski-Sachs spacetime," Phys. Rev. D, vol. 78, p. 044019, 2008.

[85] C. Collins, "Global structure of the Kantowski-Sachs cosmological models," J. Math. Phys., vol. 18, p. 2116, 1977.

[86] A. Ashtekar, T. Pawlowski, and P. Singh, "Quantum Nature of the Big Bang: An Analytical and Numerical Investigation. I.," Phys. Rev., vol. D73, p. 124038, 2006.

[87] T. Thiemann, Modern Canonical Quantum General Relativity. Cambridge Monographs on Mathematical Physics, Cambridge University Press, 2007.

[88] S. Rastgoo and S. Das, "Probing the interior of the schwarzschild black hole using congruences: Lqg vs. gup," Universe, vol. 8, p. 349, June 2022.

[89] F. Fragomeno, D. M. Gingrich, S. Hergott, S. Rastgoo, and E. Vienneau, "A generalized uncertainty-inspired quantum black hole," Physical Review D, vol. 111, Jan. 2025.

[90] P. Bosso, O. Obregón, S. Rastgoo, and W. Yupanqui, "Black hole interior quantization: a minimal uncertainty approach," Classical and Quantum Gravity, vol. 41, p. 135011, June 2024.

[91] H. A. Morales-Técotl, S. Rastgoo, and J. C. Ruelas, "Path integral polymer propagator of relativistic and nonrelativistic particles," Phys.Rev.D, vol. 95, no. 6, p. 065026, 2017.

[92] H. A. Morales-Técotl, D. H. Orozco-Borunda, and S. Rastgoo, "Polymer quantization and the saddle point approximation of partition functions," Phys.Rev.D, vol. 92, no. 10, p. 104029, 2015.

[93] E. Flores-González, H. A. Morales-Técotl, and J. D. Reyes, "Propagators in Polymer Quantum Mechanics," Annals Phys., vol. 336, pp. 394–412, 2013.

[94] H. A. Morales-Técotl, D. H. Orozco-Borunda, and S. Rastgoo, "Polymerization, the Problem of Access to the Saddle Point Approximation, and Thermodynamics," in 14th Marcel Grossmann Meeting on Recent Developments in Theoretical and Experimental General vol. 4, pp. 4054–4059, 2017.

[95] C. G. Boehmer and K. Vandersloot, "Loop Quantum Dynamics of the Schwarzschild Interior," Phys. Rev. D, vol. 76, p. 104030, 2007.

[96] A. Kempf, G. Mangano, and R. B. Mann, "Hilbert space representation of the minimal length uncertainty relation," Phys. Rev. D, vol. 52, pp. 1108–1118, 1995.

[97] P. Bosso, G. G. Luciano, L. Petruzziello, and F. Wagner, "30 years in: Quo vadis generalized uncertainty principle?," Class. Quant. Grav., vol. 40, no. 19, p. 195014, 2023.

[98] A. F. Ali, S. Das, and E. C. Vagenas, "Discreteness of Space from the Generalized Uncertainty Principle," Phys. Lett. B, vol. 678, pp. 497–499, 2009.

[99] S. Das and E. C. Vagenas, "Universality of Quantum Gravity Corrections," Phys. Rev. Lett., vol. 101, p. 221301, 2008.

[100] P. Bosso, S. Das, and R. B. Mann, "Planck scale corrections to the harmonic oscillator, coherent, and squeezed states," Phys. Rev. D, vol. 96, p. 066008, Sep 2017.

[101] P. Bosso, O. Obregón, S. Rastgoo, and W. Yupanqui, "Deformed algebra and the effective dynamics of the interior of black holes," Class. Quant. Grav., vol. 38, no. 14, p. 145006, 2021.

[102] K. Blanchette, S. Das, and S. Rastgoo, "Effective GUP-modified Raychaudhuri equation and black hole singularity: four models," JHEP, vol. 09, p. 062, 2021.

[103] S. Rastgoo and S. Das, "Probing the Interior of the Schwarzschild Black Hole Using Congruences: LQG vs. GUP," Universe, vol. 8, no. 7, p. 349, 2022.

[104] A. Ashtekar, J. Olmedo, and P. Singh, "Quantum Transfiguration of Kruskal Black Holes," Phys. Rev. Lett., vol. 121, no. 24, p. 241301, 2018.

[105] P. Jizba, H. Kleinert, and F. Scardigli, "Uncertainty Relation on World Crystal and its Applications to Micro Black Holes," Phys. Rev. D, vol. 81, p. 084030, 2010.

[106] A. Ashtekar and J. Olmedo, "Properties of a recent quantum extension of the Kruskal geometry," Int. J. Mod. Phys. D, vol. 29, no. 10, p. 2050076, 2020.

[107] A. Simpson and M. Visser, "Black-bounce to traversable wormhole," JCAP, vol. 02, p. 042, 2019.

[108] A. Komar, "Positive-definite energy density and global consequences for general relativity," Phys. Rev., vol. 129, pp. 1873–1876, Feb 1963.

[109] R. Arnowitt, S. Deser, and C. W. Misner, "Dynamical structure and definition of energy in general relativity," Phys. Rev., vol. 116, pp. 1322–1330, Dec 1959.

[110] E. Gourgoulhon, "3+1 formalism and bases of numerical relativity," 3 2007.

[111] C. W. Misner and D. H. Sharp, "Relativistic equations for adiabatic, spherically symmetric gravitational collapse," Phys. Rev., vol. 136, pp. B571–B576, Oct 1964.

[112] V. Faraoni, A. Giusti, and T. F. Bean, "Asymptotic flatness and Hawking quasilocal mass," Phys. Rev. D, vol. 103, no. 4, p. 044026, 2021.

[113] S. Hossenfelder, "Minimal length scale scenarios for quantum gravity," Living Rev. Rel., vol. 16, p. 2, 2013.

[114] A. N. Tawfik and A. M. Diab, "Review on generalized uncertainty principle," Rept. Prog. Phys., vol. 78, p. 126001, 2015.

[115] S. Mathur, "The fuzzball proposal for black holes: an elementary review," Fortschritte der Physik, vol. 53, p. 793–827, June 2005.

[116] S. D. Mathur and M. Mehta, "The fuzzball paradigm," 2025.

[117] D. Oriti, L. Sindoni, and E. Wilson-Ewing, "Bouncing cosmologies from quantum gravity condensates," Class. Quant. Grav., vol. 34, no. 4, p. 04LT01, 2017.

[118] E. Bianchi, C. Rovelli, and F. Vidotto, "Towards spinfoam cosmology," Physical Review D, vol. 82, Oct. 2010.

[119] M. Han, H. Liu, D. Qu, F. Vidotto, and C. Zhang, "Cosmological dynamics from covariant loop quantum gravity with scalar matter," 2024.

[120] E. Alesci, G. Botta, F. Cianfrani, and S. Liberati, "Cosmological singularity resolution from quantum gravity: The emergent-bouncing universe," Physical Review D, vol. 96, Aug. 2017.

[121] B. Melchor, R. Perca, and W. Yupanqui, "Semiclassical resolution of the black hole singularity inspired in the minimal uncertainty approach," Nuclear Physics B, vol. 1004, p. 116584, July 2024.

[122] S. Gielen and L. Menéndez-Pidal, "Black hole singularity resolution in unimodular gravity from unitarity," Physical Review Letters, vol. 134, Mar. 2025.

[123] S. Hergott, V. Husain, and S. Rastgoo, "Model metrics for quantum black hole evolution: Gravitational collapse, singularity resolution, and transient horizons," Physical Review D, vol. 106, Aug. 2022.

[124] M. S. Morris, K. S. Thorne, and U. Yurtsever, "Wormholes, Time Machines, and the Weak Energy Condition," Phys. Rev. Lett., vol. 61, pp. 1446–1449, 1988.

[125] M. Alcubierre, Wormholes, Warp Drives and Energy Conditions, vol. 189. Springer, 2017.

[126] J. Guven and N. Ó Murchadha, "Flat foliations of spherically symmetric geometries," Phys. Rev. D, vol. 60, p. 104015, Oct 1999.

[127] J. Guven and N. Ó Murchadha, "Flat foliations of spherically symmetric geometries," Physical Review D, vol. 60, Oct. 1999.

[128] S. A. Hayward, "Formation and evaporation of regular black holes," Phys. Rev. Lett., vol. 96, p. 031103, 2006.

[129] V. Husain, J. G. Kelly, R. Santacruz, and E. Wilson-Ewing, "Quantum gravity of dust collapse: Shock waves from black holes," Phys. Rev. Lett., vol. 128, p. 121301, Mar 2022.

[130] S. W. Hawking, "Particle Creation by Black Holes," Commun. Math. Phys., vol. 43, pp. 199–220, 1975. [,167(1975)].

[131] A. Ashtekar and M. Bojowald, "Black hole evaporation: A Paradigm," Class. Quant. Grav., vol. 22, pp. 3349–3362, 2005.

[132] P. Martin-Dussaud and C. Rovelli, "Evaporating black-to-white hole," Class. Quant. Grav., vol. 36, no. 24, p. 245002, 2019.

[133] V. Husain, J. G. Kelly, R. Santacruz, and E. Wilson-Ewing, "Fate of quantum black holes," Physical Review D, vol. 106, July 2022.

[134] C. Rovelli and F. Vidotto, “Planck stars,” Int. J. Mod. Phys. D, vol. 23, no. 12, p. 1442026, 2014.

[135] H. M. Haggard and C. Rovelli, “Quantum-gravity effects outside the horizon spark black to white hole tunneling,” Phys. Rev. D, vol. 92, no. 10, p. 104020, 2015.

[136] M. Han, C. Rovelli, and F. Soltani, “Geometry of the black-to-white hole transition within a single asymptotic region,” Physical Review D, vol. 107, Mar. 2023.

[137] J. M. Bardeen, “Models for the nonsingular transition of an evaporating black hole into a white hole,” 2019.